Broadband Solar Energy Harvesting Enabled by Micro and Nanostructured Materials

Dissertation

zur Erlangung des akademischen Grades

Doktoringenieur (Dr.-Ing.)

der

Fakultät für Elektrotechnik und Informationstechnik der

Technischen Universität Ilmenau

vorgelegt von

M. Eng. Pengfei Cheng

geb. am 07.09.1992 in Hubei, V.R. China

2022

1. Gutachter: Univ. -Prof. Dr. rer. nat. habil. Dr. h. c. Peter Schaaf

   (Technische Universität Ilmenau)

2. Gutachter: Univ.-Prof. Dr.-Ing. habil. Edda Rädlein

   (Technische Universität Ilmenau)

3. Gutachter: Prof. Dr. Zhang Zhang

   (South China Normal University)

Tag der Einreichung: 01.11.2022

Tag der wissenschaftlichen Aussprache: 31.05.2023

DOI: 10.22032/dbt.57584

URN: urn:nbn:de:gbv:ilm1-2023000134

Abstract

In the current era of "Carbon Peak and Carbon Neutrality", it is particularly important to develop low-cost, environmentally-friendly, and industrial-scale energy technologies to replace the traditional fossil fuels, which are widely considered to cause the greenhouse effect and frequent extreme weathers. Solar energy is a kind of energy that lasts forever and is freely available for all countries all over the world. Therefore, it is the most promising alternative to fossil energy compared to nuclear energy, wind energy, and blue energy (Energy that comes from ocean, such as tidal energy, salinity gradient energy). In this work, broadband solar energy harvesting materials are produced and demonstrated to serve as light absorbers for solar energy conversion applications, such as electric power generation, water steam generation and hydrogen generation. Firstly, black silicon (b-Si) with micro-nanostructures is fabricated by reactive ion etching (RIE). The as-prepared b-Si samples with ultra-broadband light absorption can be used for photo-thermoelectric (P-TE) power generation, photothermal (PT) water evaporation and photoelectrochemical (PEC) water reduction, which enhances solar energy conversion performance due to their excellent broadband light absorption. In addition, a metastable atomic layer deposition (MS-ALD) self-assembly strategy for fabricating large area 3D Ag@SiO_2 hybrid plasmonic nanostructures was developed. They also demonstrate an ultra-broadband super-high absorption over the whole solar spectrum. When they are further used for P-TE and PT water evaporation, the solar energy conversion performances are improved compared with b-Si samples.

Zusammenfassung

In der kommenden Ära des "Carbon Peak und der Kohlenstoffneutralität" ist es besonders wichtig, neue Energietechnologien zu entwickeln, die kostengünstig, umweltfreundlich und im industriellem Maßstab herstellbar sind, um die herkömmlichen fossilen Brennstoffe zu ersetzen, die weithin als Verursacher des Treibhauseffekts und häufiger extremer Wetterlagen gelten. Solarenergie ist sozusagen eine unerschöpfliche Energieform, die jedem Land der Erde kostenlos zur Verfügung steht. Daher ist sie im Vergleich zu Kernenergie, Windenergie und blauer Energie die vielversprechendste Alternative zu fossiler Energie. In dieser Arbeit werden breitbandige Materialien zur Gewinnung von Solarenergie als Lichtabsorber für Anwendungen zur Umwandlung von Solarenergie, wie Stromerzeugung, Wasserdampferzeugung und Wasserstofferzeugung, vorgestellt. Zunächst wird schwarzes Silizium (b-Si) mit einer Vielzahl von Mikro-Nanostrukturen durch reaktives Ionenätzen (RIE) hergestellt. Die so hergestellten b-Si-Proben mit ultra-breitbandiger Lichtabsorption können für die photo-thermoelektrische (P-TE) Stromerzeugung, die photothermische (PT) Wasserverdampfung und die photoelektrochemische (PEC) Wasserreduktion verwendet werden, was die Leistung der Solarenergieumwandlung aufgrund ihrer hervorragenden Lichtabsorption im gesamten Sonnenspektrum verbessert. Darüber hinaus wurde eine metastabile Atomlagenabscheidung (MS-ALD) mit Selbstorganisation zur Herstellung großflächiger plasmonischer 3D-Ag@SiO_2 Hybrid-Nanostrukturen entwickelt. Diese zeigen auch eine ultrabreitbandige sehr hohe Absorption im gesamten Sonnenspektrum. Wenn sie für die P-TE- und PT-Wasserverdampfung verwendet werden, verbessert sich die Leistung der Solarenergieumwandlung im Vergleich zu b-Si-Proben.

Acknowledgements

Time flies like an arrow, and the more than three-year PhD life is coming to an end. In the past three years, I have spent more than 1,000 days and nights under the supervisions of my dearest Prof. Peter Schaaf and PD Dr. Dong Wang, and with the warm accompany of our department members. Three years ago, I joined our WET group with hope. Three years later, I will leave with knowledge and skills, but I lost the initial confusion and gained more confidence in life. Here, I would like to express my deep gratitude to our colleagues, my friends and my family who have accompanied and helped me in work and life.

First and foremost, I would like to express my deeply gratitude to my supervisor Prof. Peter Schaaf who offered me a chance to join his group. His direct guidance, continuous encouragement and meaningful suggestions make me to be an excellent PhD student. He also devoted his full mind to modifying my manuscripts and contributed many useful comments on them. Then, I want to thank Dr. Dong Wang for his direct help on the experiments, data analysis and manuscripts. His high-efficiency modifications on the manuscript made them publish in time without too much delay. He also taught me how to be a patient, careful and serious scientist. Besides, I would also like to thank my master supervisor Prof. Zhang Zhang from South China Normal University for his contribution in this dissertation.

I want to thank China Scholarship Council (CSC) for offering enough scholarship to cover my life expense and insurance so that I can concentrate on the research work.

I also would like to deliver my sincere gratitude to my dear colleagues Prof. Lothar Spieß, Dr. Thomas Kups, Dr. Dimtry Zyabkin, Ms. Antje Schencke, Mr. Honglei Wang, Mr. Feitao Li, Ms. Emina Vardo, Ms. Michaela Blum, Mr. Sebastian Matthes, Ms. Yesenia Haydee Sauni Camposano Ms. Theresa Scheler, Mr. Hauke-Lars Honig, Dr. Marcus Hopfeld, Mr. Jens Schawol, Mr. Dominik Flock, Dr. Andreas Diemar, Dr. Gerd

Teicherd, Dr. Arne Albrecht, Ms. Manuela Breiter, Mr. Joachim Döll, Dr. Andrea Knauer, Mr. Christian Koppka, Dr. Herry Romanus, Dr. Mario Ziegler, Mr. Valentin Ripka, Mr. David Venier, Mr. Björn Müller, Prof. Dr. Jens Müller and Mr. Jonas Schneegaß for their contribution on this dissertation and their involvement in my PhD study.

Moreover, I want to thank Dr. Supreeti Shraddha, Dr. Yuhan Wu, Ms. Yulian Dong, Mr. Zhiqiang Zeng, Mr. Yuanwu Liu, Ms. Congcong Chen, Ms. Caiyi Jiang, Mr. Xuyan Zhang, Mr. Yuanwu Liu, Dr. Zhiyong Zhang and Ms. Shiya Rong for their assistance and encouragement on life and work.

Last but not the least, my deep gratitude is delivered to my family. They gave me encouragement, support and patience to me when I came across difficulties in both life and work. With the assistance of them, I gradually be a more independent man in Germany. I will always appreciate their love, care and support.

Table of Content

Contents

List of Figures

List of tables

1. Introduction

Developing new low cost, environmental friendliness, and industrial scale energy technologies to replace the traditional fossil fuels are widely considered to efficiently cope with energy crisis, greenhouse effect and frequent extreme weather issues.[1–5] Solar energy is a kind of energy that lasts forever and is freely available for all countries all over the world.[6,7] Therefore, solar energy is the most promising substitute to fossil energy compared to nuclear energy,[8] wind energy[9], and blue energy.[10] Among the solar energy conversion technologies,[11] silicon-based photovoltaic (PV) solar cell has been commercialized and the efficiency of monolithic silicon/perovskite solar cell has achieved over 29%.[12,13] Alternatively, photothermal conversion is another way to utilize solar energy and has drawn dramatically increasing attention due to the easily achievable large conversion efficiency (usually larger than 50%) for the applications in thermal catalysis,[14–17] water evaporation and desalination,[18–26] bacterial killing,[27] as well as thermal-responsive sensors.[28–30] Photothermal conversion of solar energy refers that solar energy is firstly converted into heat and then heat energy is utilized to achieve the desired destinations,[14,15,27,30–33] such as water purification, desalination, electric power generation, catalysis conversion, bacterial killing, and actuators. Thus, photothermal conversions of solar energy can be supplementary to PV-based technology in solar energy conversion and are deemed to be extremely important to clean energy production.[34–36] In addition, photoelectrochemical (PEC) water reduction that utilizes solar energy and additional bias for H_2 production is also an promising technology for solar energy conversion into chemical energy due to its environmental friendliness, sustainability, as well as no pollutant gas after use.

Generally, light absorbers with high-absorption in a broad spectrum are highly desired for all types of solar energy conversions including PV conversion, photothermal conversion and PEC conversion. Light trapping performance of absorbers is usually dependent on materials and surface structures. Mie scattering and multiple scattering can be clearly enhanced by surface microstructures and nanostructure, leading

improved light trapping performance. Material requirement and selection can be very different for different conversion types, and for example semiconductors are mainly used in PV conversion. For the photothermal conversion, different materials including semiconductors, plasmonic metal nanostructures, organic materials and carbon materials can be used. The absorber for the PEC is usually also semiconductors or oxides integrated with catalysts on the surface. In this dissertation, the main focus is to develop absorbers for solar photothermal conversion, and here Si with surface nanostructures and 3D Ag@SiO_2 hybrid plasmonic nanostructures are investigated as absorbers for the applications of photo-thermoelectric generation and photothermal water evaporation. In addition, Si with surface nanostructures integrated with ReS_2 catalyst is also investigated as photocathode of PEC for the H_2 generation.

Crystalline silicon (c-Si) that doesn't have obvious optical bandgap is able to harvest solar energy at light wavelengths below 1110 nm, or even the full solar spectrum,[33,37,38] respectively, showing potential applications in PV solar cells, photothermal water evaporation, electric power generation by photo-thermoelectric conversion, and PEC water splitting. By micro-nano-structuring of Si, the reflection below 1110 nm of c-Si can achieve as low as 1%, which largely enhances the performance of PV solar cells and PEC water reduction and oxidation reactions. Simultaneously, c-Si that doesn't have obvious optical bandgap can also show extremely high absorption in the whole solar spectrum.[33,38,39]

In addition, metal plasmonic nanostructures, such as Au, Ag, Al, Cu plasmonic nanostructures,[31,40–42] can also possess extremely high absorption in the whole solar spectrum, indicating that these kinds of materials have powerful solar energy conversion capabilities, for example, large-scale (153 cm^2) 3D Ag@SiO_2 hybrid plasmonic nanostructures with adjustable and ultra-broadband light absorption are developed by a simple and controllable two-step approach. Using 3D Ag@SiO_2 plasmonic nanostructures as a light absorber for bottom-heating-based evaporation, the

water evaporation rate remarkably improves seven times under 1 sun than that in dark condition. Moreover, when we integrate it with a commercial thermoelectric module for photo-thermoelectric conversion, it successfully converts solar energy into electric power. Our results pave the avenue for developing super large-scale Ag-based plasmonic nanostructure with potential applications in solar energy conversion.

The Chapter 2 describes the general background of solar energy conversion, summarizes the fundamentals of broadband solar energy harvesting based on photothermal conversion and its mechanism. In addition, fundamentals and mechanisms for PEC water splitting are also summarized. In Chapter 3, the experimental details for the fabrication of broadband light absorbers are presented. In Chapter 4, finite-difference time-domain (FDTD) simulations for light-absorbers interaction are introduced. In Chapter 5, we present that black silicon (b-Si) fabricated by reactive ion etching (RIE) exhibits excellent light absorption performance. When it is applied as a light absorber for photo-thermoelectric power generation, we successfully convert the solar energy to electric power via photo-thermoelectric conversion, especially solar light exceeding 1110 nm wavelength can also be efficiently used. In addition, it can be also applied for photothermal water evaporation and its average photothermal conversion efficiency (PTCE) can be as high as 73%. In Chapter 6, an efficient full-solar-spectrum 3D Ag@SiO_2 plasmonic absorber (b-Ag) was prepared for scalable photo-thermoelectric conversion based on a simple integration of light absorber and commercial thermoelectric modules. By using the b-Ag as light absorber for photo-thermoelectric power generation, it can achieve a peak voltage density as high as 82.5 V m^{-2} under a solar intensity of 100 mW cm^{-2}. Furthermore, when it is used as light absorber for bottom-heating-based evaporation, the water evaporation rate remarkably improves seven times under 1 sun than that in dark condition. In Chapter 7, by further depositing of TiO_2 on the b-Si and growing the ReS_2 on top of the TiO_2 as silicon photocathode, the ReS_2/TiO_2/b-Si shows obviously enhanced PEC performance compared to b-Si, TiO_2/b-Si and ReS_2/b-Si photocathodes

due to the suitable band alignment of b-Si, TiO_2 and ReS_2. In the final chapter (Chapter 8), we give a systematic summary of this dissertation and analyze the prospects and challenges of broadband solar energy harvesting materials.

2. State of the art

2.1 Fundamentals of broadband solar energy harvesting materials based on photothermal conversion.

Conversion of solar energy into other forms of energy is urgently needed to address the global energy issues.[43,44] It can be realized by different conversion processes, such as photovoltaic effect,[2,45–47] photochemical transformation,[48–50] photoelectrochemical process,[51–53] photothermal conversion.[17,26,32] Among these processes, photothermal conversion is a straightforward way to harvest solar energy for solar storage and conversion,[26] which allows it to derive a series of applications, such as water evaporation and purification, desalination, electric power generation, bacteria-killing, catalysis, sensors and so on. The photothermal effect, also the so-called photo-induced thermal effect, is produced by absorbing solar light and then releasing heat with the materials. These materials can be both organic materials (conjugated polymers, dyes, macromolecules) and inorganic materials (such as carbon-based materials, semiconductors, and plasmonic metals). Based on different thermal release mechanisms of light interaction with matter, we classify these materials into four groups as shown in Scheme 2-1:[23,26,32,54,55] a) Non-radiative relaxation of semiconductors; b) Plasmonic heating of metals; c) Thermal vibration of organic molecules; c) Multiple interactions of micro/nanostructured materials.

The related mechanisms of photothermal conversion of solar energy

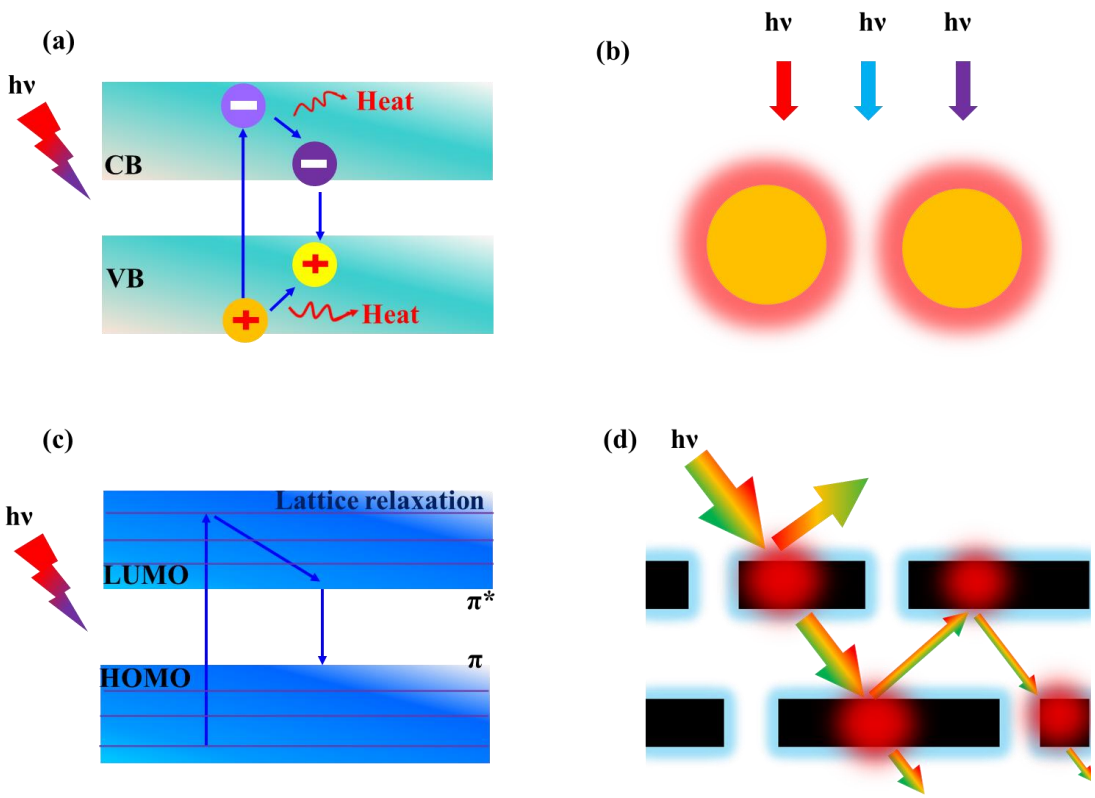

Scheme 2-1 Solar-driven photothermal mechanisms of different light absorbers. (a) The illustration for heat production from non-radiative relaxation in narrow bandgap semiconductors. (b) The illustration for heat production from localized heat in plasmonic metals. (c) The illustration for heat production from molecule vibrations in organic materials. (d) The illustration for heat production from multiple interactions in micro/nanostructured materials.

2.1.1 Non-radiative relaxation of semiconductors

Semiconducting materials convert solar energy into heat by absorbing the photon energy larger than their bandgaps, so that electrons in the valence band (VB) are able to be excited to the conduction band (CB). Next, excitation-state electrons and holes are produced in the CB and VB, respectively. Then, the excitation-state electrons and holes relax to the corresponding edges of CB and VB. As a result, the solar energy is successfully converted into heat, as shown in Scheme 2-1a. However, recombination of the excited carriers (electrons and holes) in semiconducting materials will directly lead to photothermal performance loss by releasing photons. In addition, the reflection of

light with a wavelength larger than the band edge will also lead to low photothermal conversion efficiency. Usually, by heteroatom doping or vacancy concentration regulation, the cutoff wavelengths of semiconducting materials can move towards long wavelength (redshifts) and even till the optical bandgaps disappear.

2.1.2 Plasmonic heating of metal nanostructures

Metallic plasmonic nanoparticles, such as gold, silver, aluminum, and platinum nanoparticles, have a high concentration of free electrons within the metals.[25,26,42,56–58] When the collective oscillation of the free electrons is driven coherently by the oscillating electric field of light, the localized surface plasmon resonance (LSPR) phenomenon will occur on the surface of these metals nanoparticles, leading to enhanced radiative scattering of and absorption of resonant light. In addition, near-field enhancement and hot carrier generation can also result from the decay of the collective oscillations. All these depend on many factors such as particle size, form, composition, and dielectric environment.[58–60] The relaxation of the enhanced absorption in a non-radiative way by releasing thermal energy, is called the plasmonic photothermal effect. The exact mechanism of the plasmonic photothermal effect can be understood like that: the excited electrons at a higher energy level (hot electrons) have a limited lifetime and will release the absorbed energy through electron-electron and electron-phonon scatterings and then dissipate energy in the surroundings by phonon-phonon relaxation process.[25,26] During this process, solar energy is converted into heat (Scheme 2-1b). Nanoparticles and nanostructures have a large cross-section of absorption which allows the interaction with the light on a large scale, thus, metallic plasmonic nanoparticles with a strongly LSPR effect are promising candidates for solar energy conversion by the photothermal process.

2.1.3 Thermal vibration of organic molecules

Some polymer materials and organic small molecule materials can efficiently convert photon energy into heat through lattice relaxation.[61–64] The mechanism of these kinds

of organic materials is similar to that of semiconductors.[22,25,26] Such materials usually appear to be black or dark in color. In a typical photothermal conversion process (Scheme 2-1c), the materials with abundant conjugated π bonds absorb the photon energy, and the electrons subsequently are excited from the ground state π orbit (highest occupied molecular orbital, HOMO) to a higher excited π* orbit (lowest unoccupied molecular orbital, LUMO). On one hand, heat will be released when excited electrons relax to the edge of LUMO energy level by lattice relaxation; On the other hand, when the incident photon energy matches a possible electron transition within the organic molecule, the excited electrons will come back to the HOMO energy level, leading to the heat release.

2.1.4 Multiple interactions of micro/nanostructured materials

Micro/nanostructured materials include black carbon-based materials, black silicon, black GaAs, and other black materials.[20,30,33,38,41,42,65–69] Generally, bulk materials tend to have a limited emissivity. For example, a graphite sheet without micro/nanostructures has an emissivity of ~0.85, which is not beneficial for solar energy harvesting.[25] Therefore, in order to improve light absorption of bulk materials, different micro/nanostructured materials, such as graphene, carbon nanotube, black silicon, and black GaAs nanostructures are put forward. The basic principle is to increase the times of reflections, refractions, and scatterings within the nanostructures, as presented in Scheme 2-1d.[25,32] In this principle, incident photon energy is greatly trapped in the nanostructures and almost no photons are able to escape from them. Finally, the absorbed photon energy is released into the environment by radiation, conduction and convection.

2.1.5 Hybrid mechanisms of other materials

In order to meet the demand for practical applications, many hybrid materials with hybrid mechanisms have been developed. Generally speaking, hybrid mechanisms consist of two or two more fundamental mechanisms are mentioned above. For example,

Huang et al,[70] developed one super-robust photothermal liquid metals@polymer core-shell material, which consists of plasmonic heating and thermal vibration of organic polymer mechanism during the heat production process. Zhang et al,[71] presented that the nanostructured silicon with gold nanoparticle deposition for photothermal conversion includes three fundamental mechanisms of non-radiative relaxation below the cutoff wavelength, plasmonic heating, and multiple interactions within the nanostructures in the wavelength range from 200 to 1700 nm. Li and his co-workers reported that Ti_3C_2 MXene with a characteristic absorption peak at ~800 nm can show a nearly light-to-heat efficiency of 100%,[72] which possibly referred to plasmonic heating and multiple interactions within the nanostructures.[54]

2.2 Fundamentals of broadband solar energy harvesting materials for PEC water splitting.

Fujisima et al.[73] firstly reported a PEC device for H_2 production using TiO_2 semiconducting photocatalyst. The fundamental principle of PEC water splitting is the conversion solar energy into H_2 or O_2 with the assistance of an applied bias and light illumination on the semiconducting photocatalyst, which was immersed in a suitable electrolyte. So the semiconducting photocatalyst plays an very important role during the PEC water splitting.[74] These photocatalysts tend to have several features: 1) suitable bandgap for light harvesting; 2) proper valence band (VB) and/or conduction band (CB); 3) long carrier lifetime. With such kind of photocatalyst, it can absorb enough solar light for the production of photogenerated electrons and holes, then photogenerated carriers can be easily reacted with the redox couple in the solution as long as their lifetime is long enough, or photogenerated electrons and holes will recombine with each other, leading to decreased photocatalytic activity and even inactivation. In addition, externally applied bias can speed up the slow PEC kinetics and offer sufficient energy to drive the reaction with a larger current density.

2.2.1 The related mechanism of PEC water reduction.

Semiconducting photocatalyst can convert solar energy into chemical energy by a PEC conversion process. As shown in Scheme 2-2a, it presents a PEC water reduction device. With the assistance of solar light and an applied bias, photogenerated electrons are able to jump from VB to CB, and then transfer into the electrolyte to react with H^+. As a result, double H^+ recombine 2 electrons to form one H_2 molecule at the photocathode. At the same time, four OH^- will lose four electrons to form one O_2 molecule. The whole reaction refers to PEC water splitting mechanism:[74]

$$2H_2O + h\upsilon \rightarrow 2H_2 + O_2 \quad \Delta G° = 4.92 \text{ eV } (113 \text{ kcal mol}^{-1}) \qquad (2\text{-}1)$$

$$4H^+ + 4e^- \rightarrow 2H_2 \qquad E° = 0 \text{ V} \qquad (2\text{-}2)$$

$$2H_2O \rightarrow 4H^+ + 4e^- + O_2 \quad E° = 1.23 \text{ V} \qquad (2\text{-}3)$$

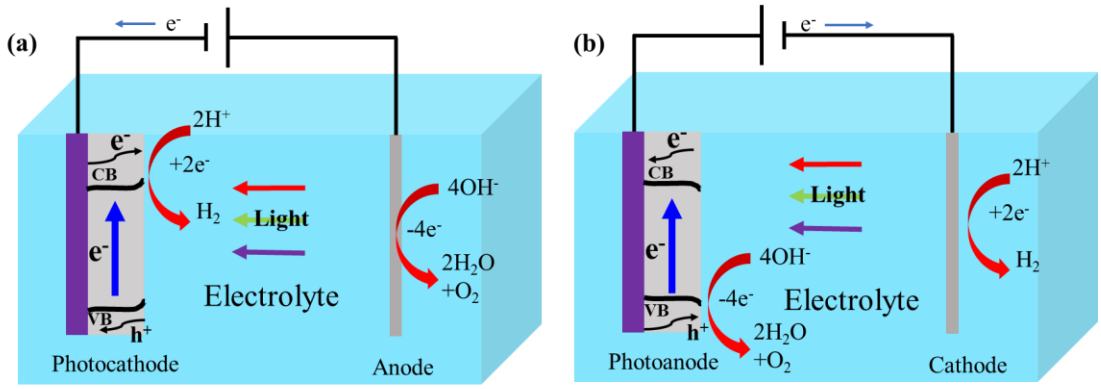

Scheme 2-2 The schematic mechanism diagram of PEC water splitting. (a) PEC water reduction. (b) PEC water oxidation.

2.2.2 The related mechanism of PEC water oxidation.

The mechanism of PEC water oxidation is similar to PEC water reduction, excepting that photocathode is replaced by photoanode, applied bias is on the contrary and the oxidation reaction is driven by holes at the photoanode. The details can be seen in Scheme 2-2b.

3. Experimental section of b-Si and b-Ag

3.1 Sample preparation

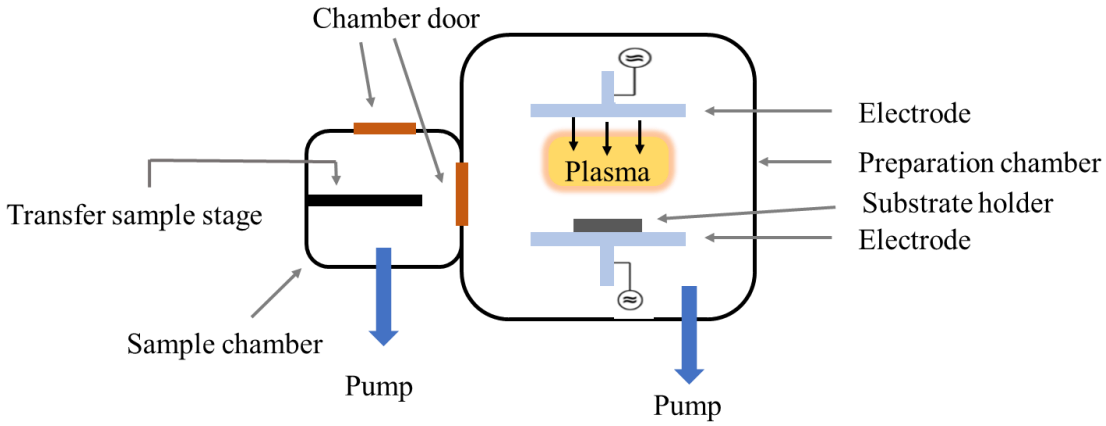

Figure 3-1 Schematic image for RIE machine.

3.1.1 Preparation of b-Si samples

B-Si was prepared by dry-etching employing a RIE system PlasmaLab 100 Oxford.[75] The 4-inch p-type B-doped Si(100) substrates with two different resistivities of 0.01 - 0.02 Ω·cm and 1 - 30 Ω·cm, respectively, and a thickness of about (525 ± 20) μm, were used to fabricate b-Si. Si wafers were directly etched without prior treatment. At first, the nitrogen (N_2) valve was opened to fill the sample chamber with nitrogen so that sample chamber (See Figure 3-1) can be opened. Then, the Si wafer was correctly placed in the sample chamber (See Figure 3-1). In next, the Si wafer was transferred to preparation chamber for RIE. Typically, during the etching process, the pressure was set as 13.33 Pa, the plasma power was set as 100 W, the temperature was kept at 20 °C, and the flow rates of SF_6 and O_2 were 79 sccm (standard cubic centimeters per minute) and 71 sccm, respectively. The etching time was varied from 0 minutes to 120 minutes in order to obtain optimized samples for light absorption. After the etching process, different Si samples were obtained.

The as-fabricated samples were treated for 20 minutes by piranha solution containing concentrated H_2SO_4 and H_2O_2 with a volumetric ratio of 3:1 to remove the contaminants on the surface of b-Si. Then, the samples were treated with HF solution for 30 seconds to remove the SiO_2 oxidation layer on the b-Si with nano-pyramidal structures.

3.1.2 Preparation of modified b-Si photocathodes

RIE of b-Si: b-Si samples were prepared the same as 3.1.1.

Plasma-enhanced atomic layer deposition (PE-ALD) of titanium dioxide (TiO_2): Prior to ALD process, b-Si was treated by HF again to remove the native oxide layer. Then, it was immediately transferred to the ALD chamber for ALD process. The deposition was conducted in an Oxford Instruments OpAL system equipped with a 300 W inductively coupled plasma source. In a typical process, Titanium (IV) isopropoxide (TTIP 99.9 %, MERCK Group, Germany) and O_2 were applied as Ti^{4+} and O^{2-} sources in a cyclic manner, respectively. The precursor dose times were 1.5 s and 8 s for TTIP and oxygen plasma, respectively. The growth per cycle (GPC) was approximately 0.043 nm. To obtain 10 nm of TiO_2, 233 cycles were applied. The ALD process was conducted under a pressure of 40 Pa at 150 °C.

Chemical vapor deposition (CVD) of ReS_2 on b-Si and b-Si/TiO_2:

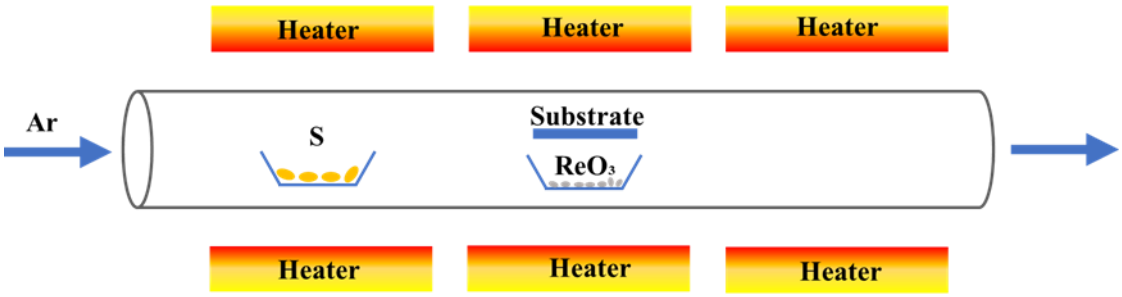

Figure 3-2 Scheme for ReS_2 growth in the CVD system.

We used a three-temperature-zone furnace (Figure 3-2) for the growth of ReS_2 on b-Si and b-Si coated by 10 nm TiO_2.[37] In a typical CVD process, 500 mg S powder was put into an alumina boat as the S precursor and then the boat was placed at the first zone. The boat with 2 mg ReO_3 was place at the middle zone and substrate was placed above the boat. The growth temperature was 500 °C and the growth time was 10 min. Details of the ReS_2 growth can be found in previous works.[76,77] After CVD growth, the samples were kept in sample boxes for PEC water splitting tests.

For CVD of ReS_2 on carbon cloth, all the conditions were kept identical as ReS_2 on b-

Si and TiO_2/b-Si, excepting that the substrate was replaced by carbon cloth.

3.1.3 Preparation of b-Ag

3D Ag@SiO_2 plasmonic nanostructures were prepared by self-assembly in a metastable ALD chamber (Oxford Instruments OpAL).[78,79] The vitreous SiO_2 substrates (Carl Roth/Menzel, Germany) with a size of 2 × 2 cm^2 and 12.7 × 12.7 cm^2 were first deposited with a 300 nm Ag film and then immediately placed into the ALD chamber for self-assembly ALD. During the MS-ALD deposition, O_2 plasma and tri(dimethylamino)silane (TDMAS, Dockweiler Chemicals, Marburg, Germany) were used as O^{2-} source and Si^{4+} source, respectively. The O_2 plasma power was set as 300 W and the substrate was kept at 120 °C during the MS-ALD deposition. The SiO_2 deposition was conducted in Oxford Plasma Technology OpAL system (Bristol, UK). For each super cycle, 300 nm Ag film was included, and 50 ms TDMAS treatment followed by 6 s O_2 was repeatedly treated for 225 cycles.

3.2 Measurements

3.2.1 Photo-thermoelectric conversion

Photo-thermoelectric conversion of b-Si: Si samples with sizes of 2×2 cm^2 and 4 × 4 cm^2 are used to test the photothermal property and thermo voltage performance. The solar simulator (LOT, quantum design) is used to illuminate AM 1.5G light on the samples, and the real-time sample's temperature is recorded by an Infrared (IR) camera (FLIR SYSTEM, Thermovision A40), which marks a maximum value in a given area. For the photo-thermoelectric investigation, a commercial thermoelectric generator (Hubei Sagreon New Energy Technology Company) with the size of 4 × 4 cm^2 was used, and the b-Si was placed on one side of the thermoelectric generator. Under illumination, the temperature of the side with b-Si was increased, and electric power is generated due to the difference of the temperatures between both sides of the thermoelectric devices.

Photo-thermoelectric conversion of b-Ag: At first, the thermal conductive tape

(Silverbead, Khasbulat Kadiev, Germany) was adhered on the aluminum heat sink (4 × 4 cm^2). In next, the thermoelectric module was mounted on the glue with good alignment. Then, the thermal conductive glue was adhered on the module again. Finally, the b-Ag sample (4 × 4 cm^2) was covered on the glue to obtain a whole photo-TE device. The photothermal electric energy generation experiments were carried out under the solar simulator (LOT, quantum design) with 100 mW cm^{-2} (AM 1.5G). During the illumination, the real-time open-circuit voltage and short-circuit current were measured by a multimeter. The outdoor experiments were conducted on June, 18th, 2021 in Ilmenau. The light intensity was calculated to be about 80 mW cm^{-2}.

3.2.2 Photothermal water evaporation

Photothermal water evaporation of b-Si: An exposed geometric area of 2 × 2 cm^2 b-Si sample is directly placed on the center of the superhydrophilic porous sponge (SPS, 3 × 3 cm^2 with saturated water) without any further treatments. The b-Si together with the SPS (b-Si@SPS) is placed in the center of the beaker. After that, DI water is slowly added into the beaker to reach about 80% height of the SPS. The remaining height of SPS is kept to ensure enough channels for efficient water evaporation. Xe lamp (LOT, quantum design) is used as the light source. For cycle test, the experiments are repeated 10 times under 100 mW cm^{-2} of AM 1.5G irradiation. The same mass of water is used for evaporation at each time, and before irradiation, the experimental set-up is naturally cooled to room temperature. The mass loss of evaporated water is recorded by the balance under the beaker. All the evaporation experiments have been conducted at room temperature (22°C±1.5°C) with a humidity of 30% ± 5%.

Photothermal water evaporation of b-Ag: The infrared (IR) images were taken by IR camera (FLIR SYSTEM, Thermovision A40). 3 SC Ag@SiO_2 plasmonic nanostructures with an area of 2 × 2 cm^2 were used to record the temperature for water evaporation experiments.

3.2.3 PEC water reduction

EC and PEC measurements

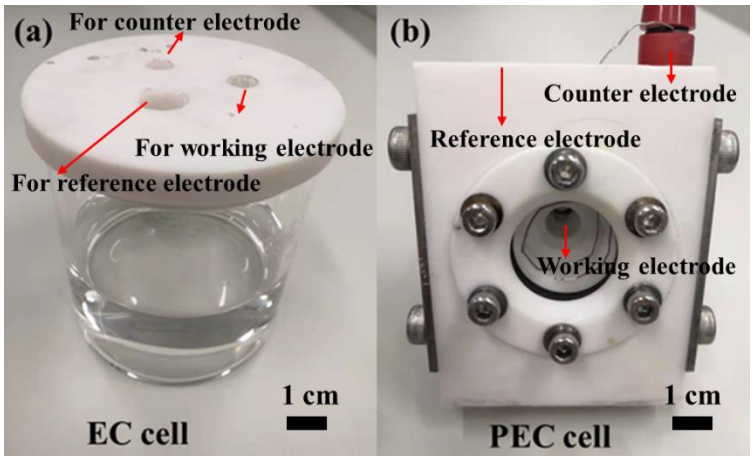

Figure 3-3 Photograph of (a) EC cell. (b) Photograph of PEC cell. The working electrode is at the back of the cell, and glass window is used to pass through light.

All the EC and PEC experiments were performed by an electrochemical workstation (VMP3, Bio Logics, France). Prior to EC and PEC experiments, the 0.5 mol L^{-1} H_2SO_4 electrolyte (pH value was measured to ~ 0.3) was purged with pure nitrogen (N_2) for more than 30 minutes. Three-electrode EC cell (Figure 3-3a) and PEC cell (Figure 3-3b) was applied to measure the polarization curve, electrochemical impedance spectroscopy (EIS) and Mott-Schottky curves. In the EC experiments, ReS_2 on carbon cloth or platinum (Pt) sheet was used as the working electrode, Pt sheet as the counter electrode and Ag/AgCl electrode as the reference electrode. For the PEC experiments, all keep the same as EC experiments except that the working electrode replaced by the Si-based photocathodes, counter electrode was used Pt wire and the EC cell was replaced by PEC cell. The In/Ga eutectic (Sigma-Aldrich) was uniformly coated on the back side of Si-based photocathode as the back contact. The Solar light (LOT, Quantum Design GmbH) was calibrated to AM 1.5G (100 mW cm^{-2}) using a certified photovoltaic cell. The potential was converted to reversible hydrogen potential (V_{RHE}) by the equation: $V_{RHE} = V_{app} + 0.197 + 0.018$ (V), where V_{app} means applied potential vs. Ag/AgCl electrode, 0.197 V is the standard reversible potential of Ag/AgCl and the 0.018 V is caused by the pH value of electrolyte. The linear sweep voltammetry (LSV) curves were measured with a scan rate of 10 mV s^{-1} from -1.5 V to 0.2 V vs the Ag/AgCl

electrode. EIS was measured at -0.9 V vs Ag/AgCl electrode with the frequency from 10^6 to 0.1 Hz. The transient photocurrent responsive curve was obtained in 5 minutes with 30 seconds light-on and 30 seconds light-off repeatedly.

3.3 X-ray diffraction (XRD) measurements

Figure 3-4 presents the details of geometrical condition for diffraction. According to Bragg's equation: $n\lambda = 2d_{hkl} \times \sin\theta$, where n is the order of diffraction, λ is the wavelength of the X-rays, d is the lattice spacing and θ is the diffraction angle. For crystalline materials, every kind of material has its own special diffraction angles, which can be used as fingerprint to identify crystallographic phase. All the crystallographic phases of the Si, b–Si and b-Ag were characterized with 2θ from 10° to 80° using a SIEMENS/BRUKER D5000 X-ray diffractometer equipped with Cu Kα radiation, corresponding X-ray wavelength of 0.154056 nm.

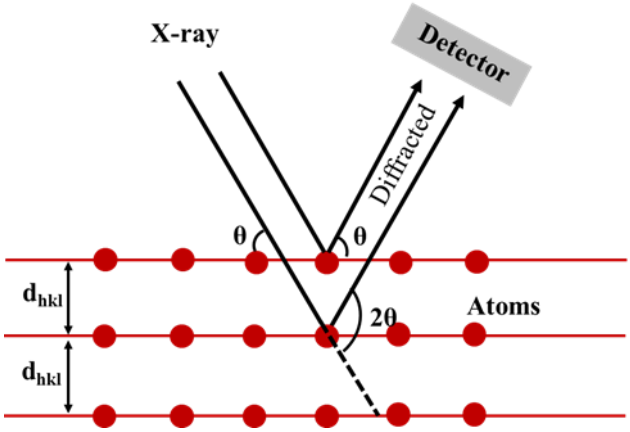

Figure 3-4 XRD condition from lattice planes. Modified from [80]

3.4 Scanning electron microscopy (SEM) and transmission electron microscopy (TEM) characterizations

All samples were firstly characterized by a cold field emission SEM (FE-SEM, Hitachi S-4800 SEM). In addition, modified Si photocathodes and b-Ag were also characterized by Zeiss Gemini 500 SEM and JEOL 6700FM SEM, respectively. TEM investigations for b-Si and b-Ag were carried out using a spherical aberration-corrected scanning TEM (STEM, JEM-ARM200F, JEOL Co. Ltd.) equipped with the cold-field emission gun

and a probe Cs-corrector (DCOR, CEOS GmbH) operated at 200 kV. The corresponding convergent and collection semiangles for High-Angle Annular Dark-Field imaging (HAADF) imaging were 20.4 mrad and 70−300 mrad, respectively. Electron energy loss spectroscopy (EELS) acquisition was performed by Gatan Imaging Filter Quantum Energy Resolution System (ERS) imaging filter equipped with a Gatan K2 camera. The collection semiangle for EELS measurements was 111 mrad. TEM characterizations for modified Si photocathode were conducted by JEOL JEM 2100 and probe-Cs corrected JEM-ARM300F2 cold Field Emission Gun (FEG) with JEOL dual silicon drift type detector (SDD) and Energy Dispersive Spectroscopy (EDS) detector (2 × 158 mm^2).

3.5 Raman spectroscopy, X-ray photoelectron (XPS) spectroscopy and UV-Vis-NIR spectrophotometer measurements

Raman spectroscopy:

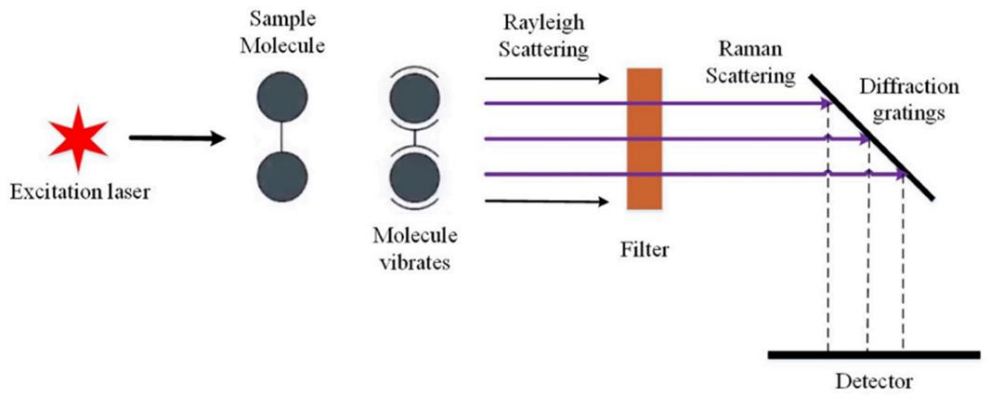

Figure 3-5 Schematic principle of Raman spectroscopy. Reproduced from[81]

Raman spectroscopy is an efficient tool for the detection of materials. The basic principle is shown in Figure 3-5. When excitation laser shines on the sample, the laser-sample interaction will produce elastic scattering (Rayleigh scattering) and inelastic scattering (Raman scattering). Rayleigh scattering is non-Raman active and should be filtered. The rest Raman scattering can be applied as fingerprint to identify materials. Raman characterizations for Si and b-Si were tested by a NTEGRA Spectra with a 532 nm laser (Spectrum Instruments Limited). Raman characterizations for modified Si

photocathode were tested by a Renishaw 42K864 system with a 532 nm laser as the incident laser beam.

XPS spectroscopy:

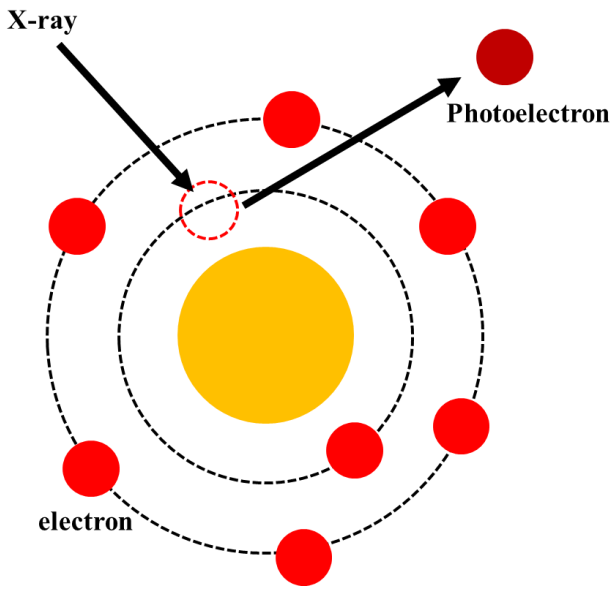

Figure 3-6 Schematic principle of XPS spectroscopy. Modified from [82]

The principle (Figure 3-6) of XPS is to irradiate the sample with X-rays, so that the inner electrons or valence electrons of atoms or molecules are excited and emitted. By detecting the kinetic energy of photoelectron, the binding energy of each element can be obtained by the equation: BE=hυ-KE-Φ, where BE is binding energy, h is Plank constant, υ is the X-ray frequency, KE is the kinetic energy of photoelectron and Φ is the work function of the spectrometer. Because every element has its own special set of binding energy, XPS can be used to determine and identify the materials. XPS full spectra and elemental fine spectra for ReS_2/TiO_2/b-Si were measured by a Thermo Fisher Scientific K-Alpha+ spectrometer.

UV-Vis-NIR spectrophotometer measurements:

UV-Vis-NIR light directly passes through an integrating sphere and vertically shines on the sample (Figure 3-7). Then, light is scattered and reflected on the sample surface. Finally, both the scattering and reflection will be collected by the detector. Therefore, UV–Vis–NIR reflection spectrum can be used to characterize the optical property of materials. In this dissertation, UV–Vis–NIR reflectance experiments were tested from

200 to 2500nm with an UV–Vis-NIR spectrophotometer (Cary 5000) equipped with an integrating sphere. Transmittance experiments were also measured by Cary 5000 in the same range.

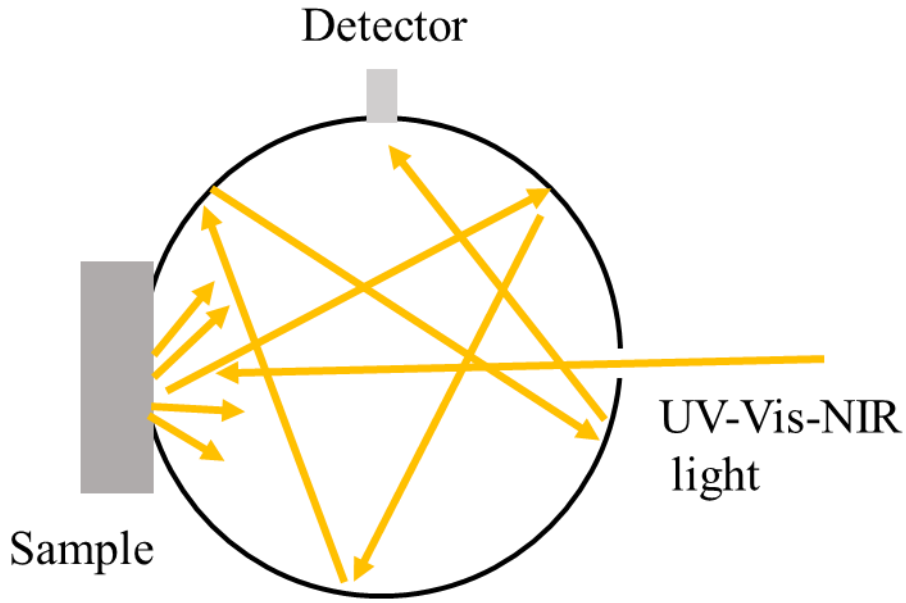

Figure 3-7 Schematic principle for the measurement of total reflectance (Ulbrich sphere). Reproduced from [83]

3.6 Wettability measurements

Wettability tests were conducted with a Drop Shape Analysis System (Krüss DSA 10 Mk2) and the volume of water drop was 10 ~ 20 μL. The contact angle between the sample and water drop is applied to determine the wettability.

4. Finite-difference time-domain (FDTD) simulations

4.1 FDTD simulation for reflection properties of Si and b-Si

The simulations related to the reflection of different silicon structures were performed by FDTD Solution (Lumerical Company).[84] Anti-symmetric and symmetric are used for x and y directions, respectively, and z-direction uses perfect match layer (PML) conditions. The dielectric index of silicon is from Palik.[85] To simplify the calculation, 4-side pyramid arrays (10 × 10 and 5 × 5) with the sizes of 0.4 μm × 0.4 μm × 0.6 μm and 0.8 μm × 0.8 μm × 1.2 μm are used for short etching time and long etching time.

4.2 FDTD simulation for reflectance and electric field enhancement of b-Si

The reflectance and electric field enhancement simulations are conducted. A simplified model with a periodic unit cell of the pyramidal b-Si structure was constructed and simulated. 4 sides pyramids with the dimension of 1.6 μm × 1.6 μm ×2.5 μm are used. For the x and y direction, the periodic condition is used for all cell boundaries. For the z-direction, a PML is used between the Si substrate and b-Si. For the reflectance and electric field enhancement simulations, the b-Si is illuminated by a total field scattered field source with wavelengths of 300 nm to 2500 nm.

4.3 FDTD simulation for modified Si photocathodes

The effect of light interaction with micro-nanostructure and the simulated reflection property were analyzed. Plane wave source with wavelength from 300 to 900 nm was applied in the simulation. For the z direction, a PML was used. And symmetric and anti-symmetric boundaries were applied for both x and y directions. The dielectric parameters of silicon were obtained from Palik.[85] The dielectric material of TiO_2 with a refractive index of $n = 2.5$ was assumed.

4.4 FDTD simulation for reflection and extinction of b-Ag

The theoretical extinction spectra were performance by FDTD simulations.[31,33] Reflection models of SiO_2 nanopillar with uniform random distribution of Ag

nanoparticles from diameter 10 nm to 50 nm were applied. The height of SiO_2 nanopillars are 200, 500 and 800 nm. Due to complicated $Ag@SiO_2$ hybrid nanostructures, simplified structures and shorter incident wavelength were used to simulate the reflection results. For x, y directions, periodic boundaries were used. A PML boundary was used in z-direction. Plane wave source illuminates toward z-axis negative direction. Mie scattering models were used to analyze the extinction effect of Ag nanoparticles with the substrate. The dielectric constants of Ag and SiO_2 were gained from Palik[85] and the dielectric constant of Ag_2O is from ref[86]. Total-field scattered-field (TFSF) source was used as the light source. The mesh accuracy of the FDTD simulation was 5 (high accuracy). Anti-symmetric, symmetric and PML boundary conditions are used for x, y, and z directions, respectively. The normalized extinction spectra were calculated by the intensity of extinction divided by the cross-section area of the simulated nanoparticles.[31]

4.5 FDTD simulation for absorption and electric field enhancement of b-Ag

3D FDTD simulation of strong localized surface plasmon resonance was analyzed. The size of the used Ag nanoparticles was based on the TEM results. The dielectric function was also obtained from Palik.[85] The TFSF source without polarization was used as the incident light source. Anti-symmetric and symmetric boundaries were used at x and y directions, respectively. A PML was applied at z direction. For simulation of 3D $Ag@SiO_2$ nanostructure with different heights, periodic boundaries were applied at x and y directions and a perfectly matched layer (PML) was applied at z direction. Plane wave source was used as the incident light source. The Ag nanoparticles with diameter from 10 to 50 nm were distributed on SiO_2 and the distribution density for each structure was kept the same.

5. Results of broadband b-Si and b-Ag micro-nanostructure for electric power generation and photothermal water evaporation

5.1 Results of b-Si with an ultra-broadband absorption for photo-thermoelectric conversion

5.1.1 Introduction of photo-thermoelectric conversion using b-Si

Structuring Si with surface micro-nanostructures for excellent light trapping can be an effective method to convert solar energy for different applications, such as photoelectrochemical water splitting, Si-based solar cells, photothermal therapy and much more.[87–89,71,90,91] Conventional fabrication methods for b-Si are mainly divided into wet chemical etching and dry chemical etching.[92–97] For wet chemical etching (mainly metal-assisted chemical etching), noble metal ions act as catalyst and hydrofluoric acid (HF) solution as etchant.[98–100] By control of the reaction time, the concentration of HF and the amount of catalyst, one can form b-Si nanostructures. Though this method (wet chemical etching) is simple, there still exists some shortages. For example, the controllability is poor, usage of toxic hydrofluoric acid is necessary, and metal contamination is a big problem.[101] Moreover, the structure of b-Si is not optimal for light trapping due to a large portion of reflection. Therefore, tailored preparation of the b-Si with almost no reflection of the whole solar spectrum can be very attractive for highly efficient solar energy conversion, and can make great impact on green energy application as well as reducing CO_2 emission.

Usually, semiconductor crystalline silicon (c-Si) can only harvest sunlight with wavelengths smaller than 1110 nm, because its bandgap is around 1.12 eV. But during the past years, b-Si for solar to thermal energy (STE) conversion has attracted the researcher's great interest.[71,102–105] However, almost all the work focused on using solar energy with wavelengths below 1110 nm and ignoring the entire solar energy above 1110 nm. Therefore, methods that also take advantage of solar energy above 1110 nm wavelength and that increase the absorption of wavelengths below 1110 nm are highly

needed. In this chapter, highly doped b-Si with surface micro-nanostructures was fabricated by a RIE method and it exhibited an excellent photo-thermoelectric conversion performance. SEM characterizations demonstrated that b-Si has plenty of micro-nanostructures on its surface. The b-Si showed extremely high absorption below 1110 nm due to multiple reflections and scatterings. The high absorption beyond 1110 nm is contributed from the enhanced free carrier absorption in the nanostructures. The related mechanism is put forward and FDTD simulation also verifies it. Furthermore, by placing an as-prepared b-Si on one side of a commercial thermoelectric generator (TEG), we successfully convert the solar energy to electric energy via photo-thermoelectric conversion process: at first, b-Si absorbs the solar energy and transforms solar energy into heat, leading to a temperature increase of one side of the TEG, while the back side of TEG still keep at room temperature; then, electric power is generated due to the temperature difference between both sides. Especially, solar energy exceeding 1110 nm wavelength can also be utilized efficiently due to the enhanced NIR absorption.

5.1.2 Results and discussion

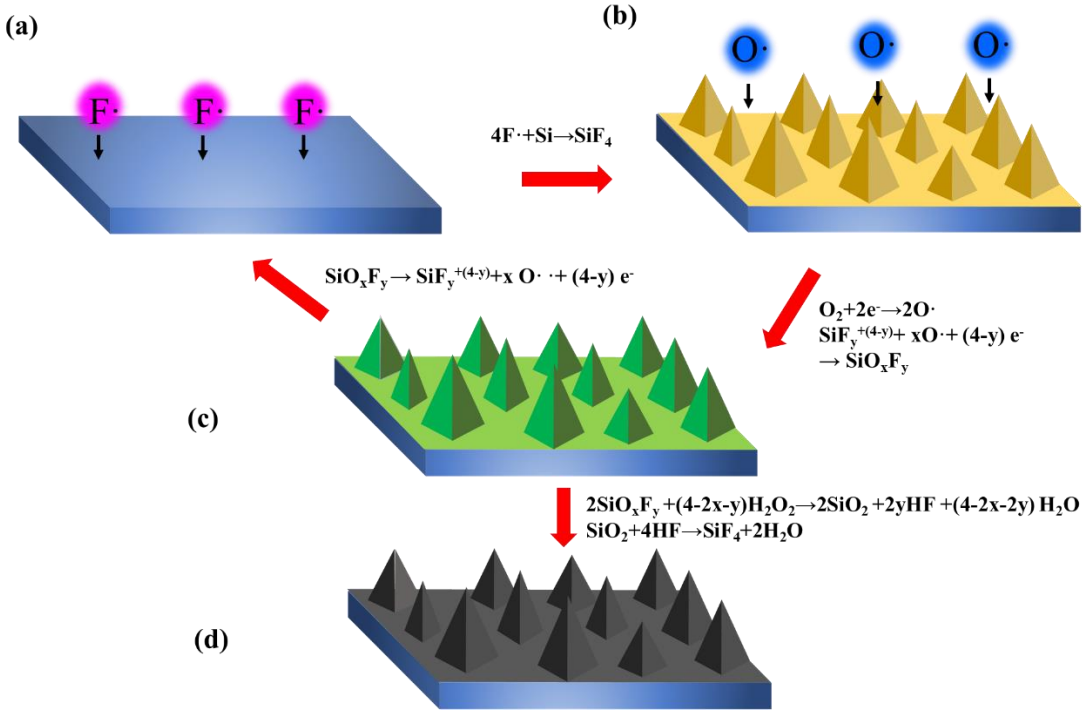

Figure 5-1 Scheme of the preparation of b-Si with rich surface texturing. (a) F· plasma etches Si substrate to produce b-Si structure. (b) O· plasma reacts with SiF_y^+ on Si surface to form SiO_xF_y passivation layer. (c) b-Si structure covered with SiO_xF_y passivation layer. (d) Clean b-Si structure.

As illustrated in Figure 5-1, the b-Si with abundant surface nanostructures is produced in the co-presence of SF_6 and O_2, and SF_6 offers fluorinated radicals (F·) and O_2 produces oxygen radicals (O·). The preparation mechanism mainly includes 4 steps:[71,92,106–108]

First, SF_6 produces the F· for etching Si structure under certain voltage conditions, then F· reacts with the Si wafer surface. Nanostructures are initially formed on the Si wafer surface.

$$SF_6+e^-\rightarrow SF_5^-+F\cdot \quad (5\text{-}1)$$

$$4F\cdot+Si\rightarrow SiF_4 \quad (5\text{-}2)$$

$$yF\cdot+Si\rightarrow SiF_y^{+(4-y)} \quad (5\text{-}3)$$

Second, one O_2 gains two electrons to form 2 O·, at the same time, the produced O· reacts with SiF_y^+ to produce the SiO_xF_y passivation layer. The passivation layer can

protect the pyramids from being further etched, and thus can keep the pyramids shape.

$O_2 + 2h\nu \rightarrow 2O\cdot$ (5-4)

$SiF_y^{+(4-y)} + x\ O\cdot + (4-y)\ e^- \rightarrow SiO_xF_y$ (5-5)

Third, the unstable SiO_xF_y decomposes to SiF_y^+ and $O\cdot$ again, removing the protection layer of the sample and making therefore further etching possible. Then the etching process returns back to the first step. The cycle etching process is finished as soon as the sample satisfies the requirement.

$SiO_xF_y \rightarrow SiF_y^{+(4-y)} + x\ O\cdot + (4-y)\ e^-$ (5-6)

Fourth, once the cycle etching process is finished, there are plenty of contaminants on the sample's surface. It is cleaned up by piranha solution. At last, HF is used to remove the silicon oxide.

$2SiO_xF_y + (4-2x-y)\ H_2O_2 \rightarrow 2SiO_2 + 2yHF + (4-2x-2y)\ H_2O$ (5-7)

$SiO_2 + 4HF \rightarrow SiF_4 + 2H_2O$ (5-8)

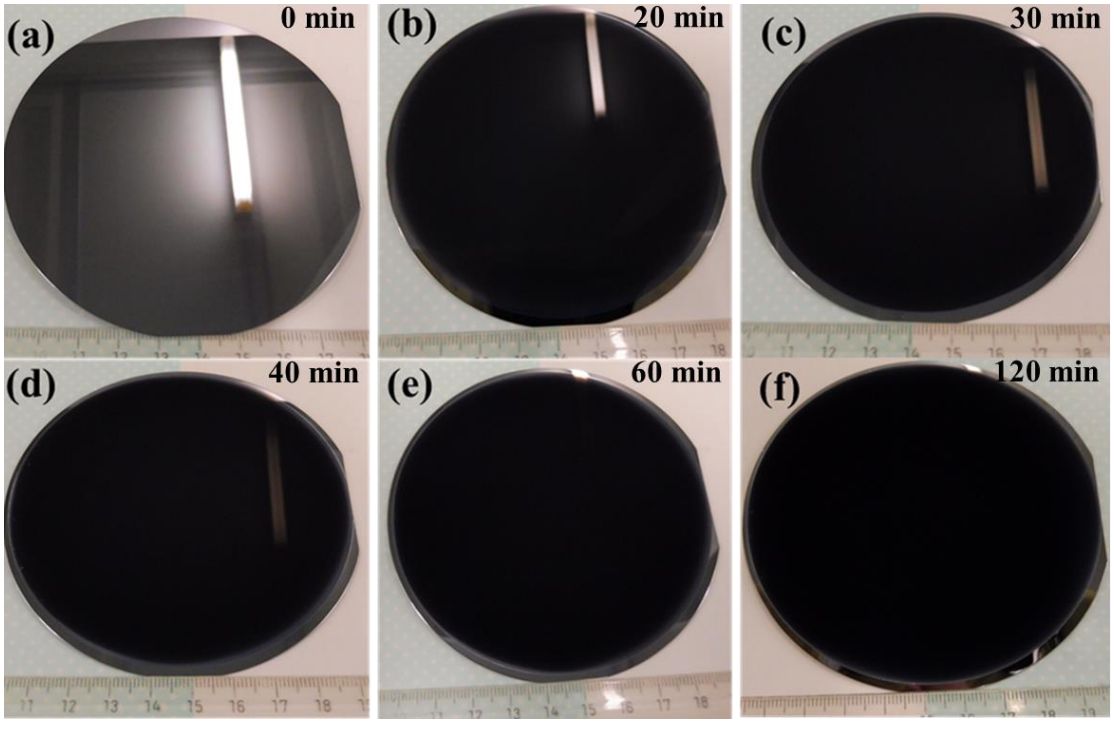

Figure 5-2 (a)~(f) 4-inch Si substrates after different etching time. (a)-(f) t=0 min, 20 min, 30 min, 40 min, 60 min and 120 min. The white bars in a, b, c and d are fluorescent lamps.

In terms of reflecting white fluorescent light, the intensities of reflection gradually

become weaker and weaker as the etching time becomes longer. As shown in Figure 5-2a, when the light illuminates on the surface of pristine Si, it looks like a mirror that most part of light can be reflected so that it can be seen by human eyes. However, when the etching time increases to 20 min, 30 min and 40 min, more and more light is absorbed by the b-Si, corresponding that less and less light is reflected by it. It is worth noting that there is almost no light seen by human eyes as the time are prolonged to 60 min, or 120 min. To get a better understanding of what causes the differences, SEM characterizations of b-Si samples with different etching time have been conducted.

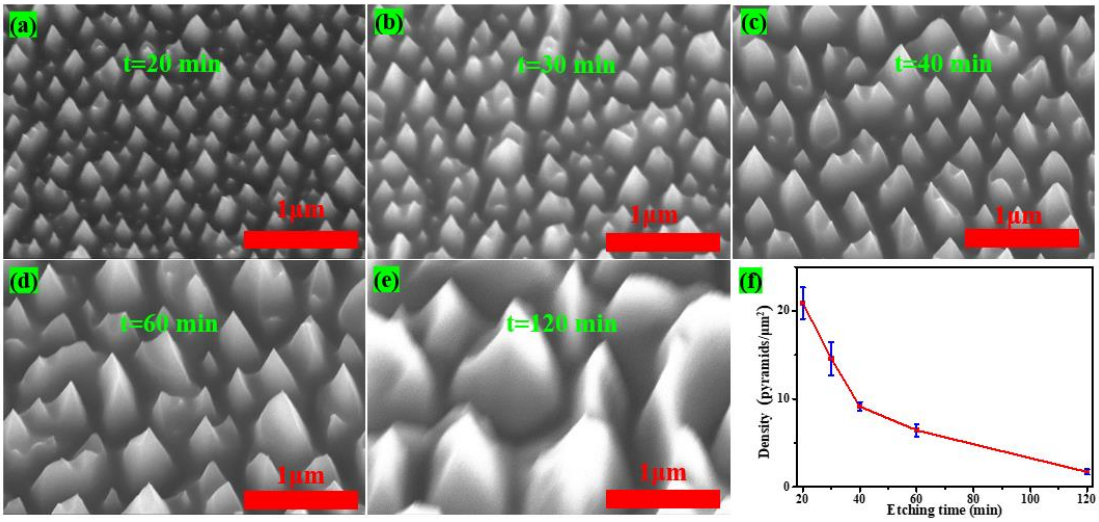

Figure 5-3 (a)-(e) SEM pictures with a tilt angle of 20° of abundant surface nanostructure for different etching time from 20 min to 120 min. (f) density of pyramids of each SEM picture from (a) to (e).

Figure 5-3 presents SEM pictures with a tilt angle of 20° of abundant surface nanostructures for different etching times from 20 min to 120 min by RIE processing. From Figure 5-3a, we can observe that there are lots of pyramids with several hundred nanometers length and height distributing on the surface of b-Si with the etching time of 20 min. As the etching time is extending (Figure 5-3b, 5-3c, 5-3d and 5-3e), the size of the nanopyramids gradually grows. The height of the pyramids slowly increases from about 100-200 nm to about 1-2 μm. A similar phenomenon can be found for the length of the pyramids. At the same time, the Si pyramid density (Figure 5-3f) varies from 20.9 ± 1.8 pyramids/μm^2 for the etching time of 20 min to 1.7 ± 0.3 pyramids/μm^2 for the etching time of 120 min.

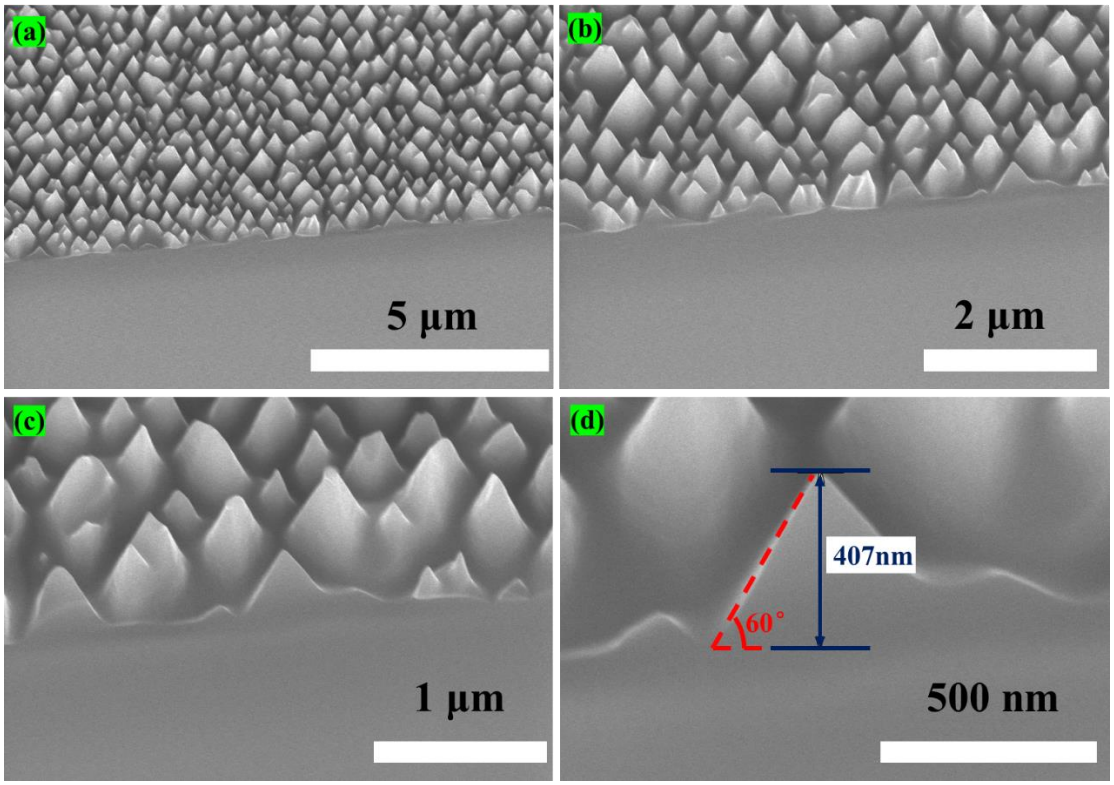

Figure 5-4 (a)~(d) Cross section SEM micrographs at different magnifications of b-Si pyramids with 60 min etching time.

In order to further understand the morphology of the b-Si, the cross section of the sample with a 60 min etching was characterized. As shown in Figure 5-4, different magnifications of SEM pictures indicate that the b-Si pyramids uniformly distribute several hundred nanometers in size and covers the whole surface of the substrate. There is almost no space between two b-Si nanopyramids, and they stand close to each other. Linear measurement on one exemplary pyramid showed that the height between the top and the bottom of the nanopyramid is 407 nm and the tilt angle is about 60°. Owing to the fact that the height and tilt angle of the b-Si nanopyramid determine the number of scattering events and the scattering angle at the same time, the height and tilt angle of nanopyramids are two key factors for the excellent light trapping property of the b-Si.[108–110] These results are well consistent with above characterizations, which indicate that the longer etching time results in lower reflection.

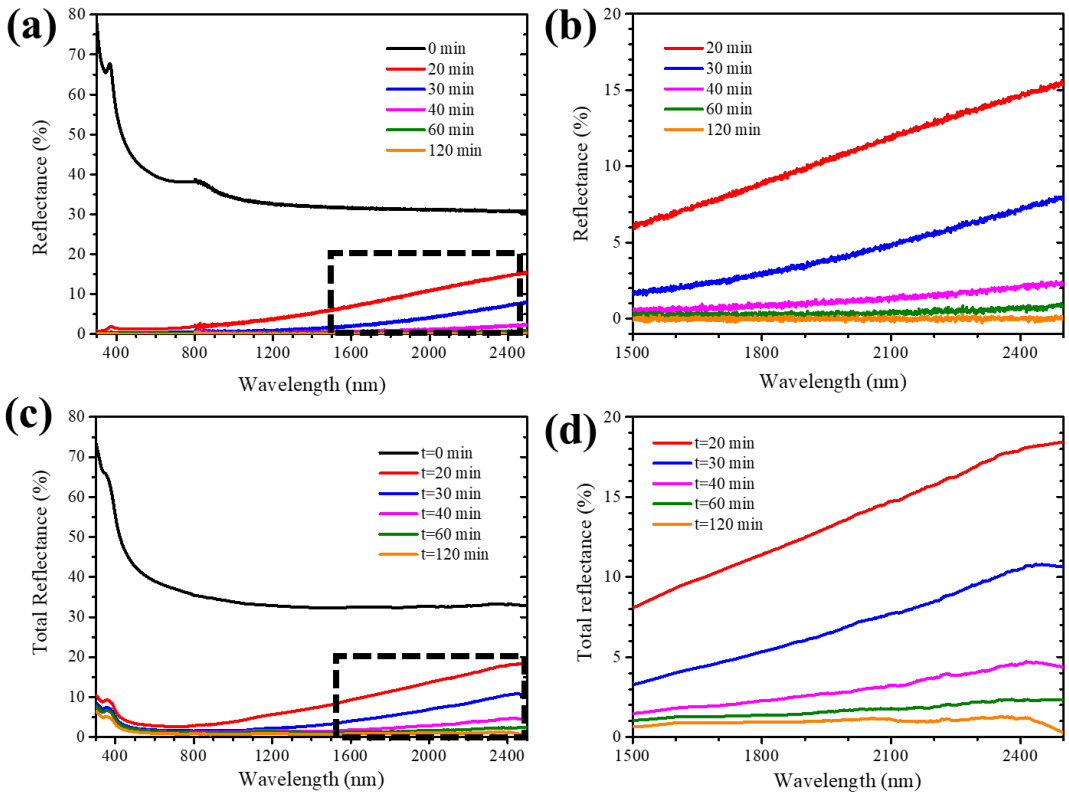

Figure 5-5 (a) Specular reflectance spectrum for different RIE etching times of the Si samples. (b) Enlarged area from (a), which is marked by black rectangle. (c) Total reflectance spectrum for different RIE etching times of Si samples. (d) Enlarged area from (c), which is marked by black rectangle.

To optimize the reflection performance of b-Si with rich surface nanostructures, different etching times of b-Si samples are analyzed. Figure 5-5a and 5c show the both specular reflectance and total reflectance of the samples. More than 30% of incident light is reflected in the pristine wafer without etching. After etching for 20 min by RIE, the reflectance of b-Si decreases sharply to less than 16% in the whole range from wavelength 300 nm to 2500 nm. The reflectance of b-Si decreases further with increasing etching time. Especially for the NIR range from 1500 nm to 2500 nm, the reflectance in NIR range is decreased less than 0.1% for the sample etched with 120 min, as shown in the enlarged images of Figure 5-5b and 5-5d. It should be noticed that the total reflectance is little higher than the specular reflectance due to additional diffuse reflection. Table 5-1 shows its excellent total reflection performances and research status among the previous reported black silicon materials.[71,87,93,111–113] The transmission spectrum of silicon samples with different resistivities show clearly

distinct transmission properties (Figure 5-6a). The transmission intensity of pristine Si with a resistivity of 1 to 30 Ω·cm increases rapidly near the Si cut-off wavelength, whereas there is no obvious change in the Si sample with a resistivity from 0.01 to 0.02 Ω·cm. This is due to clearly enhanced phonon-assisted absorption and free-carrier absorption in the Si with higher doping density.[39,114] This behavior can be also found by comparing the reflection spectra of the Si samples with resistivities of 1 - 30 Ω·cm and 0.01 - 0.02 Ω·cm (Figure 5-6b). The almost perfect light trapping performance of optimized b-Si from this work is also compared with other "black" materials (Table 5-1).[115–119] The absorption (Figure 5-6c) is calculated by using the formula: Absorptance (A) + Reflectance(R) + Transmittance(T) = 1.[120]

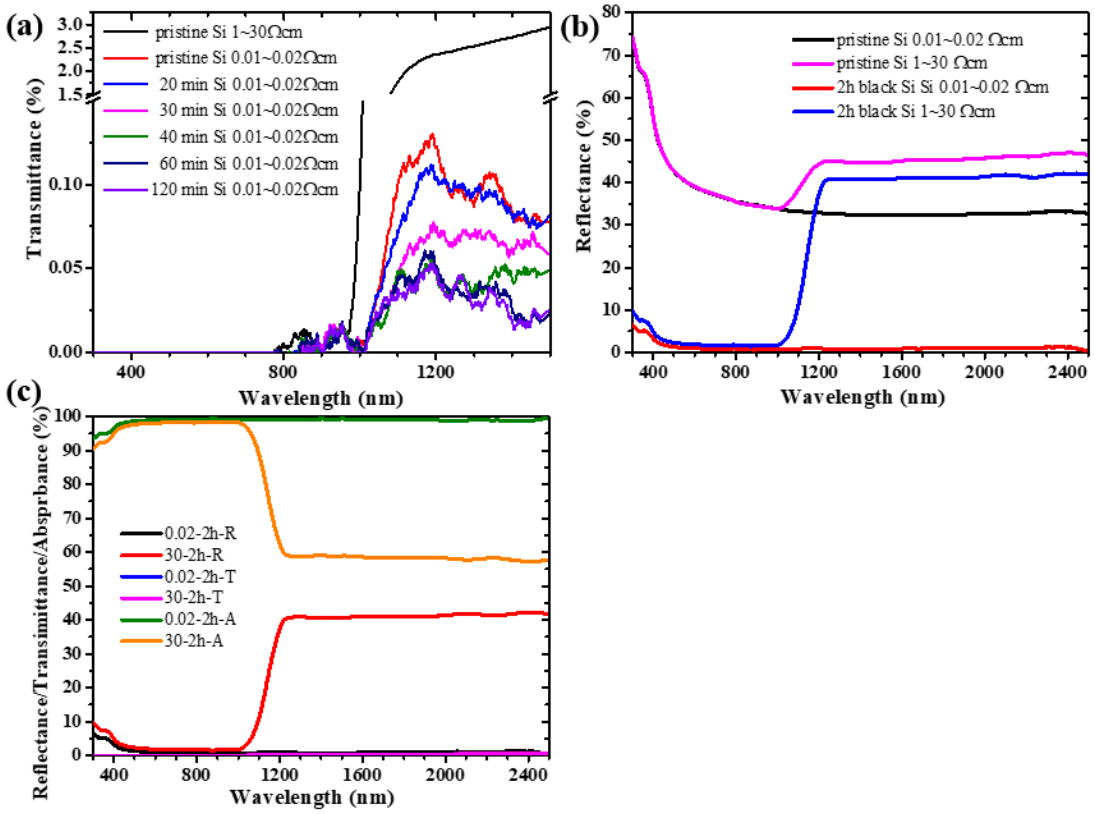

Figure 5-6 (a)Transmission spectra of different Si samples (The thickness is 525 ± 20 µm). 2 different doping levels (1-30 Ω·cm and 0.01-0.02 Ω·cm) of the Si wafers are shown. The treated b-Si is always done for the highly doped Si wafers (0.01-0.02 Ω·cm), the various treatment times are given in the legend of the graph. (b) Reflection spectra of different Si samples. (c) Reflection (R), transmission (T) and absorption (A) spectra of the as-prepared b-Si-2h samples. 0.02-2h means 0.01~0.02 Ω·cm Si sample with etching time 2 hours; 30-2h means 1~30 Ω·cm Si sample with etching time 2 hours.

Table 5-1 Research current situation compared to recently reported black silicon.

Total reflectance			Fabrication method[a]	Application	References
AR	λ=600nm	λ=1200nm			
1.1%	**1.2%**	**0.8%**	**RIE**	**P-TE**	**This work**
<5%	~3%	>12%	CE	PEC	Ref.[87]
8%	~1%	>50%	PL+RIE	PT + P-TE	Ref.[71]
>5%	~3%	>12%	MACE	PV	Ref.[93]
4%	2.6%	\	RIE	PV	Ref.[111]
3.9%	~2.6%	>20%	MACE	PEC	Ref.[112]
~0.3%	~0.5%	~0.4%	ECR-PE	\	Ref.[113]

a: CE: chemical etching; PL: photo lithography; MACE: metal-assisted chemical etching; ECR-PE: electron cyclotron resonance plasma etching. P-TE: photo-thermoelectric conversion; PEC: photoelectrochemical conversion; PV: photovoltaic conversion.

To better understand the reflection principles of b-Si with rich surface nanostructures, we choose the sample's etching time of 20 min and 60 min as the ideal models and the untreated Si as the reference. As is described in Figure 5-7a, when the incident light illuminates on the pristine Si sample, the reflected light can be easily reflected from the polished surface. Figure 5-2a also verified this. This phenomenon could be well explained by geometric optics. However, the sizes of b-Si surface nanostructures are similar to the light wavelengths, leading to largely enhanced scattering (Mie scattering).[121,122] As is illustrated in Figure 5-7b and 5-7c, most of the scattering behavior belongs to forward scattering,[123] and a tiny part is the backward scattering.[124] The forward scattering light leads to strong absorption by b-Si structure, while the backward scattered light was also detected (as the little difference between the specular reflection and total reflection in Figure 5-5a and 5-5c). When the structural height increases with increasing etching time, multiple scattering or more times of scattering can occur and absorption is further increased.

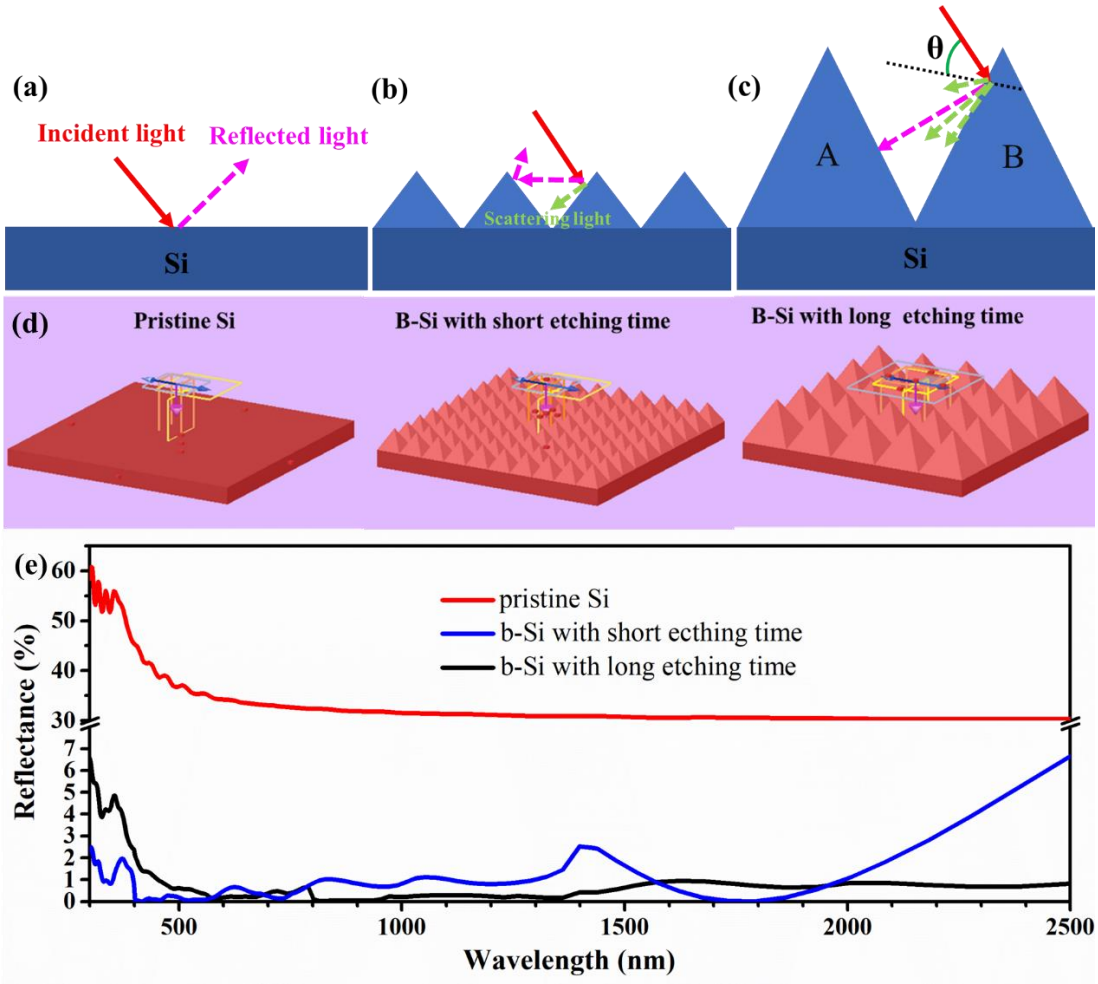

Figure 5-7 Schematic picture of different Si structures for illustrating the reflection principle. (a) Polished Si surface. (b) b-Si with short etching time. (c) b-Si with long etching time. (d) FDTD simulation model based on (a), (b), and (c). (e) FDTD simulation results with pristine Si, b-Si with short etching time and b-Si with long etching time.

But it is very interesting to notice here that the absorption in NIR range, which is clearly beyond the band edge of Si (1110 nm), is also highly enhanced. This is mainly due to the free carrier absorption in which the transfer of photon energy to an electron or hole in the semiconductor conduction or valence band is involved.[39,113,125,126] Free carrier absorption increases or even becomes significantly strong when the doping density increases. However, the NIR absorption increases dramatically with increasing structural height of the b-Si (Figure 5-5b and 5-5d), indicating that free carrier absorption is clearly enhanced in the nanostructures. So the large NIR absorption beyond the band edge is resulted from the combined effect of high doping density and nanostructures. Furthermore, the FDTD simulation results also confirm these results.

As shown in Figure 5-7d and 5-7e, planar Si shows a large reflection, however, b-Si with short and long etching time indicate a relatively low reflection and the latter generally obtains the lowest reflection. Thus, the simulation results are almost agreed with reflection measurements.

Photothermal and photo-thermoelectric experiments have been conducted to verify the excellent light trapping performance of b-Si with abundant surface micro/nanostructure. Figure 5-8a shows the schematic picture of photothermal effect experimental set-up. The solar light vertically irradiates on the sample and an infrared (IR) camera on the top right records the real-time samples' surface temperature information. According to Figure 5-8b, when the solar light (AM 1.5G, 100 mW cm^{-2}) shines on the samples, both the bare Si and b-Si surface temperature rise rapidly in the first 5 minutes, then their surface temperature gradually increase during the last 25 minutes. However, the b-Si shows a faster surface temperature ascent rate in the first 5 minutes and ends with higher surface temperature at 53.8 °C than bare Si, which has a lower surface temperature rise and final surface temperature of 45.6 °C. Figure 5-8c shows the schematic diagram of how the photo- thermoelectric device produces the electric power. Thermoelectric (TE) device produces electrical power by the temperature differences between upper and lower surface. As is presented in Figure 5-8d, when there is no sample on the TE device, it can hardly produce the voltage under the AM 1.5G 100 mW cm^{-2} solar light irradiation. The voltage produced by TE device shows the similar phenomenon compared to the surface temperature. In the first 5 minutes, as-produced voltage by the bare Si and b-Si reach the highest at 36 mV and 65 mV, respectively, and then keep stable voltage with a little decrease due to the temperature diffusion to the TE device back side and heat balance with the environment. With the irradiation intensity increasing from 100 mW cm^{-2} to 500 mW cm^{-2}, the maximum open circuit voltage of TE device with b-Si tend to rise (Figure 5-8e). This way can be a good method to increase the maximum open circuit voltage of TE device with b-Si and also an efficient method to enhance photothermal seawater desalination.

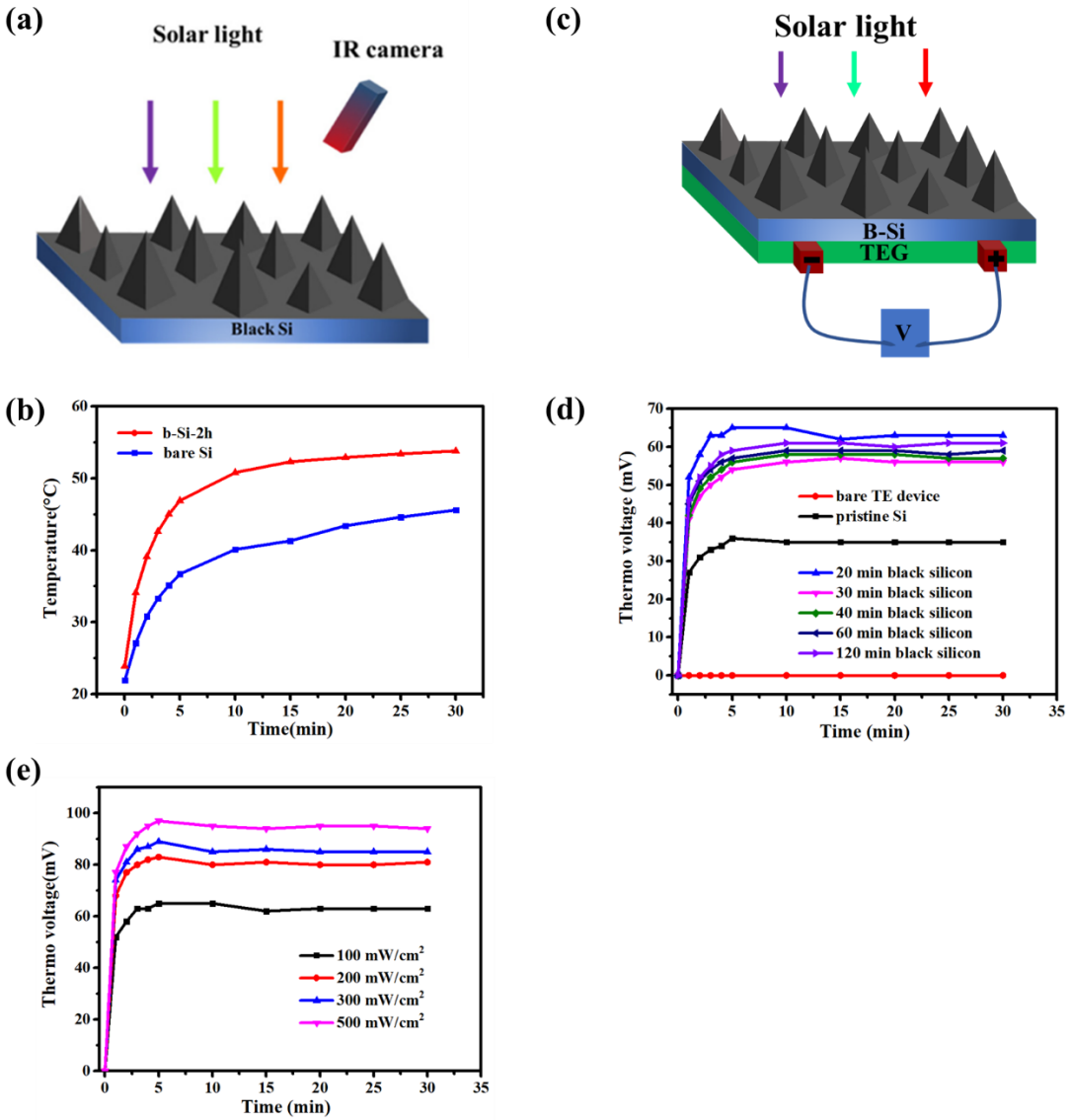

Figure 5-8 (a) Schematic picture of photothermal experimental set-up. (b) Si samples surface temperature under simultaneous AM 1.5 solar light irradiation. (c) the schematic diagram of the photo-thermoelectric device. (d) the open circuit voltage of b-Si with low resistivities and different etching time under the AM 1.5G solar light irradiation. (e) the open circuit voltage of b-Si with 120 min etching time under the different solar intensities. Low resistivity Si samples are used in e and f.

The photo-thermoelectric performance of Si with different resistivities are also compared, and the b-Si with low resistivity (highly doped) demonstrates clearly stronger photo-thermoelectric performance (Figure 5-9). But the only difference between highly doped and lightly doped Si in the reflectance spectra is that a stronger reflectance appears in the lightly doped Si for the range with wavelength above 1110 nm (Figure 5-6c). This means that enhanced light absorption of Si in the range with

wavelength above 1110 nm helps clearly for the electric energy conversion.

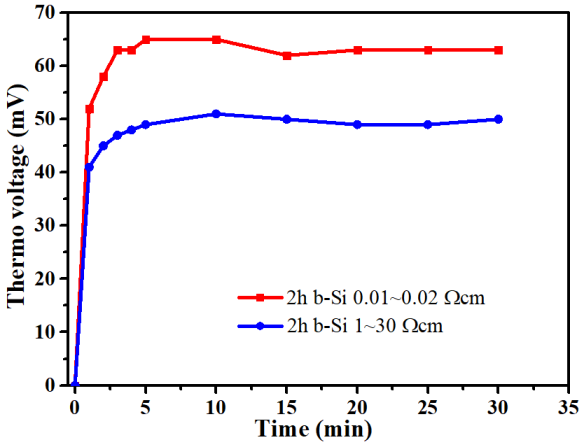

Figure 5-9 The absorption performance of b-Si-2h samples with different resistivities as measured by the thermo voltage of the TEG. The lines are only to guide the eye.

5.1.3 Conclusion

In summary, surface nanostructured b-Si with excellent light trapping performance has been prepared by self-masking RIE method. The optimized b-Si sample demonstrates a specular reflection rate lower than 0.1% and the average of total reflection (specular reflectance + diffuse reflectance) being about 1.1%. The excellent light trapping performance of the b-Si is due to multiple scattering of light and enhanced free carrier absorption in the nanostructures. By using the prepared b-Si structures on a thermoelectrical generator, we successfully demonstrated a significantly higher conversion rate from solar energy to electric power. Especially solar energy exceeding 1110 nm wavelength, i.e. above the band gap, can also be utilized efficiently. The excellent light trapping of b-Si structures with high controllability and large-scale preparation shows great potentials on photothermal effect applications in photo-thermoelectric conversion, photothermal imaging, photothermal seawater desalination and so on.

5.2 Results of black silicon with an ultra-broadband absorption for photothermal water evaporation

5.2.1 Introduction of photothermal water evaporation using black silicon

Solar energy conversion is one of the hottest topics to address the global energy challenge, and lots of scientists have been contributing to searching for new materials for broadband solar energy harvesting due to the inexhaustible source of solar energy.[25,127–135] Solar to heat conversion, also called photothermal conversion, is one of the most important forms among the solar energy conversions, besides Si-based photovoltaic cell, perovskite solar cell, photoelectrochemical water splitting and so on.[31,32,87,136–141] It also ensures wide spread applications including photothermal imaging, seawater desalination as well as photo-thermoelectric conversion.[119,142–145] Photothermal water evaporation is of great significance to take full advantage of solar energy without any other energy input. However, most of the reported materials have more or less problems towards gaining high quality and high-efficiency for photothermal water purification or desalination.

One possible solution is to design a photothermal system that is capable of addressing above concerns. Several principles should be considered.[32,146,147] First, the photothermal material must show a broadband absorption.[32] In order to ensure a high photothermal conversion efficiency (PTCE), an overall absorption above 97% in the wavelength range from 300 nm to 2500 nm is expected. At the same time, the average absorption ability of this material towards solar light should be as high as possible.[115,148–150] Second, the water uptake part should have a certain degree of thermal-insulating to avoid thermal loss.[32] Then, there should be enough water transportation channels for water vapor transporting for efficient evaporation. Furthermore, the evaporated water must not contain any toxic elements from the photothermal system. Finally, the applied materials must be earth-abundant and affordable for large-scale industrial applications.[115,32,146,149]

In this chapter, we report a non-toxic, highly efficient, low cost and broadband

absorptive photothermal converter. Employing the reactive ion etching (RIE) method, we prepare an ultra b-Si sample with a super high solar absorption capability of about 98.7% across the wavelength from 300 nm to 2500 nm.[151] This result indicates a better advantage than the reported photothermal materials. By combining the b-Si with a SPS as a photothermal converter, we achieve a high PTCE of about 73% under the AM 1.5G of 100 mW $\cdot cm^{-2}$ solar intensity. Finite difference time domain (FDTD) simulation results confirm that the light absorption of b-Si surface nanostructure is very high due to the improved electric field enhancement (EFE) within the b-Si structures. In addition, multiple reflections and free carrier absorption are also important factors according to our previous work.[151]

5.2.2 Results and discussion

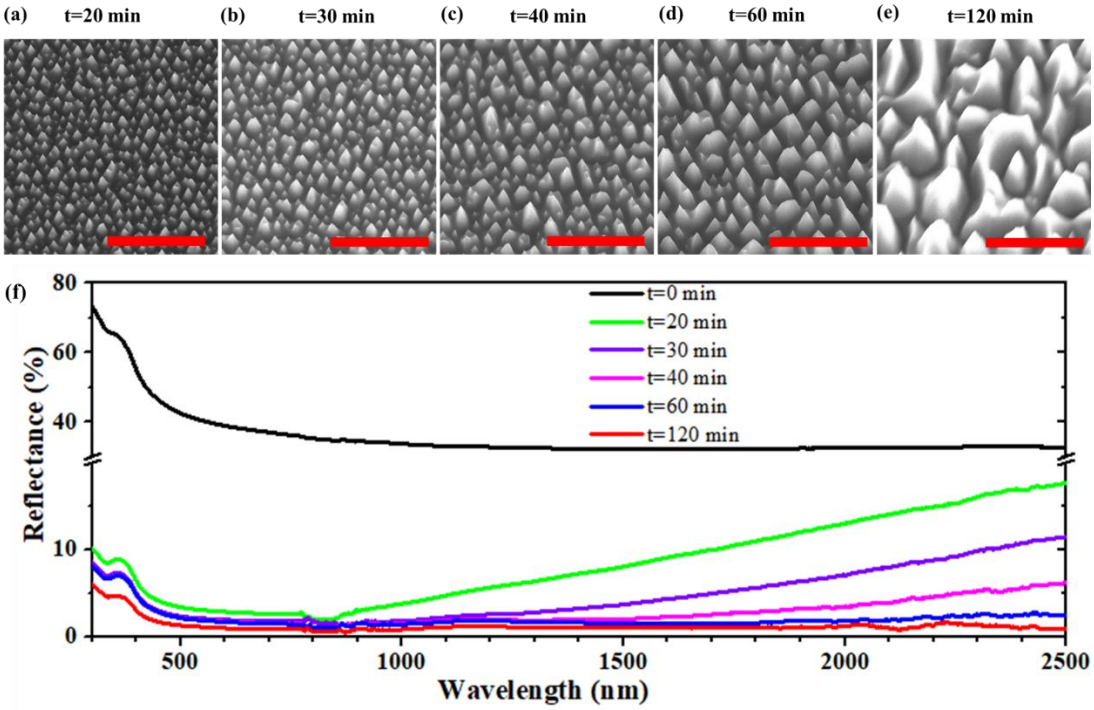

Figure 5-10 (a)~(e) SEM images at 20° tilt angle of the ultra b-Si surface nanostructures with etching times from 20 min to 120 min. Scale bars are 2 μm. (f) Reflectance spectra in the wavelength range from 300 nm to 2500 nm for the Si samples prepared with different etching times.

In a typical b-Si preparation experiment, b-Si nanostructures with broadband light absorption performance are controlled by the etching time using the RIE method. The SEM images with the same magnification present different sizes and densities as the etching time increases from 20 min to 120 min (Figure 5-10a ~ 10e). In Figure 5-10f, pristine Si sample shows the highest reflectance among the different etching time of Si samples. Once the Si samples are etched, a sharp decrease appears for the Si sample with an etching time of 20 minutes. For longer etching times, the reflectance of Si samples gradually reduces and the sample with an etching time of 120 minutes shows the lowest reflectance, which indicates that this sample gains the best solar energy harvesting capability among all Si samples. Therefore, the b-Si sample with an etching time of 120 minutes is chosen for the photothermal conversion experiments. For this sample, also more detailed scanning electron microscope (SEM) and transmission electron microscope (TEM) characterizations have been carried out. As is presented in

Figure 5-11a-c, the top-view of the b-Si surface distributes a lot of highly uniform micro/nanostructures. The micro/nanostructures of vertical and horizontal lengths have a large range from several hundred nanometers to more than one micrometer. Figure 5-11 d-f shows the side-view of as-prepared b-Si with abundant surface texturing, which indicates their three-dimensional (3-D) structures and looks like rolling hills of different sizes. All the SEM characterizations confirm that relative larger size hills gain the longer light travel distance and thus lead to multiple forward scatterings as well as light localization, which should be responsible for nearly perfect light-harvesting capability.[108,149] Figure 5-11g shows a Si pyramid lying on a TEM grid, which is scratched from the b-Si sample. Figure 1h presents the TEM image of the enlarged area in Figure 5-11g's blue rectangle. We observe some nanostructures on the Si pyramid. The high-resolution TEM (HRTEM) picture in Figure 5-11i verifies that the monocrystalline silicon is surrounded by a native oxide layer with a thickness of several nanometers. The corresponding Fast Fourier transform (FFT) pattern indicates its good single crystallinity.

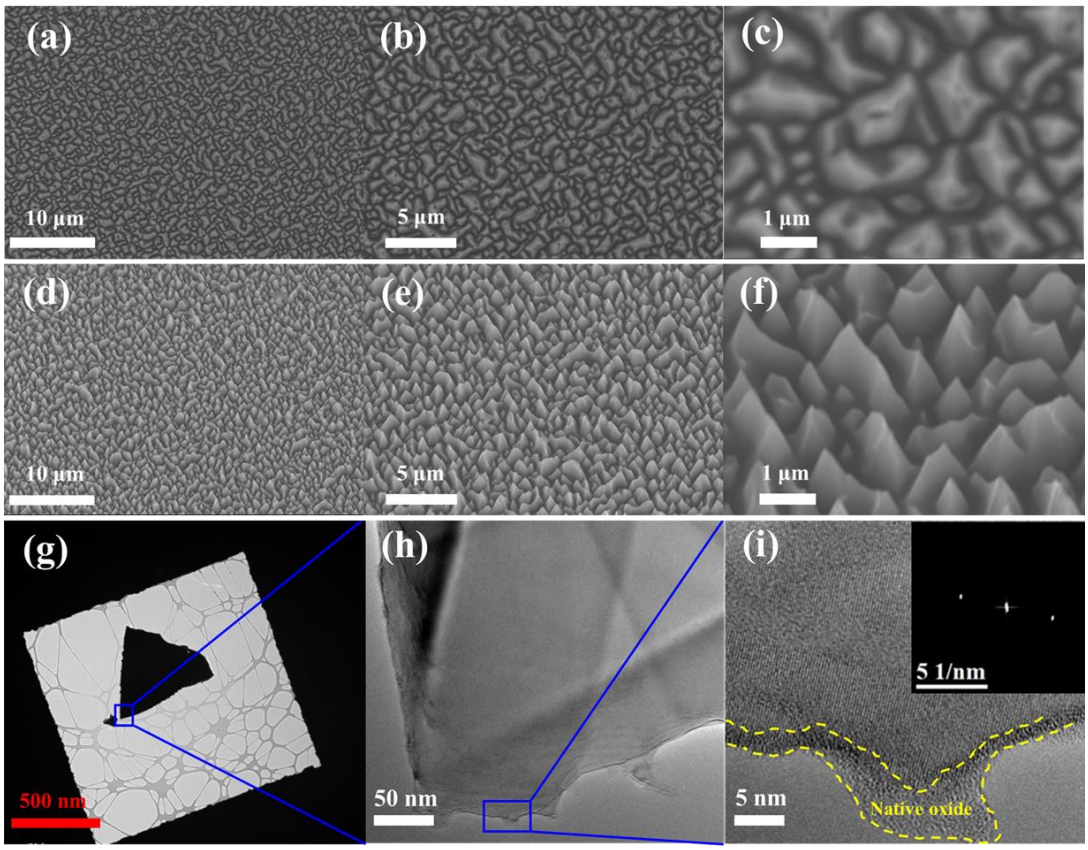

Figure 5-11 (a)~(c) Top view SEM images of the as-prepared b-Si micro/nanostructure

at different scale. (d)~(h) Side view SEM images at a tilt angle of 20 degrees of the as-prepared b-Si micro/ nanostructure at different magnifications. (g) TEM image of a pyramidal b-Si micro/nanostructure lying on a TEM grid. (h) Close-up TEM micrograph of the blue-marked square in (g). (i) High-resolution TEM image of the blue-marked rectangle in (h). The two yellow dashed lines delimit the native oxide layer of the monocrystalline silicon. The inset shows the corresponding FFT pattern.

Single crystalline silicon has a typical sp^3 hybrid diamond structure with a lattice constant of 0.543 nm. As is shown in Figure 5-12a, one silicon atom is equally connected to four other silicon atoms by covalent bonding. X-ray diffraction (XRD) and Raman measurements are conducted to investigate the crystalline structure of the pristine Si and b-Si samples. Figure 5-12b shows the XRD patterns of the pristine Si and b-Si samples. Both samples show the strongest peak intensity at 69.3° of the (400) reflection, which indicates good monocrystalline before and after etching[151–153] and is confirmed by Raman measurements (Figure 5-12c). The strongest vibration at 520 cm^{-1} show Si-Si bond vibrations.[154] Because of the strong field enhancement (see FDTD simulation below) leading to strong light absorption, the Raman intensity of b-Si is obviously lower than the pristine one.

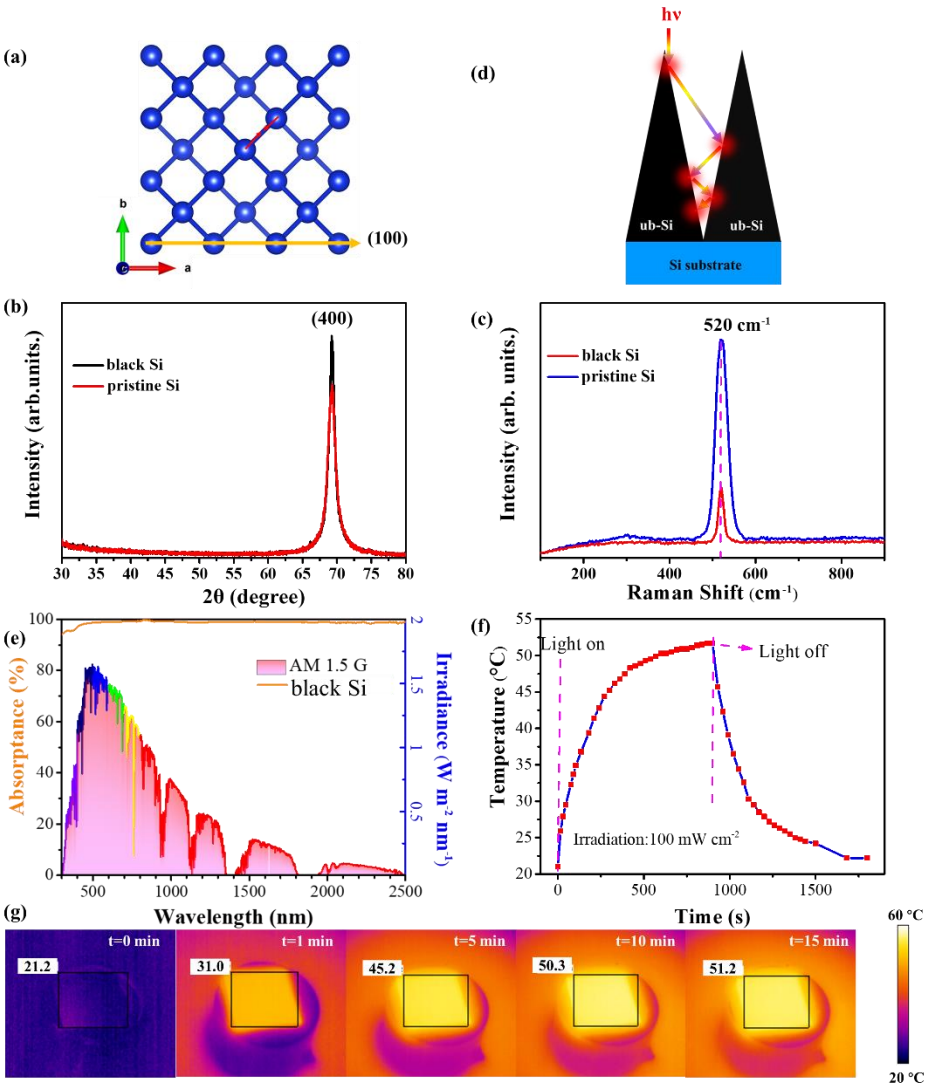

Figure 5-12 (a) Schematic diagram of the silicon crystal structure from z axis. (b) XRD patterns of the pristine Si sample and b-Si sample. (c) Raman measurements of the pristine Si sample and b-Si sample. (d) Schematic diagram of how the heat produces during the light interacting with the b-Si (e) Absorptance of the b-Si sample from wavelength 300 nm to 2500 nm. The inset is AM 1.5G solar spectrum. (f) b-Si surface temperature changes by time when lighting on or off the Xe lamp under an optical density of 100 mW cm^{-2} (1 sun). (g) The real-time b-Si surface temperatures are monitored by an infrared (IR) camera at the first 15 minutes in Figure f.

Figure 5-12d shows the mechanism of how typical ultra b-Silicon micro/nanostructure materials transfer solar energy to heat.[25,32,115,147] By creating a micro/nanostructure on a flat silicon surface, the optical path length is increased yielding a stronger light absorption. When the incident light wavelength is similar to the size of the micro/nanostructure, light can be largely scattered (Mie scattering). Multiple scattering

can even occur in the pyramidal nanostructures and light can be strongly trapped, leading to a largely reduced reflection. As a result, solar energy can be largely harvested through a highly enhanced photothermal conversion efficiency (PTCE). Heteroatom doping for broadband light absorption is a good approach to enhance the PTCE. As is shown in Figure 5-12e, highly B-doped Si shows a nearly perfect absorption in the full solar spectrum with an average absorption of about 98.7%. The total reflectance can be seen in Figure 5-10f, showing a reflectance of approximately 1%, which is much lower than the pristine Si sample. According to a previous work,[113] strong doping helps to improve the absorption of light with wavelength beyond the band edge (1110 nm), while lightly doped Si showed a large reflection when the solar light wavelength exceeds 1110 nm (Si's cutoff wavelength). Combined above results with the previous characterization, it indicates that doping and nanostructuring can be an effective approach to harvest more solar energy and further to obtain a high PTCE.[31,155] It is noted that the nearly full solar spectrum absorption performance of b-Si stands forward among the reported full solar spectrum absorption materials (see Table 5-2).[31,119,141,144,149,150]

Table 5-2 Absorption performance compared to recently reported photothermal conversion materials

Samples	Average absorptance	Absorption range	References
b-Si	**98.7%**	**300 – 2500 nm**	**This work**
3D Al nanoparticles	<90%	400 – 2500 nm	Ref.[31]
cotton-CuS aerogel	95.5%	290 – 1400 nm	Ref.[141]
PCC sponge	96%	250 – 2500 nm	Ref.[119]
GO-based aerogels	<90%	200 – 2500 nm	Ref.[144]
Te nanoparticles	~90%	200 – 2000 nm	Ref.[149]
3D graphene	97%	250 – 2500 nm	Ref.[150]

In a typical photothermal responsive experiment, a 2 × 2 cm^2 b-Si sample is used to explore the sample's surface temperature change under an intensity of 100 $mW \cdot cm^{-2}$

(AM 1.5 G). Figure 5-12f shows that the rising rate of b-Si surface temperature becomes slower and slower due to thermal equilibrium with the environment. It takes about 15 minutes to achieve 51.2 °C from room temperature (21.2 °C), while it lasts the same time to cool down to 22.2 °C again. It can be directly observed that the b-Si surface temperature changes by time according to Figure 5-12g. The real-time IR images indicate that the b-Si sample's temperature increases with illumination time. After t = 15 minutes, the b-Si sample reaches the highest temperature of 51.2 °C, which proves its good photothermal conversion capability. When switching off the lamp, the cooling to room temperature requires about 15 minutes, indicating the thermal conduction of the b-Si to the beaker and air.

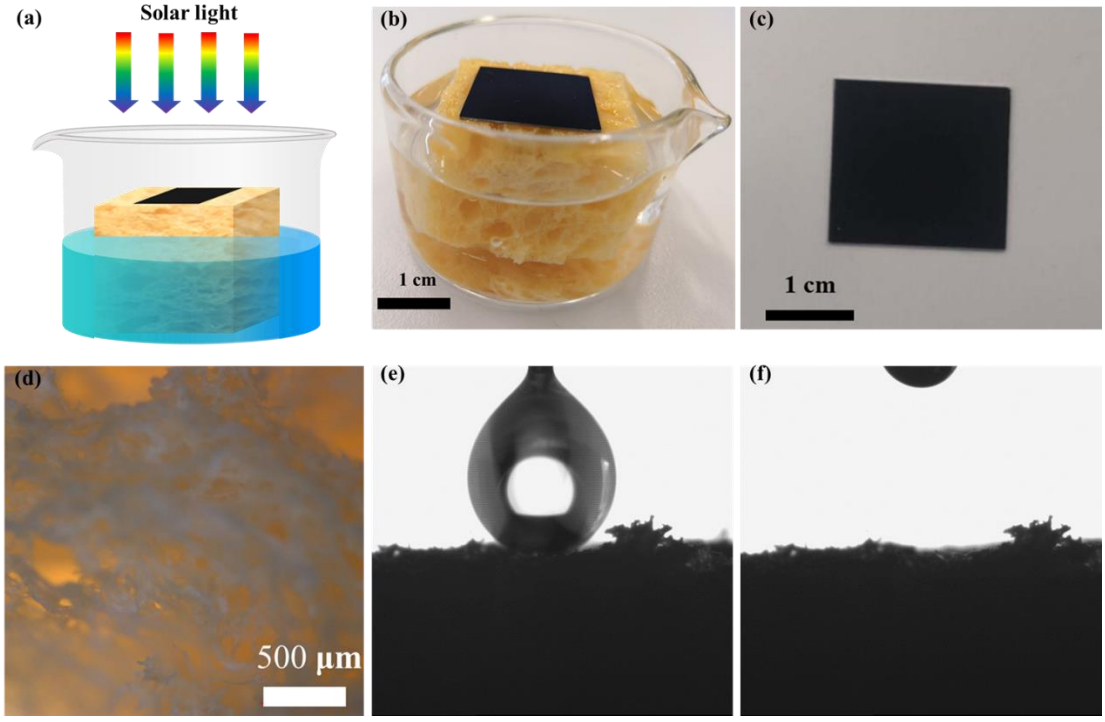

Figure 5-13 (a) Schematic picture of the photothermal water evaporation experimental set-up. (b) The photothermal water evaporation device, the b-Si sample is put on the center of the sponge's surface, and the sponge is placed in water with exposing about 20% of its body into the air. (c) Photo of 2×2 cm^2 b-Si sample, which is used as a solar absorber. (d) Optical microscope (OM) image of the porous sponge, which is acted as a water transportation channel, supporting material and also water vapor transportation channel. (e) and (f) Contact angle measurement before and after the test.

Figure 5-13a shows the schematic diagram of the photothermal water evaporation experimental set-up. As seen in Figure 5-13b, the b-Si with an area of 2 × 2 cm^2 was

directly placed on the center of water saturated sponge (3 × 3 cm^2). Figure 5-13c shows the photo of b-Si sample with a size of 20 × 20 mm^2. Under the solar light irradiation, the b-Si sample absorbs the solar energy and convert it to heat. The heat then is transferred to the sponge uptaking with water for the generation of water vapor.

The sponge has a multi-function: first of all, it is used as a water absorber, which can uptake enough liquid water for generating water vapor. Then, it functions as a supporting material for holding the b-Si sample. Last but not least, it also offers plenty of channels for transporting water vapor to the atmosphere. In Figure 5-13d, it is an optical microscope (OM) image of the multi-function sponge. In this scale, we can observe lots of microporous structures with pore size from dozens of micrometers to several hundred micrometers. In order to measure the wettability of the porous sponge, contact angle (CA) measurement has been conducted. As presented in Figure 5-13e and 13f, we capture the image of the droplet above the porous sponge before the droplet touches the sponge's surface. Upon the droplet reaches the sponge's surface, it is suddenly absorbed by the porous sponge and forms a nearly 0° contact angle. We also measure the SPS water uptake capability, Figure 5-14a and 5-14b show the weights of SPS before and after soaking saturated water. It indicates that a saturated sponge (16.052 g) can absorb water exceeding 20 times the weight of the dry sponge (0.768 g). This only causes a part of expansion (see Figure 5-14a and 5-14b). Thus, the evaporation occurs mainly from the sponge. But the effective evaporation cannot be expected in the area of sponge covered with black Si. However, vapor transport can be imagined through the channels of the porous structure into the uncovered area of the sponge. The effective evaporation area is considered as (3 × 3 - 2 × 2) cm^2. In addition, it is possible to design a container to collect condensed water from the evaporated water vapor.[31] Thus, it shows a great potential application for photothermal seawater desalination by only taking advantage of solar energy.

Figure 5-14 (a) and (b) Photographs showing the weights of superhydrophilic porous sponge before and after soaking saturated water.

The PTCE is evaluated by the water evaporation rate and the increased water temperature in an hour compared with the initial situation. Figure 5-15a shows the real-time temperature change of the whole photothermal device under an intensity of 100 $mW \cdot cm^{-2}$ (AM 1.5 G). At the beginning, the b-Si sample's surface shows an initial temperature of 22.5 °C. In the end, the b-Si sample's surface reaches 43.2 °C after one hour's illumination, which is 20.7 °C higher than the initial temperature. Due to thermal diffusion to the water and SPS, the b-Si sample's surface temperature with an hour's irradiation is even 8°C lower than that for the pure b-Si (Figure 5-12g). It verifies that b-Si not only has an excellent photothermal conversion ability, but also can transfer the heat to the water and the sponge and thus speed up the water evaporation process. It should be noted that only the b-Si sample gains the highest temperature surface while the temperature of the other part remains relatively low. This is probably caused by the strong electric field enhancement within the b-Si sample (see the FDTD simulation below). Figure 5-15b shows the b-Si's surface temperature change during the photothermal water evaporation under the irradiation. It shows a similar increase in the whole process compared to the bare b-Si.

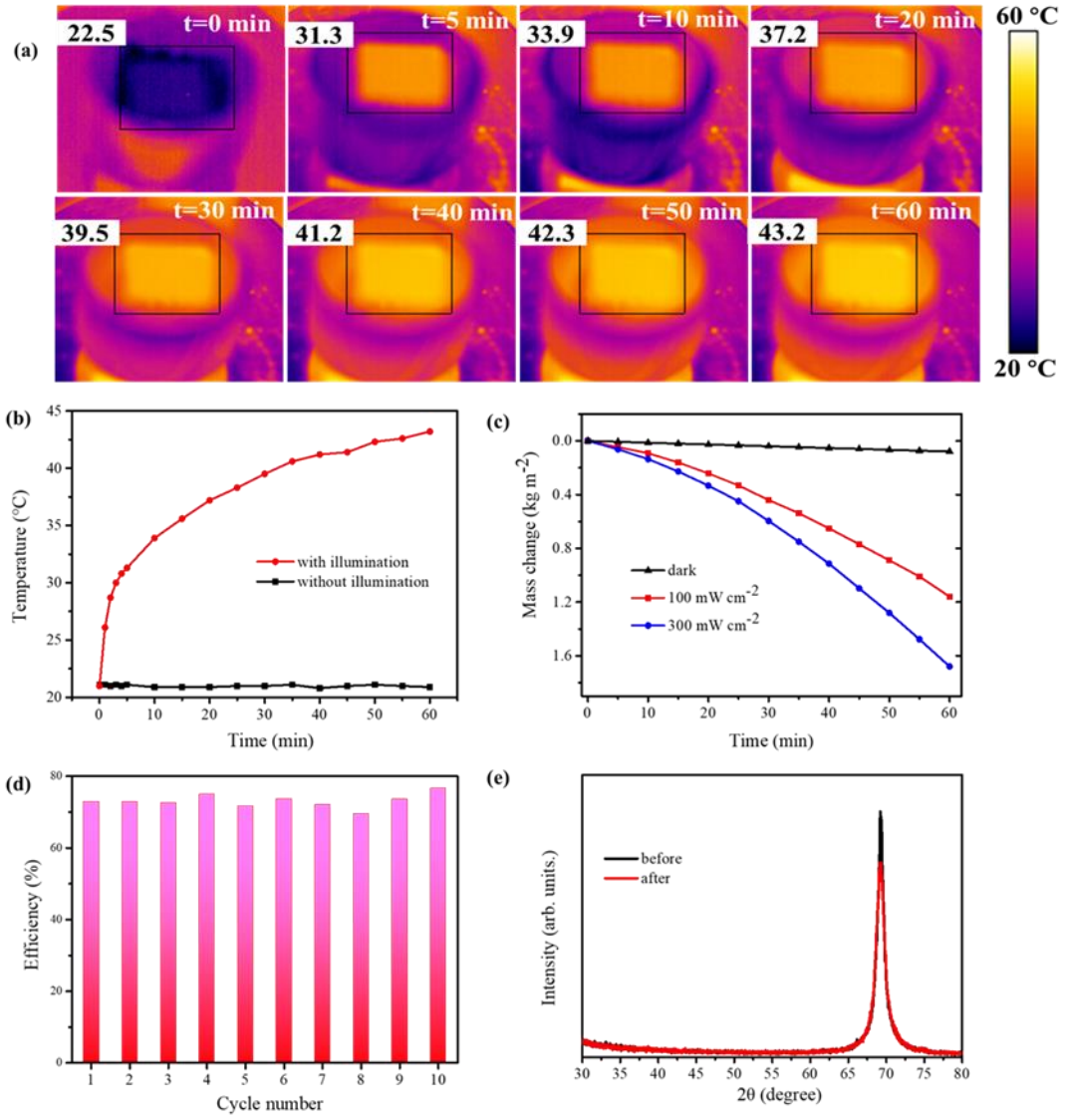

Figure 5-15 (a) Real-time IR images during the photothermal water evaporation, the number at the top left shows the maximum value of the temperature in the black rectangle. (b) Temperature changes against time with and without illumination. (c) Mass change of water evaporation with b-Si@SPS in the dark, 100 mW·cm^{-2} and 300 mW cm^{-2}. (d) b-Si@SPS sample cycle tests of PTCE under the solar illumination intensity of 100 mW cm^{-2}. (e) The XRD patterns before and after cycle tests. No changes appear in the patterns, showing the stable microstructure in b-Si.

In the water evaporation experiments, evaporation rate is used to calculate the efficiency. It defines as:[40,115,141,148]

$$\langle r \rangle = \frac{m_{\text{start}} - m_{\text{end}}}{S_{\text{effe}} \cdot t_{\text{illum}}} \tag{5-9}$$

Where r stands for the average evaporation rate in 1 hour, m_{start} and m_{end} for recording

the mass at t min, t +5 min. t_{illum} is 1 hour. S_{effe} are the effective area of SPS uncovered by b-Si (3 × 3 cm^2 - 2 × 2 cm^2), respectively. During the illumination, we record the mass of water evaporation by a balance, which is shown in Figure 4c. The evaporation rate of b-Si@SPS shows about 0.08 $kg \cdot m^{-2} \cdot h^{-1}$ in the dark. The evaporation from the b-Si@SPS combination under 100 mW cm^{-2} is much faster and can reach the evaporation rate to 1.16 $kg \cdot m^{-2} \cdot h^{-1}$, which is about 14.5 times than that in the dark. The evaporation rate is a constant in the observed time frame (in Figure 5-15c). We define the PTCE as:

$$\eta_{\mathrm{PTCE}} = \left[r \cdot \Delta H_{\mathrm{Eva}} + c_p \cdot r \cdot (T_2 - T_1)\right]/Q_{\mathrm{in}} \quad (5\text{-}10)$$

Where ΔH_{Eva} represents the evaporation enthalpy of water, here $\Delta H_{Eva} \approx 2.43 \times 10^3$ $J \cdot g^{-1}$ at 30 °C, c_p is the specific heat of water, T_1 and T_2 stand for the initial and final temperature of water and Q_{in} is input power of solar light on the b-Si sample. In this case, Q_{in} is calculated to be per 1 m^2 and for per 1 h irradiation, Q_{in} = 1 $kW \cdot h \cdot m^{-2}$ (3.6×10^6 $J \cdot m^{-2}$). Due to r ΔH_{Eva} >> *c r(T_2-T_1), c r(T_2-T_1)* can be neglected in the equation. Thus,

$$\eta_{\mathrm{PTCE}} = r\,\Delta H_{\mathrm{Eva}}/Q_{\mathrm{in}} \quad (5\text{-}11)$$

The results show that the η_{PTCE} of b-Si@SPS under AM 1.5G 100 $mW \cdot cm^{-2}$ irradiation can reach 73%. We think two essential factors should be responsible for such high PTCE: a) the b-Si has an extremely excellent light absorption structure so that nearly all the solar light can be absorbed to produce heat. b) SPS offer enough channels for water vapor transportation. The photothermal water evaporation experiment under a solar intensity of 300 mW cm^{-2} is also explored. Figure 5-15c also indicates an average evaporation rate of 1.68 $kg \cdot m^{-2} \cdot h^{-1}$, which is 1.45 times higher than that under 100 mW cm^{-2}. This could be a good path to improve the evaporation rate. However, it only gains a η_{PTCE} = 36.0%. We assume that high flux solar light can be rapidly absorbed by b-Si, but the heat can be dissipated into the air in a larger scale, leading to lower efficiency.

In order to explore the stability of the as-prepared b-Si@SPS, the cycle test, reflection and absorption properties, crystal structure and morphological characterization before and after photothermal water evaporation experiments have been conducted. As shown

in Figure 5-15d, the b-Si@SPS behaves with good stability after 10 cycle tests, and it keeps high PTCE (average 73.04%) during the 10 cycle tests. This could be an excellent advantage for water evaporation of the b-Si@SPS system. Figure 5-15e shows that the peaks of single crystalline Si (100) still stand at the position of 69.3° before and after cycle tests. There are no impurity peaks from the whole XRD patterns, which indicate that b-Si still keeps its monocrystalline after being tested for 10 times. Figure 5-16a and 5-16b show the SEM pictures before and after the cycle test. It indicates that the structure of b-Si has not been destroyed at all, and this is the reason why it can keep the reflection and absorption properties no decrease. In addition, the reflectance (Figure 5-16c) characterizations also verify it. There are almost no declines in both reflectance and absorptance performance after the b-Si@SPS sample is tested under a solar intensity of 100 $mW \cdot cm^{-2}$ for 10 times.

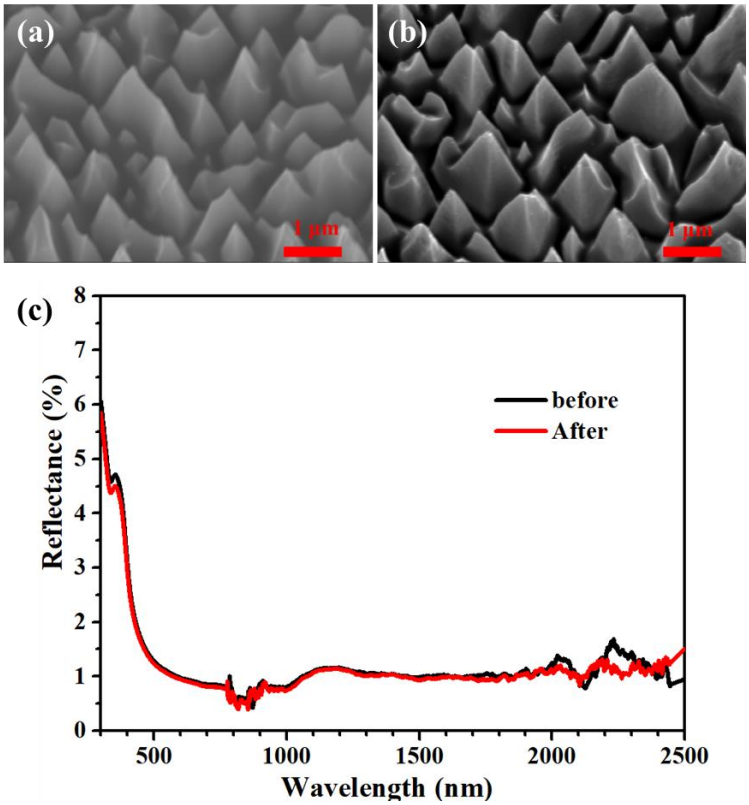

Figure 5-16 SEM images of b-Si before (a) and after (b) 10 cycles testing. The contrast differences are due to different types of detectors and different work distances. For the left, mixed detectors were used with a work distance of 8.3 mm. For the right, the upper detector was used with a work distance of 15.6 mm. (c) The reflectance shows almost no changes before and after cycle tests. Sample with 120 min etching time.

In order to better understand the interaction between the b-Si structure and light, we construct a simplified model with ordered nanostructure for the FDTD simulation, and the structure feature size is extracted from Figure 5-11. Figure 5-17a presents the FDTD simulation model of the b-Si structure. In this model, 25 tetrahedral-pyramids are uniformly distributed on the Si substrate. Figure 5-17b shows the reflectance results belong to a FDTD simulation result compared to the experimental measurement. The results agree well, indicating that our model can be used for investigating the interaction between the b-Si structure and light. For the b-Si material, the absorption ability of electromagnetic power can be used as a simple function to calculate:[149,156,157]

$$P_{abs} = \frac{1}{2}\,\omega \cdot \mathrm{Im}(\varepsilon_{Si}) \cdot |E|^2 \tag{5-12}$$

Where P_{abs} is the absorption ability, $|E|$ stands for the amplitude of the total electric field intensity inside b-Si and $|E|^2$ states for field enhancement, $\mathrm{Im}(\varepsilon_{Si})$ belongs to the imaginary part of permittivity and ω represents for the angular frequency. In this given b-Si sample, ω is the $2\pi c/\lambda$. Thus, $\mathrm{Im}(\varepsilon_{Si})$ and $|E|^2$ determine absorption ability together. The data of $\mathrm{Im}(\varepsilon_{Si})$ can be found in Ref.[149] There it is indicated that the value of $\mathrm{Im}(\varepsilon_{Si})$ sharply reduces from wavelength 300 nm to 500 nm and the wavelength larger than 500 nm keeps at a constant. This means that the b-Si absorption ability is only decided by field enhancement $|E|^2$ when the wavelength of incident light exceeds 500 nm. Figure 5-17c to 5-17f show the electric field enhancement (EFE) of a pyramidal nanostructure change from b-Si/vacuum interface to the inner b-Si under different light wavelengths. As shown in Figure 5-17c, the light at a wavelength of 300 nm interacts strongly with the interfaces of the b-Si, resulting in a relatively big reflection (see Figure 5-17b). As the wavelength increases (Figure 5-17d to 5-17f), the interaction gradually becomes weaker and weaker on the b-Si surface. However, the EFE within the b-Si tends to become stronger, which means the interaction between light and silicon is enhanced within the b-Si structures. According to Equation 5-12, the absorption should be improved compared with wavelength at 300 nm. In fact, it is in accordance with both the experimental measurement and simulated result. It is also clear that the EFE is around up to 5 times within the b-Si, confirming the strong light-trapping ability of the

structures.

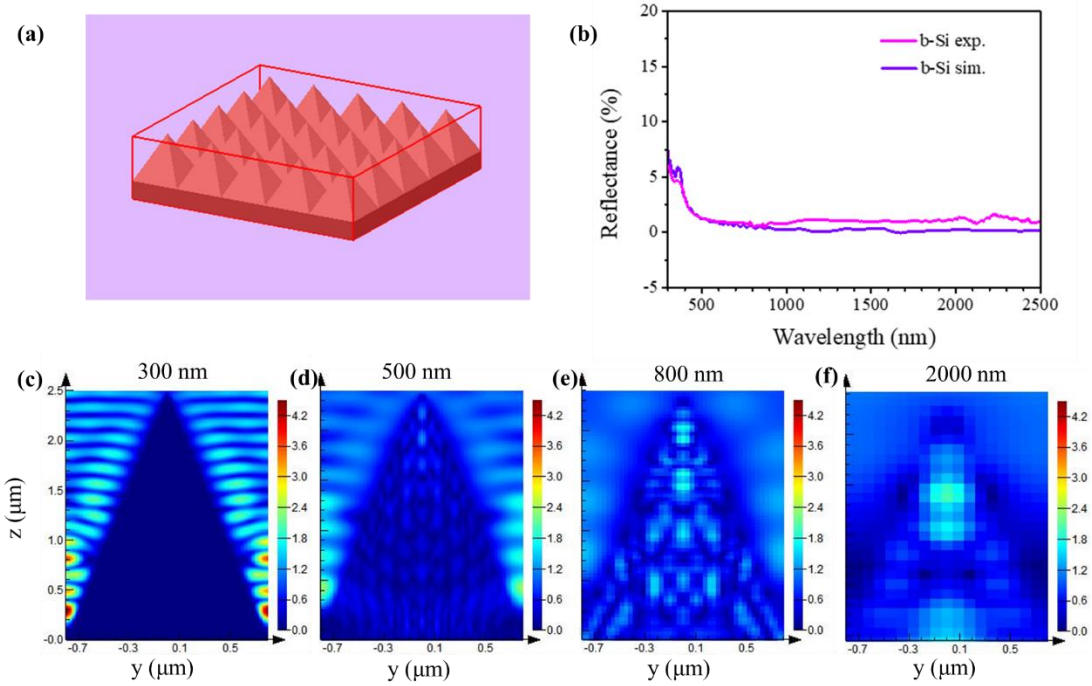

Figure 5-17 Nearly perfect absorption of the b-Si nanostructure. (a) FDTD simulation model of the b-Si structure. (b) Total reflectance of experimental and simulated b-Si. (c) ~ (f) Electric field enhancement of single pyramidal b-Si nanostructure at a broadband range from UV light (300 nm) to visible light (500 nm) to NIR light (800 nm) to middle IR light (2000 nm). The color scale is $|E|/|E_0|$.

5.2.3 Conclusions

In conclusion, we demonstrate that the ultra b-Si sample can be applied as an excellent light absorber for a photothermal water evaporation system. The ultra b-Si sample gains extremely high light absorption of about 98.7% across the full solar spectrum, due to the surface texturing and doping effects. Using the ultra b-Si sample connected with the superhydrophilic porous sponge, we can achieve an average PECE of 73% under 1 sun (AM 1.5G). The b-Si@SPS photothermal converter has an advanced PTCE compared with the latest reported photothermal conversion materials. It also presents good stability during 10 cycle tests, which indicates a great potentially practical application. Furthermore, FDTD simulations are conducted to get a better understanding of the reflection results and the mechanism of how the electric field enhancement affects the light absorption. The reported non-toxic, highly efficient, cost-efficiently and broadband-solar-spectrum absorptive b-Si photothermal material is expected to provide

wide promising applications such as water purification, photothermal therapy as well as photo-thermoelectric conversion.

5.3 Results of b-Ag plasmonic structures for photo-thermoelectric conversion

5.3.1 Introduction of photo-thermoelectric conversion using b-Ag

Photo-thermoelectric (P-TE) power generation is a sustainable energy technology for converting solar energy to electric power, which can be one efficient technology for green energy production.[158–162] Basically, a photo-thermoelectric power generation device consists of two components: the light absorber and the thermoelectric modules.[33,158,160] The former is applied to trap the solar light and then transform it to heat while the latter converts the heat into electric power. A feasible strategy to improve the performance of the P-TE device is to search for an ideal light absorber for the whole solar spectrum absorption, i.e. a material that absorbs all the solar light without transmission and reflection.[163] The absorbed solar energy from the absorber is basically transformed into photoinduced carriers (electrons and holes) or heat, leading to many aspects of applications, such as photovoltaic solar cells,[164] photochemical reactions,[163] surface enhanced Raman spectroscopy (SERS)[165] and solar vapor generation.[31,166] Therefore, fabricating a novel and ideal absorber may promote the development of these fields.

To date, different methods have been reported to fabricate an ideal metal-based absorber, such as anodized aluminum oxide (AAO) combined with physical vapor deposition (PVD)[40] or electrochemical deposition (ECD),[155] reactive ion etching (RIE),[167] colloidal lithography (CL) followed by atomic layer deposition (ALD).[168] However, there are still many restrictions in the reported works, which largely block their large-scale applications. For example, PVD or ECD-based absorbers can be scalable in production but the size of AAO template restricts its large area fabrication. the etching conditions of RIE-based absorbers are quite harsh during the fabrication process. CL-based absorbers seem not to have the mentioned problems, but the fabrication is more expensive than the others.

In this chapter, we report the application of a novel hybrid material which is a perfect full-solar-spectrum absorber. It can be fabricated by a simple, controllable, low-cost and scalable metastable-atomic layer deposition (MS-ALD) method. The perfect silver

plasmonic absorber is able to absorb over 99% of the incident light at the wavelength range from 200 nm to 2500 nm, which almost fully covers the full solar spectrum.[78] Randomly distributed silver nanoparticles loaded on the tree-shaped silica nanostructures can produce strong collective effects of localized surface plasmon resonance (LSPR) among them. The LSPR-induced electric field enhancement and multiple scatterings are thought to cause the strong light absorption. The b-Ag plasmonic nanostructures can also be easily deposited on the most solid substrates at large scale, making it easy to realize broader applications. By using this silver plasmonic light absorber, we can convert solar energy to heat under ambient conditions. Additionally, we attached a photo-thermoelectric converter that can successfully convert solar energy to electric power with an experimental maximum power of ~ 2.5 mW under 100 mW cm^{-2} solar intensity. By connecting 20 converters in series on a sunny day (solar intensity is about 80 mW cm^{-2}), they can produce a voltage as large as 2.261 V, indicating its potential application for solar-to-electricity conversion.

5.3.2 Results and discussion

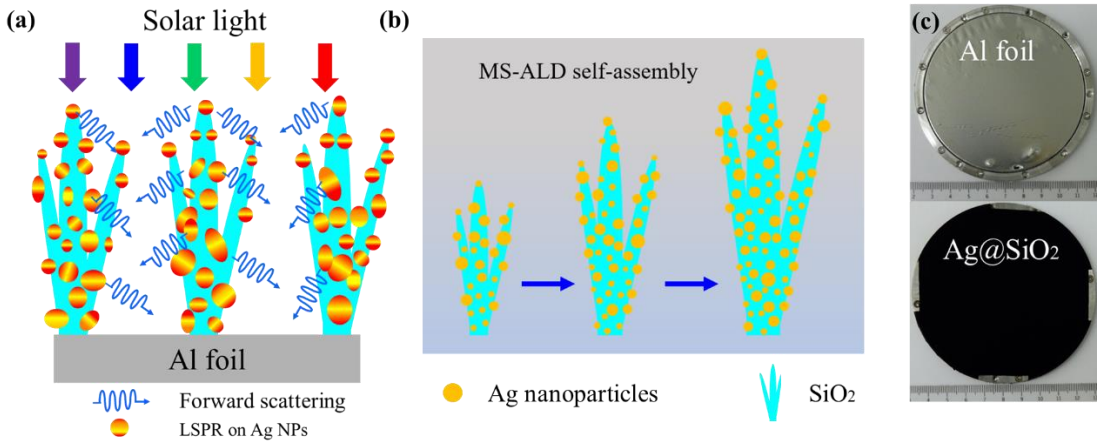

Figure 5-18 Schematic picture, fabrication process and photograph of b-Ag plasmonic absorber. (a) The light-matter interaction principle of an ideal plasmonic absorber. (b) self-assembly of silver nanoparticles on the SiO_2 nanowires to obtain the silver plasmonic absorber in ALD chamber. (c) Photos of 4-inch wafer scale bare Al foil and high plasmonic Ag@SiO_2 nanostructure.

As illustrated in Figure 5-18a, our silver-based plasmonic nanostructure has two crucial

features: dense 3D SiO_2 nanostructure as the support and silver nanoparticles with random sizes (average size is about 20 nm) attach on SiO_2 nanostructure. The high SiO_2 nanostructure can enable multiple forward scatterings and reduce reflection into the air (Figure 5-18b).[33,40,169] The Ag nanoparticles with random sizes are able to produce strong hybridized localized surface plasmon resonance (LSPR) under the illuminated light, leading to the strong absorption from ultraviolet light (200 nm) to mid-Infrared light (2500 nm) regions.[31,40,78,170]

The b-Ag plasmonic nanostructure can be prepared by a scalable and simple process: 300 nm silver film deposited on the 4-inch aluminum (Al) foil by PVD method, then transfer it into the ALD chamber for SiO_2 deposition. Different from conventional ALD process, here 3D SiO_2 nanostructures can be evolved in a self-assembly manner due to the presence of silver (cyclic formation of metastable silver oxides and their decomposition) and thus the method is called metastable ALD (MS-ALD) (see experimental section for details).[78] By repeating the above process (Figure 5-18b), the height of the plasmonic structure can be adjusted (Ag@SiO_2-H for the high structure, Ag@SiO_2-M for the middle structure, Ag@SiO_2-L for the low structure). In Figure 5-18c, it is easily distinguishable that the bare 4-inch Al foil becomes totally matte black after the MS-ALD process, and this is a direct observation of the broadband and highly efficient light trapping of the silver-based plasmonic nanostructure.

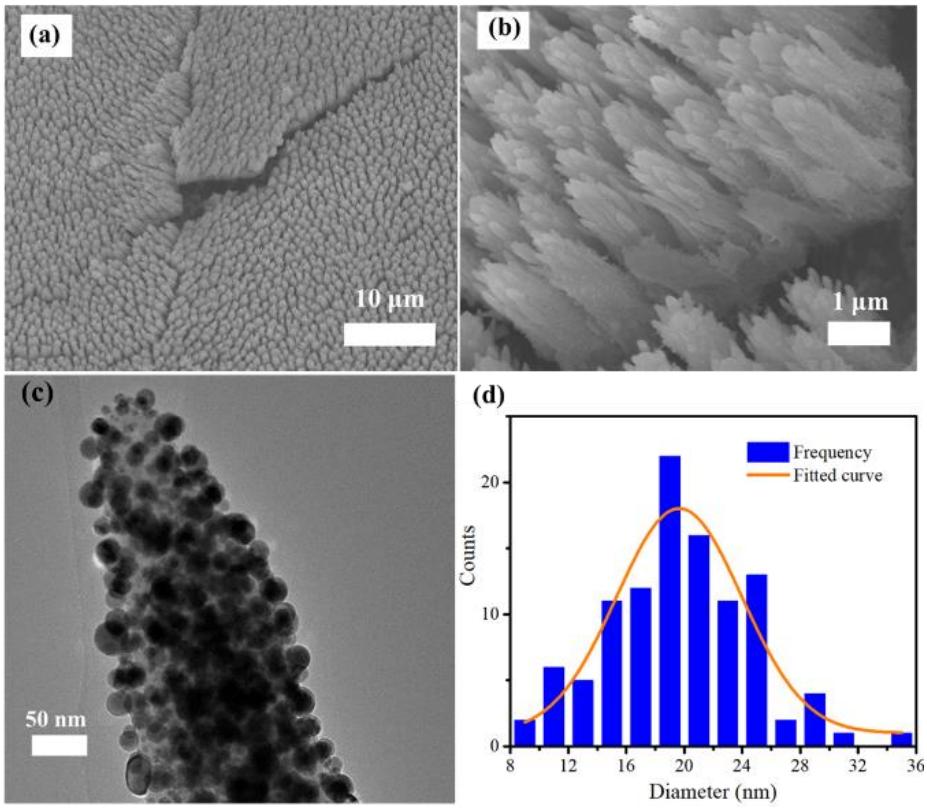

Figure 5-19 Structural characterizations of the silver-based plasmonic absorber. (a) Low magnification and (b) high magnification scanning electron microscopy (SEM) image (tilt angle of 20°) of a typical Ag@SiO_2-H sample. (c) Typical transmission electron microscopy (TEM) image of Ag@SiO_2 sample. (d) Statistical Ag nanoparticle size distribution derived from Figure 5-19c.

As is discussed above, the structural height of the as-prepared silver-based plasmonic nanostructure has an important influence on the light absorption performance. To explore the surface morphology of our plasmonic absorber, SEM characterizations are conducted. Figure 5-19a shows the typical SEM image of the high structured silver-based plasmonic absorber. It can be seen that the sample surface has hierarchical nanostructures and the nanostructures vertically stand on the substrate. It can be further seen in Figure 5-19b, that the branch-shaped SiO_2 with several hundreds of nanometers attaches on the SiO_2 nano-trees. These hierarchical nanostructures favor multiple forward scattering. TEM investigation is used to determine the sizes and distributions of the silver nanoparticles, which is the most critical factor for the strong LSPR effect and further lead to ultra-broadband light harvesting.[78] In Figure 5-19c, a high number of silver nanoparticles adhere on the hierarchical SiO_2 nanostructures. Among the silver

nanoparticles, each of them occurs at a distance of several nanometers to several dozens of nanometers to other silver nanoparticles. This arrangement allows for numerous hybrid plasmonic resonant modes. The statistical result (Figure 5-19d) show that the average size of the silver nanoparticles is around 20 nm and all the nanoparticles are smaller than 50 nm, leading to strong light-matter interaction at frequencies near their plasmon frequency with respect to these sizes.[170] As a result, multiple light scattering effectively couples with the LSPR effect of these nanoparticles, leading to strong plasmonic absorption improvement in ultra-broadband light.[40] By repeating physical vapor deposition (PVD) and atomic layer deposition (ALD), the height of the absorber can be further increased. More SEM images are shown in Figure 5-20a ~ 20f, in which silver nanoparticles with several dozens of nanometers are still hard to be observed. However, the x-ray diffraction (XRD) experiments can easily prove the existence of crystalline silver in the XRD patterns (Figure 5-20g).

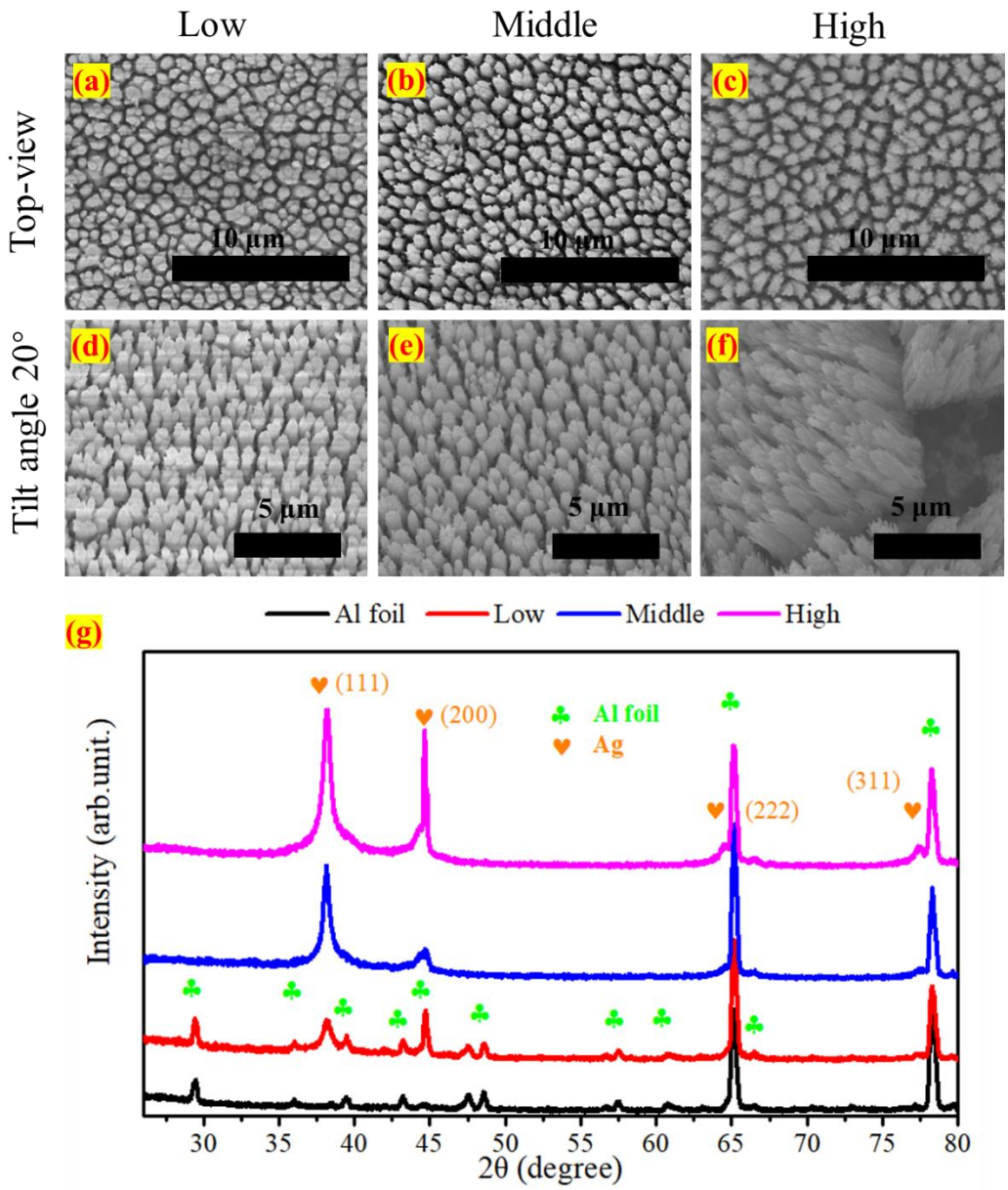

Figure 5-20 (a)~(c) Top-view SEM pictures of Ag@SiO_2-L, Ag@SiO_2-M, Ag@SiO_2-H. (d)~(f) Side-view SEM pictures (a tilt angle of 20°) of Ag@SiO_2-L, Ag@SiO_2-M, Ag@SiO_2-H. (g) XRD patterns of Al foil, Ag@SiO_2-L, Ag@SiO_2-M, Ag@SiO_2-H.

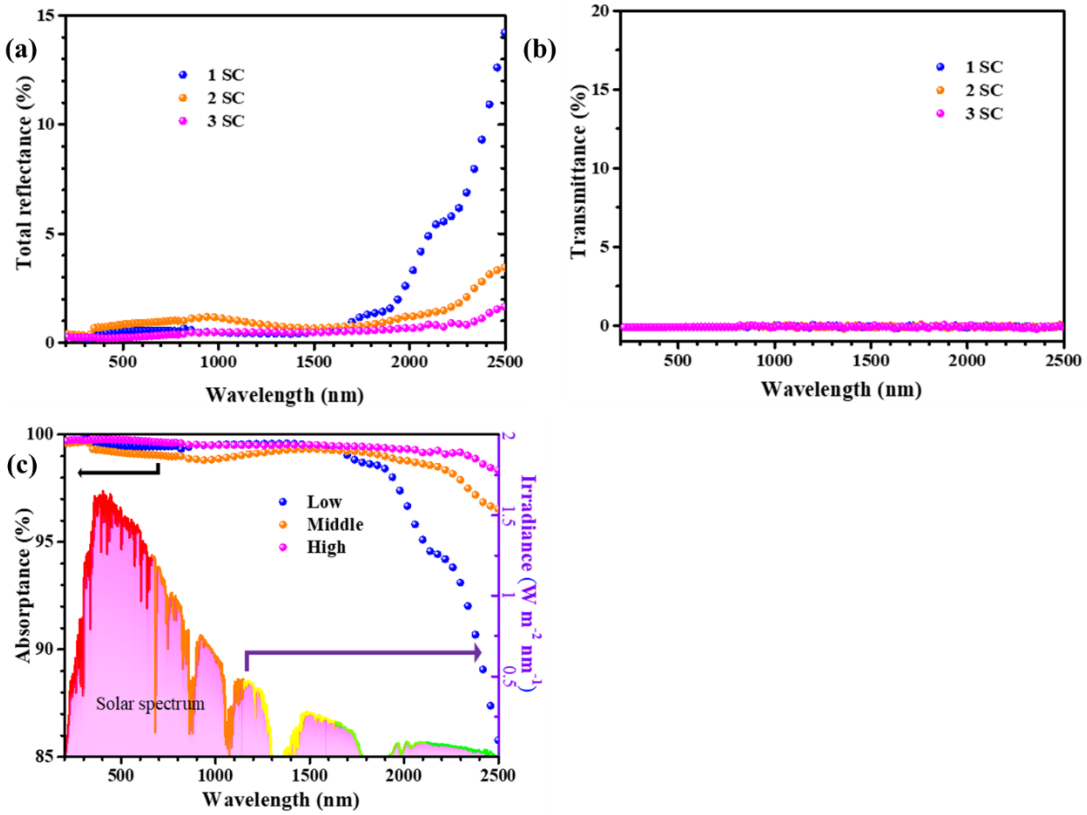

Figure 5-21 Full-solar-spectrum absorption of silver nanoparticles. (a)~(c) Experimental reflection, transmission and absorption property of different Ag@SiO_2 plasmonic nanostructures. The solar spectrum in (c) is the standard AM 1.5G solar spectrum.

In order to quantitatively analyze the absorption property of the as-prepared silver-based plasmonic absorbers, the UV-Vis-NIR absorption spectra of the above mentioned three samples have been measured in the wavelength range from 200 nm to 2500 nm, where the material absorbs more than 98% energy of the whole solar spectrum. It is noted that the absorptance is calculated by the following Equation:

$$A = 100\% - R - T \qquad (5\text{-}13)$$

where A is absorptance, R is reflectance and T is transmittance. The measurement details can be found in the experimental section. The average total reflectance (Figure 5-21a) decreases from 2.2%, 1.2% to 0.6% for the Ag@SiO_2-L, Ag@SiO_2-M and Ag@SiO_2-H structures, respectively. The measured transmittance (Figure 5-21b) is approximated to zero. As presented in Figure 5-21c, the calculated average absorptances for different samples are above 97% for the incident wavelengths from

200 nm to 2500 nm. It is interesting that the Ag@SiO_2-H sample shows the average absorptance as high as 99.4% and the absorptance exceeds 99% in the wavelengths below 2340 nm.

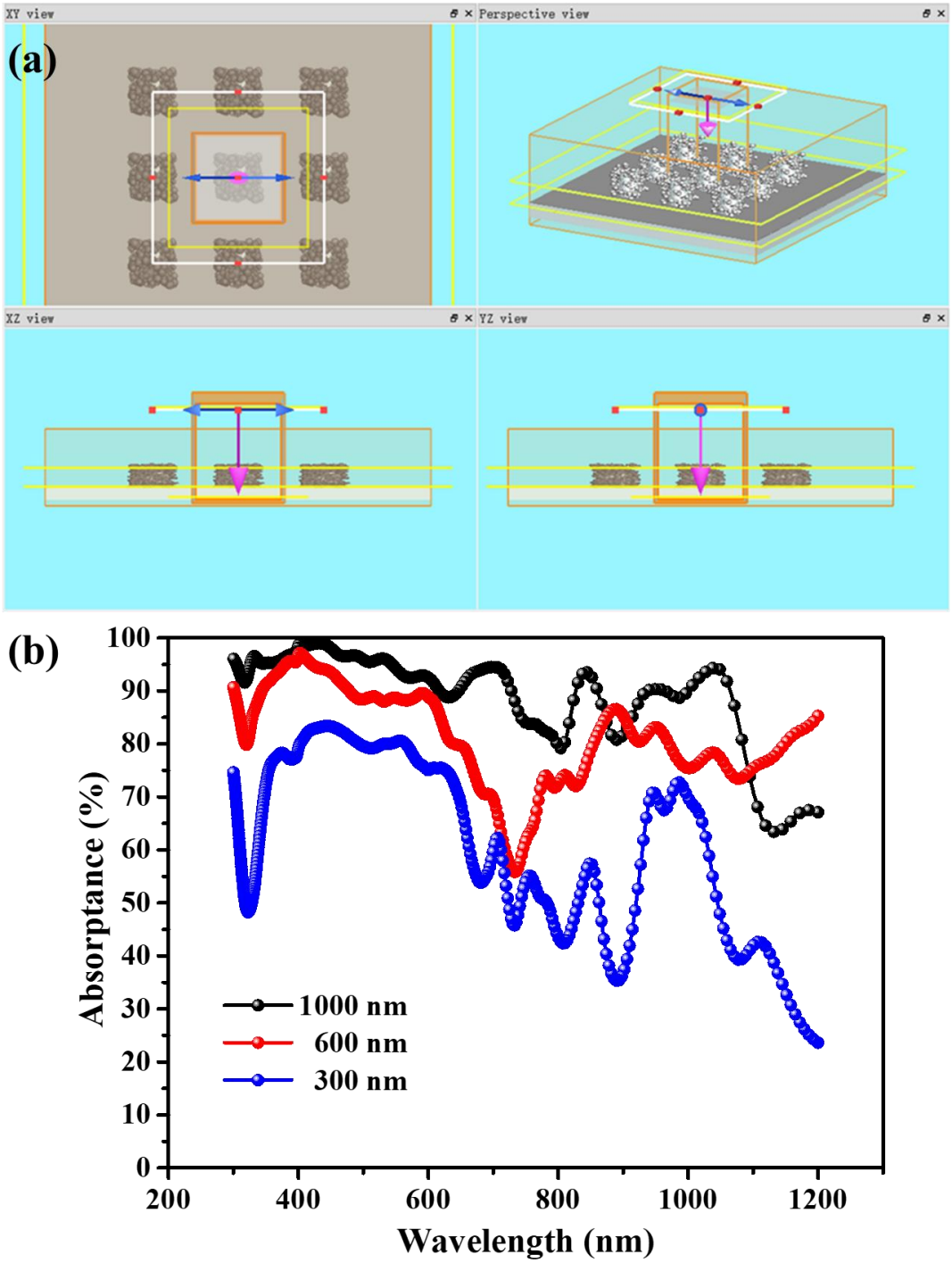

Figure 5-22 (a) Simulated absorption model constructed by FDTD software. Ag@SiO_2 nanostructure with random Ag nanoparticles on 300, 600, 1000 nm SiO_2. The loaded amount of Ag nanoparticles increases with structural height. All the simulated parameters, such as periodicity, nanoparticle density, substrate, light source, are kept

the same, except the height. (b) Simulated absorption spectra of Ag@SiO_2 nanostructures with different heights of 300, 600, 1000 nm.

The mechanism of the broadband absorption of the 3D hierarchical nanostructure is very complicated and related to several aspects, such as multiple forwards scattering in the 3D nanostructures, collective effect of plasmonic absorption and collective effect of hybrid plasmons for Ag particles with small spacing. 3D Finite Differences Time Domain (FDTD) simulations are conducted to indicated their improved broadband absorption. Due to the limited computation power, we cannot simulate the collective effects through the whole 3D complex structure, but here a simple model with nanostructure array has been constructed (Figure 5-22a). The structure heights with 300, 600 and 1000 nm are presented and the corresponding density of loaded Ag nanoparticles is kept the same. The simulated results (Figure 5-22b) show that the height of 3D nanostructure can remarkably influence the absorption, and a higher 3D structure has a higher broadband absorption. It is clear that stronger multiple scattering and stronger collective effect of plasmonic absorption can be expected in the higher structure with larger amount of loaded Ag nanoparticles, which has also been verified by previous work. [33,42,78]

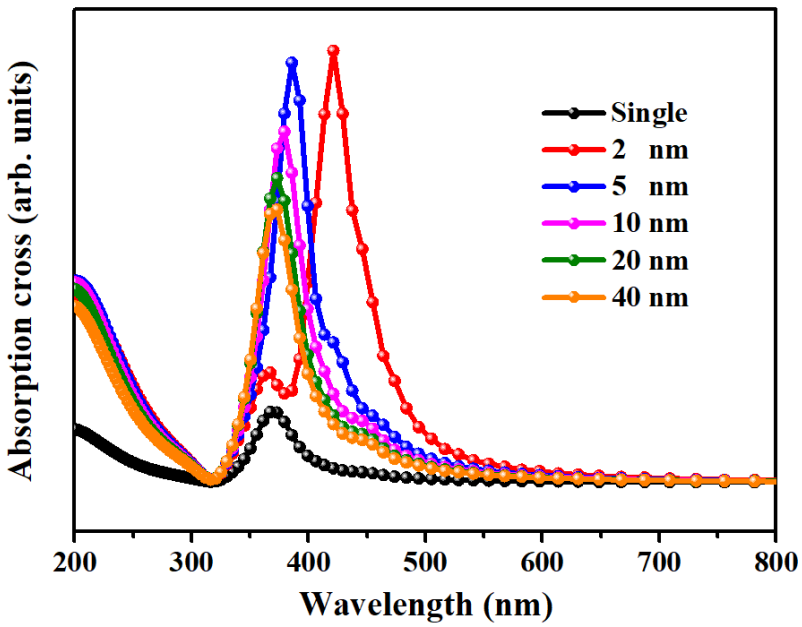

Figure 5-23 FDTD simulated absorption cross with different gap distances between dimers.

As observed in Figure 5-23, the particle spacing is very close, and here it is also interesting to know if there is collective contribution from the hybrid plasmons effect to the excellent broadband absorption. Here the plasmonic properties of the dimer (two Ag nanoparticles of 20 nm diameter) with varied spacing from 2 nm to 40 nm has been simulated. For comparison, the property of an isolated single Ag nanoparticle has also been simulated. Figure 5-23 shows the absorption properties (intensity and peak) of the dimers are clearly dependent on the spacing, and larger absorption can be achieved with smaller spacing such as 2 and 5 nm. This means there is a clear contribution from the collective hybrid plasmons effect to the excellent broadband absorption.

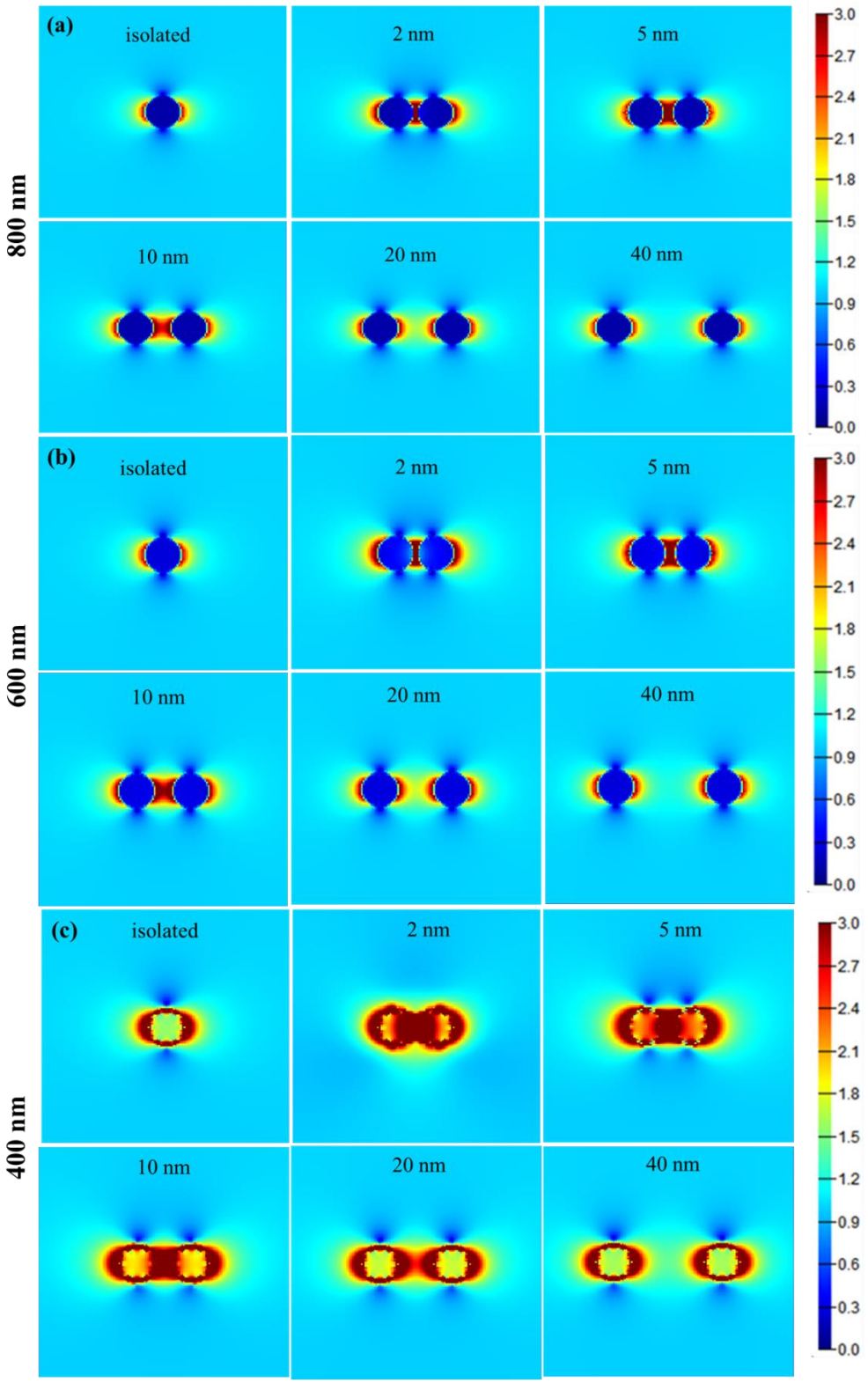

Figure 5-24 Light-matter interaction property of silver nanoparticles. (a)~(c) two Ag nanoparticles with a distance of 2 nm, 5 nm, 10 nm, 20 nm and 40 nm. Ag nanoparticles with a typical size of 20 nm. Incident wavelength is 800, 600, 400 nm, respectively. The color scale is $|E|/|E_0|$.

To further explore the dependence of the hybrid plasmons effect on the spacing of the dimer, electric near field enhancement simulations are conducted. Figure 5-24a~24c show the light-matter interaction for the isolated Ag nanosphere, dimers with a spacing of 2 nm, 5 nm, 10 nm, 20 nm and 40 nm. By analyzing the electric field enhancement induced by the incident light with wavelength of 800 nm, it is obvious that the strong LSPR effect (Figure 5-24a) is produced when the incident light illuminates on the single Ag nanosphere, while clearly stronger field enhancement can be found in the gap region of the dimers especially with spacing of 2 and 5 nm. Moreover, when two shorter incident wavelengths (600 nm and 400 nm) are applied, similar effects are observed, but the interactions are stronger as the incident wavelengths are smaller (Figure 5-24b and 24c).

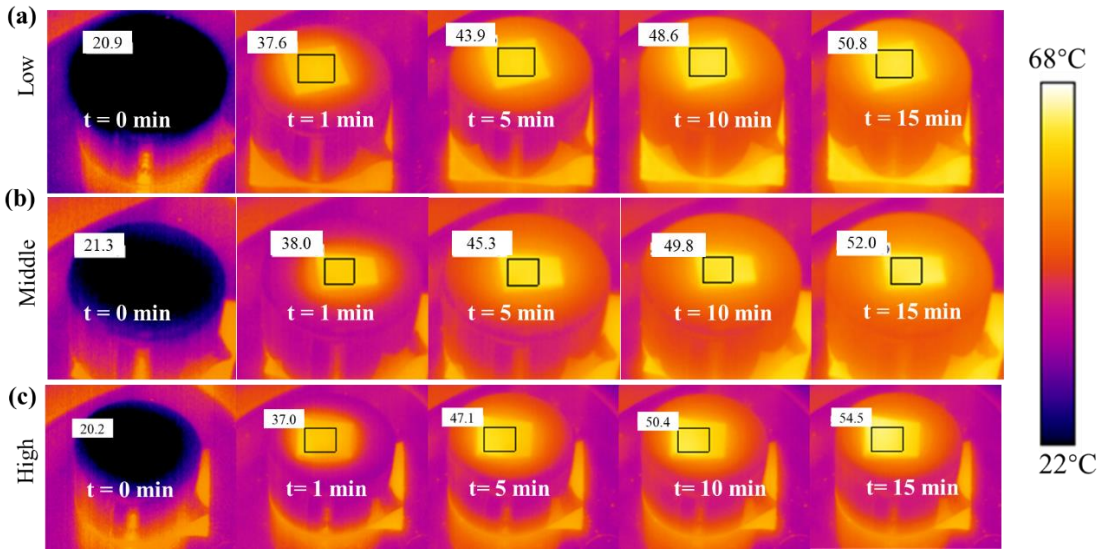

Figure 5-25 Photothermal properties vs. time images of b-Ag plasmonic nanostructures with different heights (a)~(c). The number at top left is temperature in °C.

Light absorbers are capable of harvesting the incident solar light at a broad range of wavelengths to generate heat or electron-hole pairs for the application of solar cells,[171] artificial photosynthesis,[172] photothermal therapy[173,174] and photo-thermoelectric power generation.[33,119,158,175,176] In our study, all three silver-based plasmonic absorbers show excellent light absorption (average absorption is above 97%), thus, the photo-induced heat production causes similar results under the same conditions (Figure 5-25a ~ 25c). As shown in Figure 5-25a, the sample surface average temperature for Ag@SiO_2-H

increases from the initial 20.2 °C to the final 54.5 °C in 15 minutes, resulting a temperature difference of 38.5 °C. Accordingly, the sample surface average temperature for Ag@SiO_2-M and Ag@SiO_2-L has increased by 29.9 °C (Figure 5-25b) and 30.7 °C (Figure 5-25c), respectively. These results demonstrate that our prepared silver-based plasmonic absorbers possess a highly efficient solar to heat conversion ability.

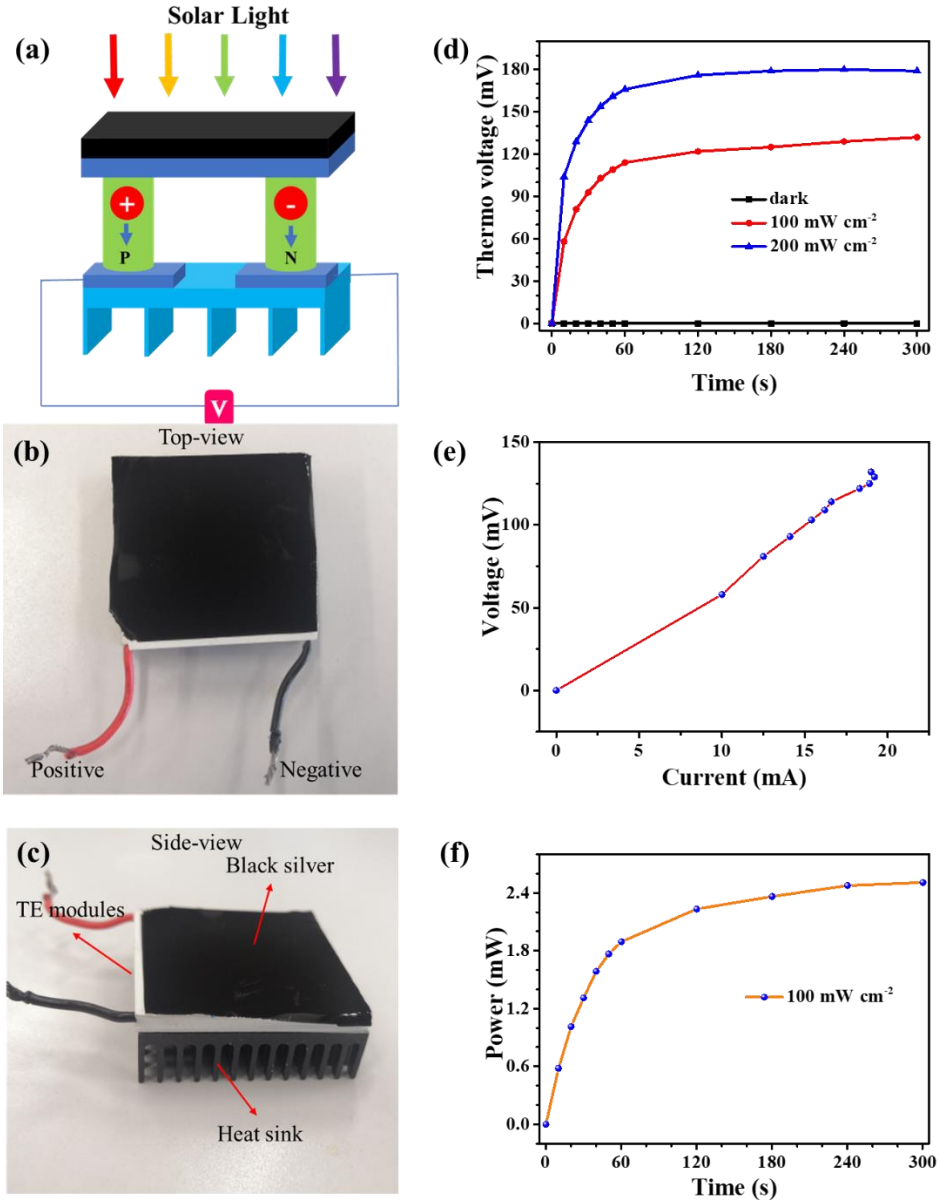

Figure 5-26 Photo-thermoelectric power generation experiments. (a) Schematic presentation of the photothermal-electric power generation process. (b) Top-view and (c) side-view of assembled photo-thermoelectric convertor with 4×4 cm^2 area. (d) Simultaneous electric power generation after being illuminated the light on the photothermal-electric conversion device. (e) I-V curve and of photo-thermoelectric convertor. (f) Power generation after being illuminated the light on the photothermal-electric conversion device.

Due to the excellent photothermal property of the Ag@SiO_2-H, we choose it for further photo-thermoelectric application. In this experiment, we present the photo-thermoelectric power generation process using the b-Ag as an absorber, a commercial thermoelectric module (TEC1-12706, Robotlink) as the heat-to-electric power generator and the simulated AM 1.5G solar light as the light source. Figure 5-26a shows a schematic picture of the photo-thermoelectric device. From the top to the bottom, they are silver-based light absorber, Al_2O_3 packaging materials, p-type and n-type (PN) thermoelectric materials, conductor and heat sink, respectively. Figure 5-26b and 26c show the well-assembled photo-thermoelectric convertor. From the beginning, we measure the performance of the single convertor under the dark condition, almost no open-circuit voltage can be detected in 5 minutes (in Figure 5-26d). However, upon light illumination the measured open-circuit voltage rapidly increases from none to 114 mV in one minute, corresponding to a voltage density of 71.25 Vm^{-2}. Later, the open-circuit voltage steadily increases to 132 mV (equals a voltage density of 82.5 Vm^{-2}) in 5 minutes. Its power rate can be calculated to about 2.53 mW (Figure 5-26e and 26f) under 1 sun. This result shows comparable performance with the reported works (Table 5-3). Such a power rate demonstrates its appealing application prospect.[177,178] To continue enlarge the power of the incident light, the voltage density further increases to 111.88 Vm^{-2}. This enables an improved voltage density while the solar light is concentrated onto the absorber. In order to verify its stability, the convertor is exposed under the light (AM 1.5G) and the dark conditions repeatedly for 40 times. The performance (Figure 5-27a) does not show any obviously decline, verifying that it can be reused many times when it is exposed in the dark and under the Sun repeatedly. We also test its optical properties after cycle tests and after being exposed in the air for 6 months, the absorptance and reflectance also do not show any decrease (Figure 5-27b).

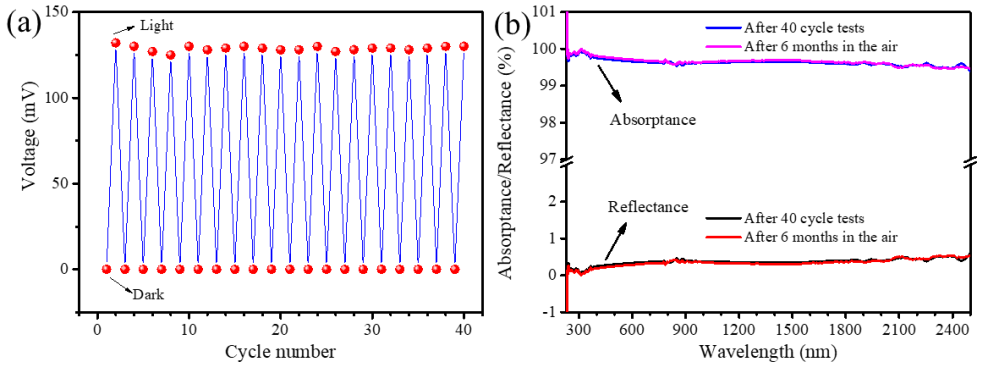

Figure 5-27 Stability test. (a) Stability test for the photothermal-electric conversion device. (b) Reflectance and absorptance spectra of the Ag@SiO_2-H samples after 40 cycles testing and after being placed 6 months in air.

Table 5- 3 The performance comparison of open circuit voltage with the reported works.

Material	Open circuit voltage	short circuit current	conditions	Ref.
b-Si	27.1 mV	1.6 mA	71 mW cm^{-2}	Ref.[102]
b-Si	64 mV	\	100 mW cm^{-2}	Ref.[33]
b-Si@Au	140 mV	\	100 mW cm^{-2}	Ref.[71]
b-Si@Au	16 mV	\	72.8 mW cm^{-2}	Ref.[179]
Ag@SiO_2	114 mV	19 mA	100 mW cm^{-2}	Cheng at al.

For the purpose of demonstrating the practical application of as-prepared silver-based plasmonic absorbers, we have assembled 20 photo-thermoelectric convertors in series (Figure 5-28a) and apply them to convert solar energy into electric power. Firstly, these convertors are placed outdoor for electric power generation at the solar intensity of ~80 mW cm^{-2}(Ilmenau, Germany, June 19, 2021). As presented in Figure 5-28b, the tandem convertors can achieve a maximum value of 2.261 V (70.66 V m^{-2}) in about two minutes, which indicates our prepared plasmonic absorbers show potential application for scalable electric power collection.

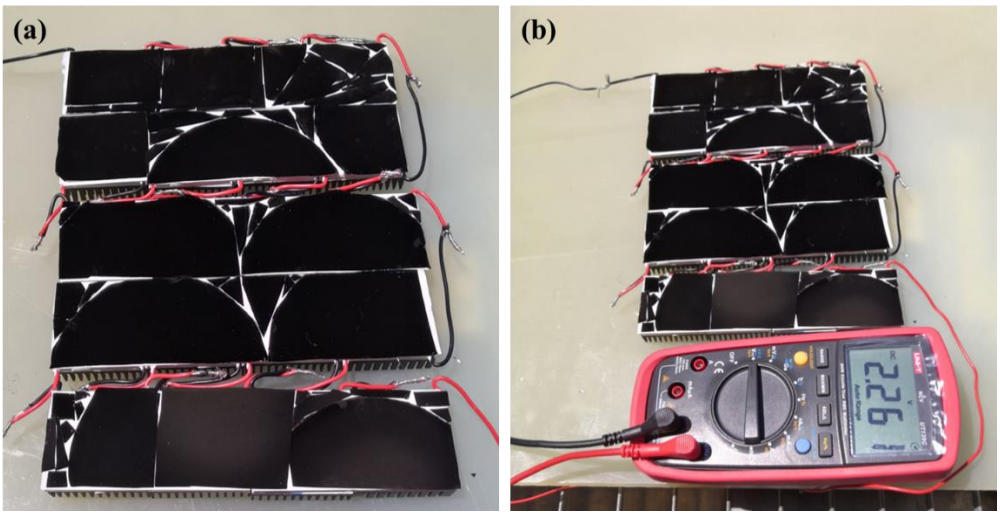

Figure 5-28 Large-scale device (a) 20 photo-thermoelectric convertors are connected in series. (b) A recorded maximum value of photo-thermoelectric voltage in outdoor experiment.

5.3.3 Conclusion

In summary, we have presented a b-Ag plasmonic absorber, which can harvest the incident light for wavelengths from 200 nm to 2500 nm and have an average absorptance of 99.4% in the whole solar spectrum. The b-Ag plasmonic absorber can be prepared by a scalable MS-ALD technique in a self-assemble manner. As-prepared b-Ag plasmonic absorber has plenty of uniformly distributed and hierarchical SiO_2 micro/nanostructures as support, where a large amount of random silver nanoparticles are attached. Their sizes range from several nanometers to dozens of nanometers. It is demonstrated that the strong LSPR hybridization of the adjacent silver nanoparticles and multiple scatterings lead to full solar spectrum absorption. The free-mask self-assembled fabrication method can also be applied to different solid substrates, enabling wide applications of solar energy harvesting. Moreover, the superior b-Ag with extremely high light absorption can be used for photo-thermoelectric power generation under the solar light irradiation. The voltage density (power rate) of assembled photo-thermoelectric convertor can achieve ~82.5 Vm^{-2} (2.53 mW) under 1 sun intensity (100 $mWcm^{-2}$). Furthermore, we also test the tandem devices with 20 convertors at outdoor, the results also show good photo-thermoelectric conversion ability. The described b-

Ag plasmonic absorber offers new possibilities for modern energy conversion technology, such as photochemical transformation, photothermal water evaporation, photo-thermoelectric power generation.

5.4 Results of b-Ag plasmonic structures for photothermal water evaporation

5.4.1 Introduction of photothermal water evaporation using b-Ag

Plasmonic metallic nanostructures using Au, Ag, Cu, or Al exhibit surface plasmon resonance (SPR) phenomena by strongly interacting with resonant photons, when the incident photon frequency is equal to the plasmon frequency.[31,180–182] Localized field enhancement around a plasmonic nanostructure can cause "hot spots" and also uncommon optical properties, enabling many applications in SPR sensing and detection,[183,184] catalytic conversion,[60,180,185–193] photothermal conversion,[194–200] personal thermal management,[201,202] photothermal therapy,[203] photovoltaic cells,[204] optical coatings.[205–208] However, although plasmonic nanostructured materials have such attractive prospects, there are still quite challenging problems that need to be solved. For example, almost no significant progress has been made on large area fabrication of plasmonic nanostructures (see Table 5-4),[31,180,198–200,206,207,209–212] which primarily hinders their technical applications. Thus, realizing large-scale fabrication, here more than 150 cm^2, will facilitate their real applications in the above-mentioned fields. As one of the typical plasmonic metallic nanostructures, Ag nanostructures tend to show SPR in the UV-Visible light region due to their limited permittivity,[180,191,193,205] resulting in no apparent resonance response in the infrared (IR) range. In addition, increasing the absorption range from UV-Vis to near-infrared will broaden the field of applications toward photothermal energy conversion techniques. Thus, removing these two obstacles would have a great significance towards more efficient solar energy conversion and other practical applications.

In order to address these two challenges, we put forward one strategy to fabricate the nanostructures on large scale and further improve the optical resonance response of Ag nanoparticles in the IR range. First, two kinds of large-scale fabrication methods of physical vapor deposition (PVD) and MS-ALD are applied. Second, the extinction effect induced by 3D Ag@SiO_2 nanostructures is introduced to absorb the light broadbandly.[31,189,199]

Nature offers many inspirations on structural and functional materials design, such as

the lotus effect for superhydrophobic coating, flying birds for airplanes, colorful butterfly for photonic crystal-based structural color design and so on. Inspired by the surface structure of coral tentacles (Figure5-29a), we apply a MS-ALD self-assembly method to prepare random size Ag nanoparticles (acting as "stinging cells") on the 3D hierarchically ordered SiO_2 branches and their SiO_2 body (acting as "coral tentacles"). Using this approach, we fabricate a large area of 153 cm^2 3D Ag@SiO_2 hybrid plasmonic nanostructures. By controlling the height and the Ag@SiO_2 size of the 3D nanostructure, they show adjustable reflection, transmission, and absorption properties within a broad bandwidth at the same time. We achieve an average reflection and absorption of 0.5% and 96.4%, respectively, for samples prepared with three supercycles (SC), which stand forward in the ultra-broadband reflection and absorption range from 200 to 2500 nm. FDTD simulation results indicate that the excellent optical extinction can be ascribed to the large-scale collective overlap of both the SPR effect of 3D distributed Ag nanoparticles and the Ag nanoparticles hybridization effect. Furthermore, we use the 3 SC Ag@SiO_2 plasmonic nanostructure sample as the bottom-heated water evaporation light absorber. It is demonstrated that it can significantly improve the evaporation rate to about seven times under 1 sun than in dark conditions.

5.4.2 Results and discussion

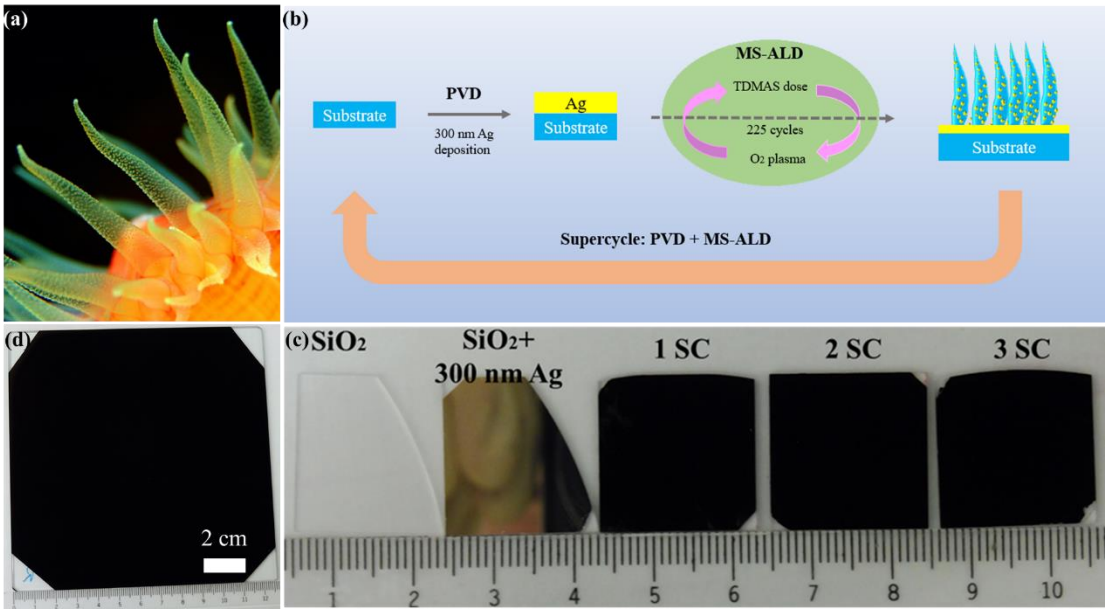

Figure 5-29 (a) Photo of coral tentacles. (b) Schematic picture of fabricating self-

assembly 3D Ag@SiO_2 plasmonic nanostructures with different supercycles. (c) photos of SiO_2 substrate, 300 nm Ag film on SiO_2 substrate, 1 SC, 2 SC and 3 SC self-assembled 3D Ag@SiO_2 plasmonic nanostructures. (d) 153 cm^2 1 SC self-assembled 3D Ag@SiO_2 plasmonic nanostructures. 1 supercycle = 1 SC.

We take advantage of a hierarchical nanostructure design strategy to fabricate 3D Ag@SiO_2 plasmonic nanostructure based on an MS-ALD self-assembly method. In order to precisely control the morphology of Ag@SiO_2 hybrid structures and to further regulate the plasmonic property, many years of efforts have been devoted to realizing controllable and large-scale production.[78,79,213] As depicted in Figure 5-29b, each optimized SC fabrication process of 3D Ag@SiO_2 plasmonic nanostructures includes two steps: At first, 300 nm Ag film is deposited on the SiO_2 substrate using thermal evaporation; then, MS-ALD is conducted for the evolution of 3D hierarchical SiO_2 structures loaded with Ag nanoparticles. The MS-ALD is developed based on the plasma-enhanced ALD process for the deposition of SiO_2 in the presence of Ag thin film. For the deposition of SiO_2, both tri(dimethylamino)silane (TDMAS) as Si^{4+} source and O_2 plasma as O^{2-} source are used as precursors. However, Ag can be oxidized during each O_2 plasma step (6 s) and then the metastable silver oxides can decompose and release oxygen during each TDMAS step (50 ms). The released oxygen can lead to a side reaction for the excess formation of SiO_2. Therefore, after 225 cycles, 3D hierarchical SiO_2 structures are evolved in a self-assembled way, and the Ag film is totally transformed into Ag nanoparticles loaded on the SiO_2 nanostructures during the cyclic oxidation of Ag and decomposition of its oxides. So each SC procedure consists of the deposition of 300 nm thick Ag film and the subsequent 225 cycles of MS-ALD. For the fabrication of 2 SCs and 3 SCs samples, the same procedure was just repeated 2 and 3 times (See Figure 5-29b). For 2 SCs sample, 2 × 300 nm thick Ag film was totally transformed into Ag nanoparticles and for the 3 SCs sample, 2 × 300 nm thick Ag films were totally transformed into Ag nanoparticles.

Figure 5-29c shows photos of the transparent SiO_2 substrate, the mirror-like Ag film

deposited on a SiO_2 substrate, 1 SC, 2 SC and 3 SC Ag@SiO_2 samples with extreme black surfaces. Most reported plasmonic nanostructures with self-assembly approaches, including metals and their compounds, have a limited scale not over 5 cm^2 (Table 5-4), which largely restricts their practical application in SPR sensing and detection, solar energy conversion, photothermal cancer therapy, and so on.[180,184,186,191,203,205,214] Here 3D Ag@SiO_2 hierarchically plasmonic nanostructures with a super large area of 153 cm^2 (Figure 5-29d) are fabricated in this work. Please note that this size is only limited by the used setups but not by the process itself. This breakthrough might show a significant influence in above-mentioned fields.

Table 5-4 Large scale and spectra adjustability comparison with the reported works and methods.

Samples	Methods [a]	Area	Spectra Adjustability	References
3D Ag@SiO2	MS-ALD+PVD	153 cm^2	**yes**	**This work**
Al nanostructures	MLDW+LN	1 cm^2	no	Ref.[182]
Al@AAM	AAM+ EBE	5 cm^2	no	Ref.[31]
Ni SPhCs	AAM+ECD	5 cm^2	yes	Ref.[198]
Cu@Zn-foil	DD	3 cm^2	no	Ref.[200]
PI NC/Au-W	CL+ICP+MS	~5 cm^2	yes	Ref.[206]
Au nanofilm	SG+TE	~	yes	Ref.[207]
Au nanostructure	HL +EBE+RIE	<4 cm^2	no	Ref.[209]
Pt, Pd & Ag	CL	< 2 cm^2	yes	Ref.[210]
Au, Ag and Al	NIL+EBE	2.6 cm^2	yes	Ref.[211]
Au/Cr nanostructures	CL+TE	1 cm^2	no	Ref.[212]
3D Au@AAM	AAM+PVD	5 cm^2	yes	Ref.[215]

[a] PVD: physical vapor deposition; MLDW: millisecond-laser-direct-writing; LN: liquid nitrogen; AAM: anodized aluminum membrane; EBE: electron beam evaporation; ECD: electrochemical deposition; DD: Dip-and-Dry fabrication; ICP: ion coupled plasma; MS: magnetron sputtering; SG: seeded growth; TE: thermal evaporation; HL: holographic lithography; RIE: reactive ion etching; CL: colloidal lithography; NIL: nanoimprint lithography.

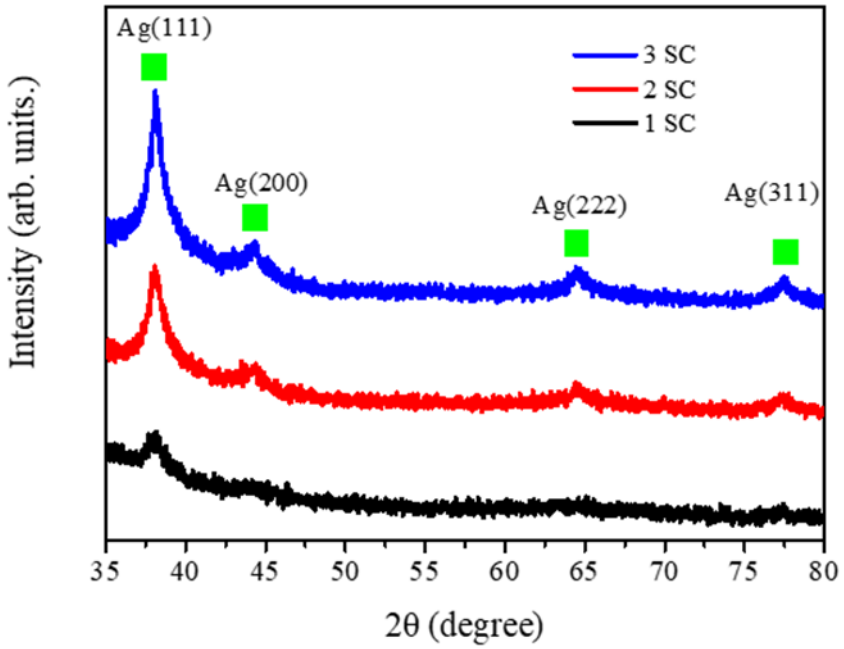

Figure 5-30 XRD patterns of 1 SC, 2 SC and 3 SC self-assembly Ag@SiO_2 nanostructures.

X-ray diffraction (XRD) measurements are conducted to determine the crystal structure of Ag@SiO_2 plasmonic nanostructures. The four peaks in the XRD pattern in Figure 5-30 can be assigned to Ag (111) at 38.1°, Ag (200) at 44.3°, Ag (222) at 64.5° and Ag(311) at 77.5°, which perfectly corresponds to PDF#89-3722 and also ref[216]. Combining this and the previous result, the Ag@SiO_2 plasmonic nanostructures only consist of crystalline Ag and amorphous SiO_2.[78,216] Also seen in Figure 5-30, as the number of super cycle increases, the intensity of Ag (111) peak tends to become larger, indicating that a higher grade of crystallinity for Ag nanoparticles is achieved or the particles are larger.

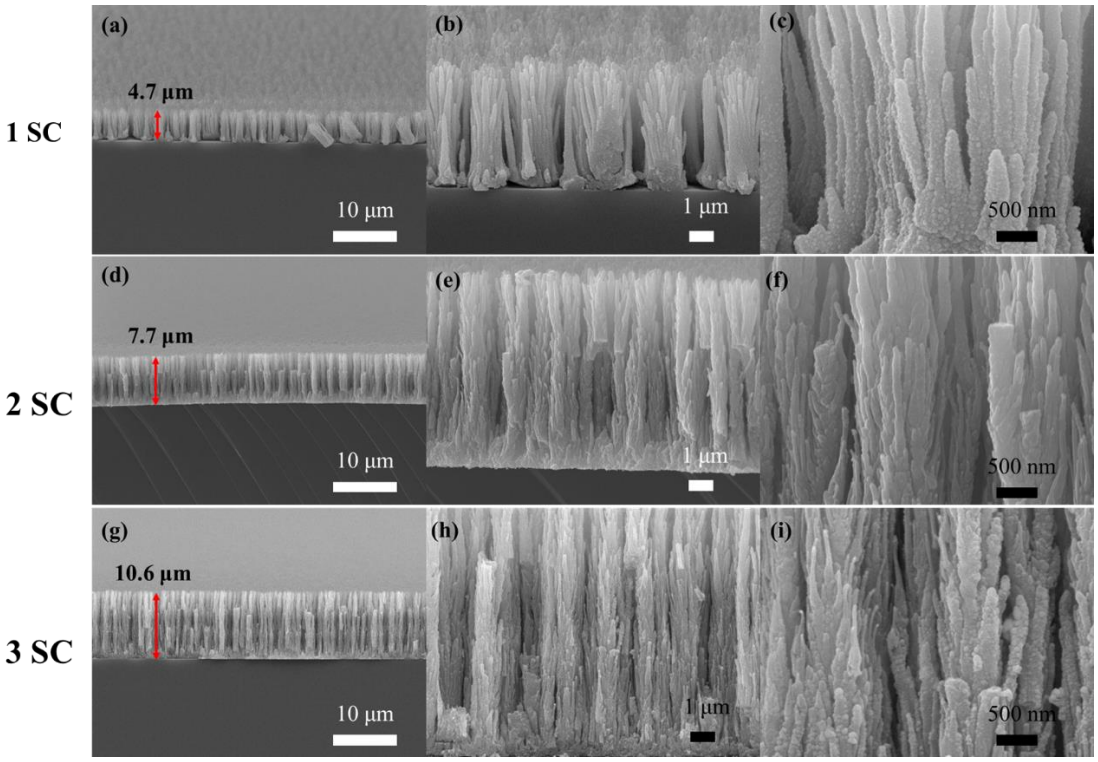

Figure 5-31 Morphology characterizations of silver plasmonic nanostructures. (a)~(i) Scanning electron microscopy (SEM) images of the cross-section at different magnifications for 1, 2 and 3 SC Ag@SiO_2 samples, respectively.

Structural analysis and film height were determined using SEM characterizations. As shown in Figure 5-31a, the average height of 1 SC Ag@SiO_2 hybrid plasmonic nanostructures is about 4.7 µm and the height is almost uniform. Hierarchical branches appear on each SiO_2 trunk (Figure 5-31b). At high magnification (Figure 5-31c), plenty of Ag nanoparticles with a random size distribution can be found adhering on the SiO_2 trunk and its branches, in accordance with surface structures on coral tentacles (Figure 5-29a). For the 2 SC samples, the average height of the Ag@SiO_2 plasmonic nanostructures rises to 7.7 µm (Figure 5-31d). Longer and thinner hierarchical branches of the Ag@SiO_2 plasmonic nanostructures can be observed in Figure 5-31e and 31f compared to the 1 SC sample. The highest and thinnest Ag@SiO_2 plasmonic nanostructures are achieved for the 3 SC samples. As presented in Figure 5-31g ~ 31i, the height of the 3 SC sample is 10.6 µm, while the width of the hierarchical branches is the smallest. Figure 5-32 shows the top-view of these samples. The densities of

$Ag@SiO_2$ plasmonic nanostructures are getting larger among the different samples, while the sizes of corresponding hierarchical branches are becoming smaller, which is consistent with SEM characterizations of the cross-section.

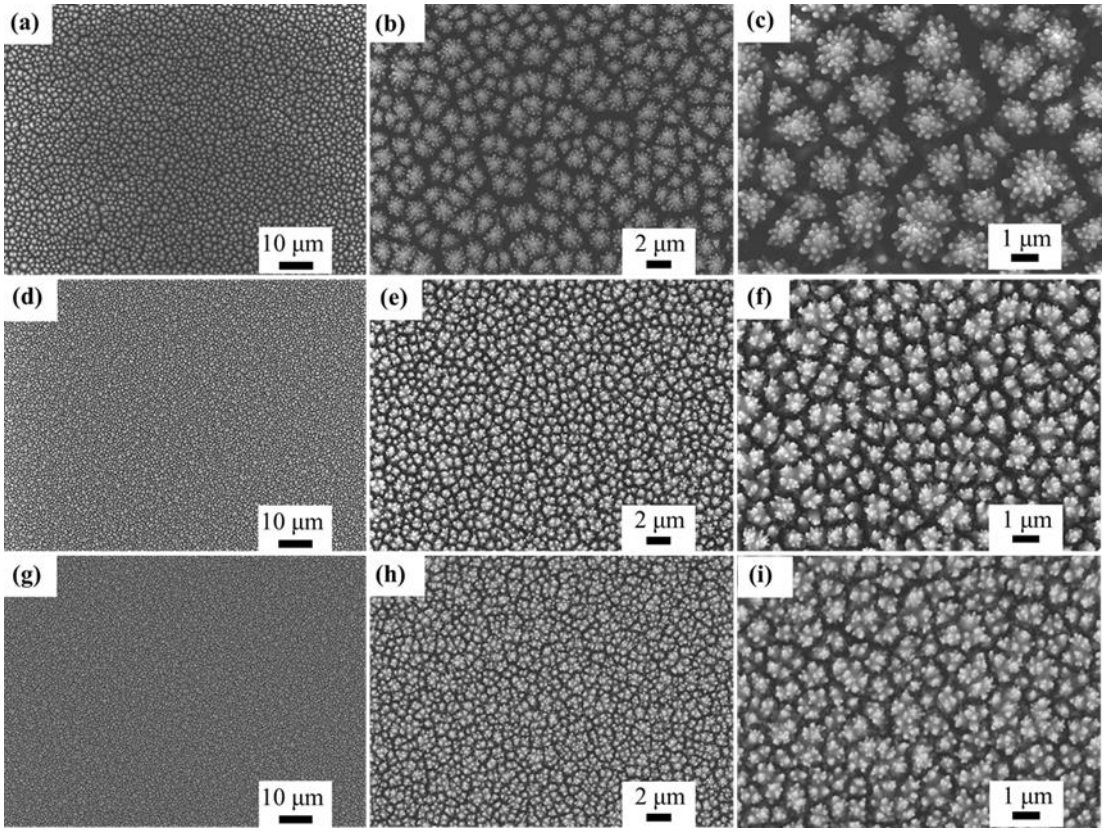

Figure 5-32 a~c, d~f and g~i different magnifications top-view SEM images of 1, 2 and 3 SC of $Ag@SiO_2$ samples, respectively.

The typical 3 SC $Ag@SiO_2$ sample is scratched from the substrate and transferred to copper TEM grids with lacey carbon films for TEM analysis. Figure 5-33a shows one of the $Ag@SiO_2$ nanostructures lying on the TEM grid. Obviously, there are plenty of Ag nanoparticles attached to the SiO_2. HRTEM image in Figure 5-33b shows the random size distribution of Ag nanoparticles. The corresponding particle analysis result in Figure 5-33c indicates that the typical size distribution mostly ranges from ca. 10 nm to several dozens of nanometers. Figure 5-33d presents the atomically resolved HRTEM image of a single crystal Ag nanoparticle partially stacking on another Ag nanoparticle. Therefore, two sets of reflection spots can be observed in the Fast-Fourier-

transformed (FFT) pattern (Figure 5-33e). Atomically resolved STEM-EELS element mapping of a Ag particle (Figure 5-33f ~ 5-33i) shows that the Ag_2O oxide layer with the thickness of few nanometers appears on the surface of the Ag particle. We think that such thin oxide layer is due to the exposure to air for about 5 months from their fabrication to TEM analysis.

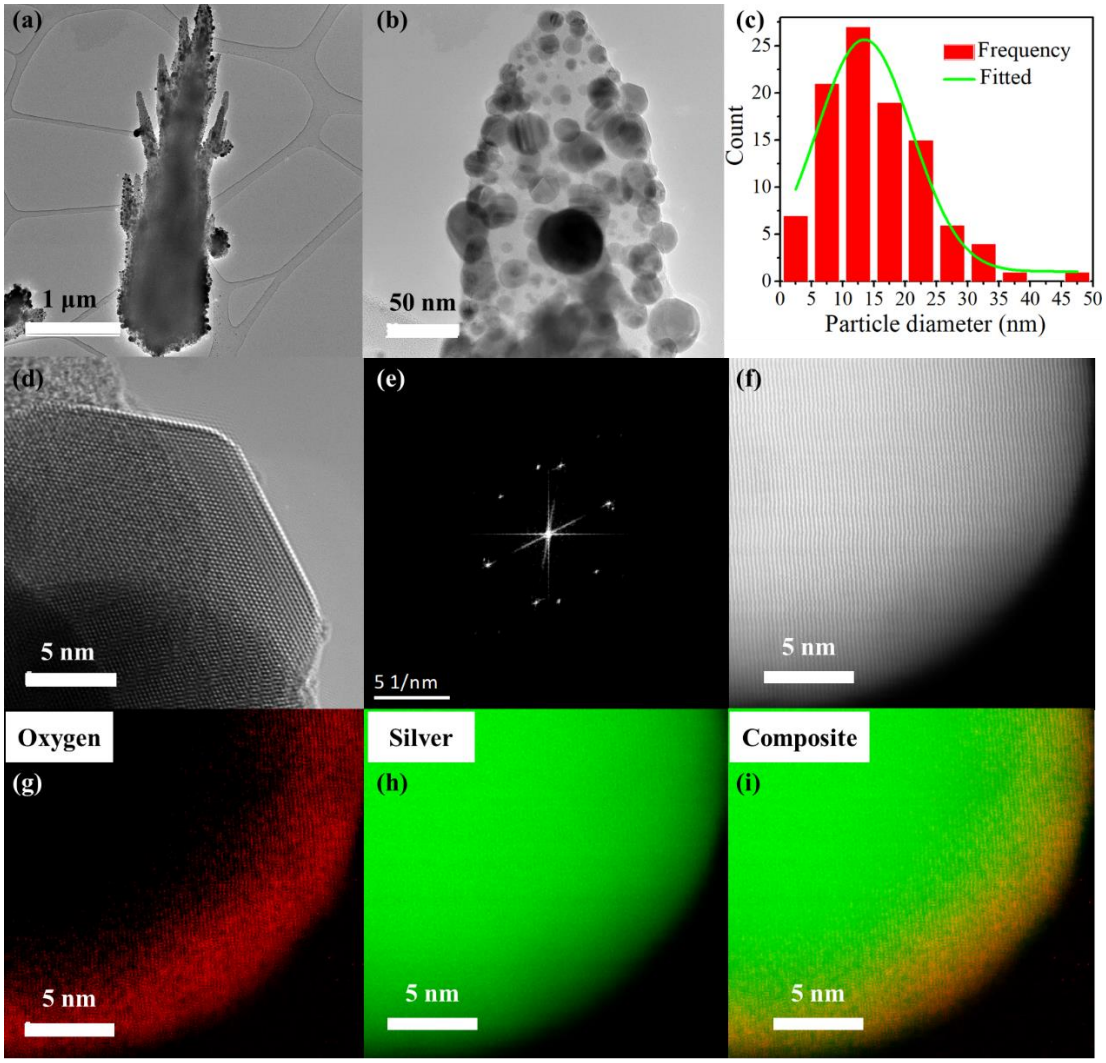

Figure 5-33 (a), (b) and (d) Aberration-corrected high-resolution TEM (HRTEM) images of $Ag@SiO_2$ nanostructures for the 3 SC sample at different magnifications. (e) The corresponding FFT pattern in d. (c) Statistical Ag nanoparticle distribution for (b). (f)~(i) Atomically resolved element mapping with STEM-EELS.

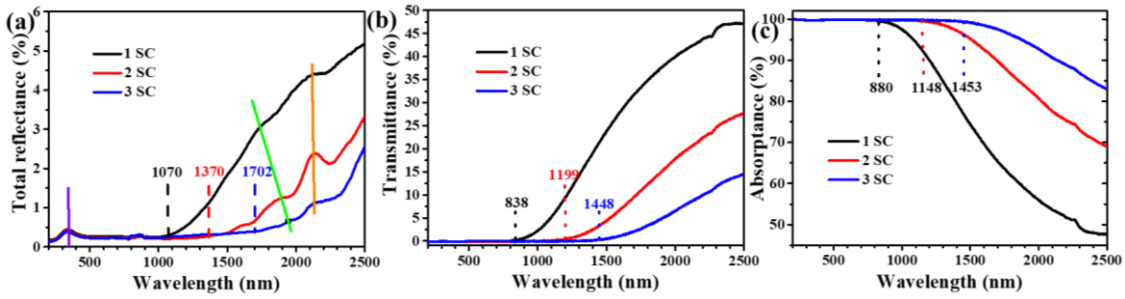

Figure 5-34 Ultra-broadband light trapping and its mechanism. (a) ~ (c) Tunable reflection, transmission and absorption spectra of 1 SC, 2 SC and 3 SC self-assembly Ag@SiO_2 nanostructures.

UV-Vis-NIR reflection, transmission and absorption spectra are measured to analyze the tunable optical properties of Ag@SiO_2 hybrid plasmonic nanostructures. As shown in Figure 5-34a, the 1 SC, 2 SC and 3 SC samples show different reflection edges of 1070, 1370 and 1702 nm, respectively. Three resonance peaks are observed in the reflection spectra. The peaks at the foremost (violet line, 343 nm) and the last (orange line, 2130 nm) stay at the exact same position, while the resonance peaks in the middle revealed observable redshifts (green line) from 1736 nm to 1943 nm. The average total reflections in the range from 200 to 2500 nm of the above three samples are calculated to be 1.9%, 0.8% and 0.5%, respectively, which shows an excellent light reflection property compared with other published work (see Table 5-5).[33,189,217–221] To our surprise, the transmission spectra (Figure 5-34b) of 1, 2 and 3 SC samples also indicate tunable transmission edges of 838, 1199 and 1448 nm. Please note that a large portion of IR light (λ<2500nm) could pass through the samples while almost all UV light and visible light are absorbed by them. Thus, it shows great potential for application in UV and visible light filters.

Table 5-5 Antireflective (AR) property compared to recently black nanostructure materials.

AR samples	methods[a]	Average reflection	range	References
3D Ag@SiO_2	**PVD+ALD**	**0.5%**	**200 – 2500 nm**	**This work**
Au	PVD	17%	300 – 800 nm	Ref.[189]
Ag/TiO_2/Si	CBD+WE	3.5%	300 – 1000 nm	Ref.[217]
PPy/TiO_2/Si	WE+HT	<4%	200 – 2300 nm	Ref.[218]
Black Si	RIE	1.1%	300 – 2500 nm	Ref.[38]
Ag@Si	LP	0.8%	300 – 1200 nm	Ref.[219]
Ag/Au/Si	CCT+ECD	<2%	250 – 2000 nm	Ref.[220]
Fe	PLD	1.2%	250 – 2000 nm	Ref.[221]

[a] CBD: chemical bath deposition; WE: wet etching; HT: hydrothermal method; SIT: soft imprint technology; LP: laser nanoprocessing; CCT: colloidal crystal templates; PLD: pulsed laser deposition

Absorption can be calculated by the equation: Absorptance = 100% - reflectance – transmittance.[33] These absorption results are presented in Figure 5-34c, where tunable absorption edges are still existed in the spectra, corresponding to 880, 1148, and 1453 nm, respectively. The average absorption in the range from 200 ~ 2500 nm increases from 78.5% to 91.4% to 96.4%. The absorption performance also shows comparable results to the published works (Table 5-6).[31,196–199,206,222,223] These results demonstrate that Ag@SiO_2 plasmonic nanostructures show a super-powerful capability towards tunable reflection, transmission and absorption property in the NIR range(λ<2500nm).

Table 5-6 Absorption performance compared to recently reported plasmonic nanostructure materials.

Samples	Average absorptance	Broadband absorption range	References
3D Ag@SiO2	**96.4%**	**200 – 2500 nm**	**This work**
3D Al@AAM	<90%	400 – 2500nm	Ref.[31]
Al nanostructure	92.6%	300 – 2500 nm	Ref.[196]
Au/Nanoturf	~ 94.3%	400 – 2500 nm	Ref.[197]
Ni SPhCs	~ 80%	250 – 2000 nm	Ref.[155]
TiN @Al_2O_3	~ 96%	300- 2000nm	Ref.[200]
PI NC/Au-W	~96%	300- 2500nm	Ref.[206]
3D Au@AAM	>90%	200- 2500 nm	Ref.[199]
Ti-SiO_2-Al	~97%	300 -1200 nm	Ref.[222]

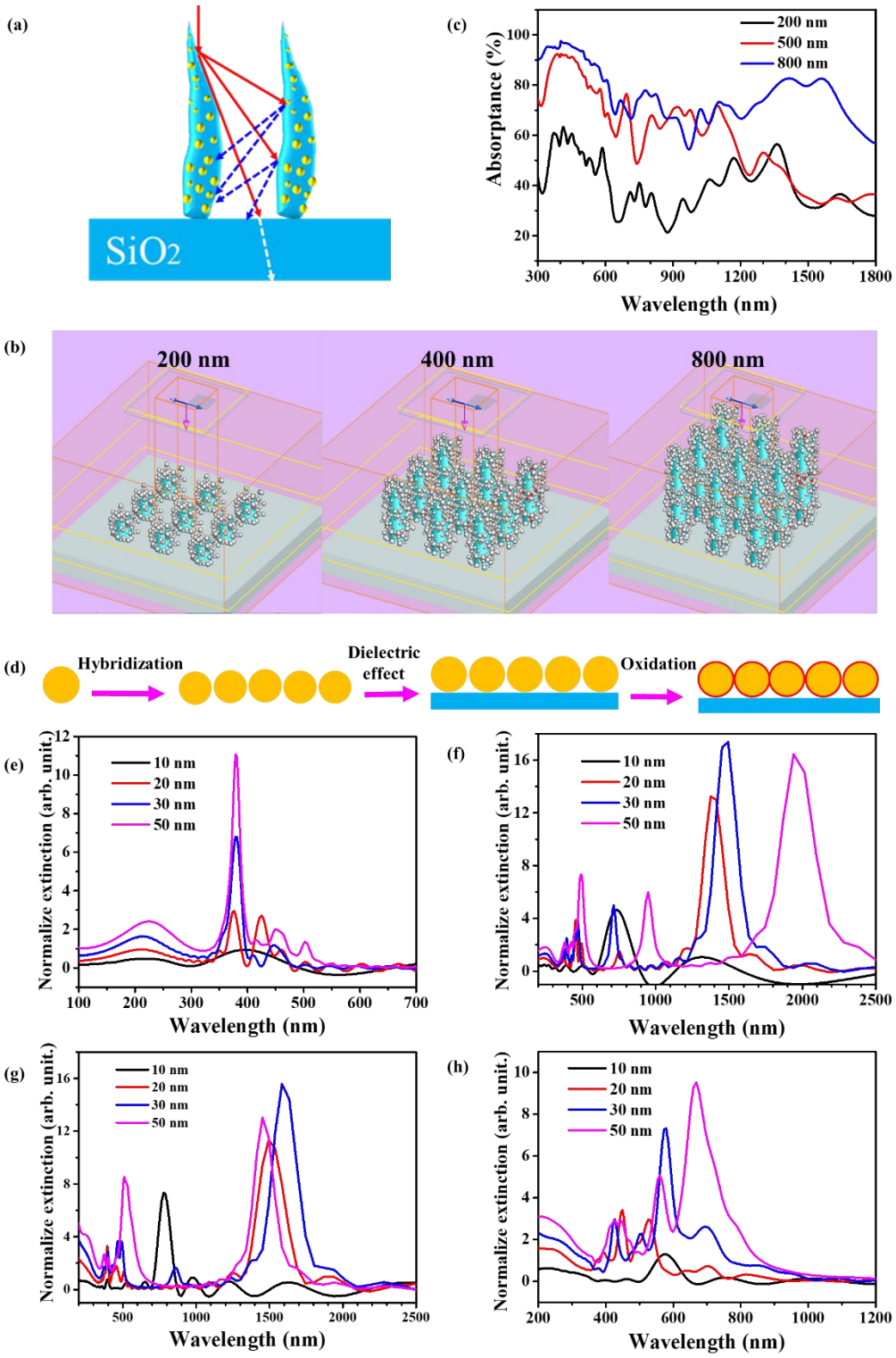

Figure 5-35 (a) Schematic illustration of multiple scatterings caused by the Ag@SiO_2 nanostructure. (b) Simulated reflection and transmission model constructed by FDTD software. Ag@SiO_2 hybrid plasmonic nanostructure with random Ag nanoparticle distribution on 200, 500 and 800 nm SiO_2. Blue pillars are SiO_2, gray particles are Ag nanoparticles and the bottom is the SiO_2 substrate with 2 nm Ag film on the surface. (c) Simulated absorptance for the height of 200, 500 and 800 nm Ag@SiO_2 plasmonic nanostructures. (d) Mie scattering simulated model for (e), (f), (g) and (h). (e) ~ (h)

Normalized extinction spectra for different diameters of single Ag nanoparticle, five aligned Ag nanoparticles, five aligned Ag nanoparticles on SiO_2 substrate and five aligned Ag nanoparticles with 2 nm Ag_2O oxidation layer on SiO_2 substrate, respectively.

As seen in Figure 5-31, the structural height and the amount of loaded Ag nanoparticles increases from 1 SC to 3 SCs. In order to investigate the structure-property relationship and explore the multiple forward scattering, simple 3D analog models have been designed, and FDTD simulation has been performed. As depicted in Figure 5-35a and 35b, multiple scattering is mainly dependent on the structural height. The number of scattering events increases with increasing structural height, resulting in a change in transmittance and reflectance.[33] Therefore, the absorptance increases as the height increases (Figure 5-35c). It is well consistent between the experimental results (Figure 5-34c), simulation results (Figure 5-35c) and previous results.[78]

In addition, several Ag nanoparticles with very close gaps can be often observed (Figure 5-33b), and it can lead to a strong plasmonic hybridization effect. Different models, including single Ag nanoparticle, 5 close located Ag nanoparticles, 5 close located Ag nanoparticles on a SiO_2 substrate (dielectric effect), 5 close located Ag nanoparticles with a thin Ag oxide layer on a SiO_2 substrate, were designed to study the hybridization effect (Figure 5-35d). For the simulation, the Ag particle size was also changed from 10 nm to 50 nm according to the results from Figure 5-33c. Figure 5-35e ~ 35h show the simulated extinction spectra of the different models with different particle size. The strong hybridization effect leads to multiple resonances and even more than 3 resonance peaks can be observed, and the multiple resonances redshift into NIR range with increasing particle size (Figure 5-35f). In addition, there are also clear influences from the dielectric SiO_2 and Ag oxides (Figure 5-35g and 35h).

So it can be concluded that a large scale collective effect of the light extinction in broadband can be obtained by the multiple scattering into the hierarchical structure. The collective overlap is from both SPR effects of many isolated Ag nanoparticles and

hybridization effects of many groups of close localized Ag nanoparticles. It can also be imagined that the multiple scatterings will cease somewhere in the hierarchical structure with infinite depth, and the light penetration depth can be defined as the depth with effective multiple scattering events in the forwards direction. It should be dependent on the structural features (such as particle distribution and particle size distribution). As seen in Figure 5-34b, the transmission edge redshifts with increasing structural height, indicating that the light penetration depth is also wavelength-dependent for our structure, and light with a larger wavelength should have a more considerable penetration depth.

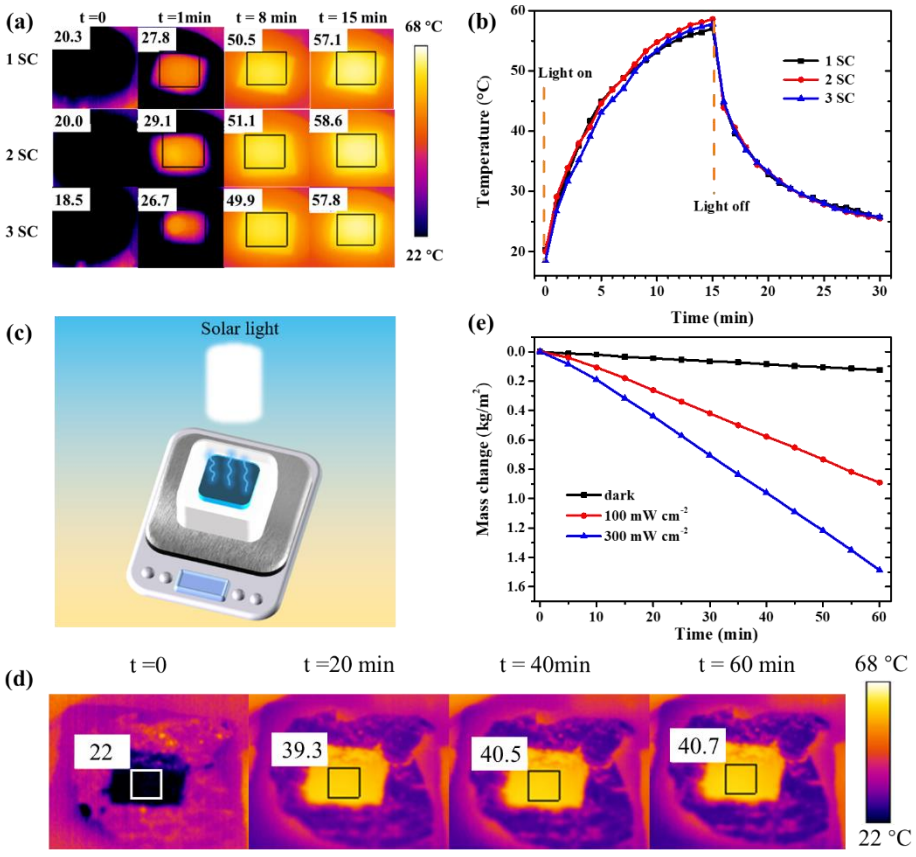

Figure 5-36 Localized heat effect for photothermal evaporation using Ag@SiO_2 plasmonic nanostructures. (a) The photothermal effect produced by 1 SC, 2SC and 3SC Ag@SiO_2 plasmonic nanostructure. The numbers in the upper left white rectangle show the average temperature in the center black rectangles. (b) Temperature changes with time for 1 SC, 2 SC and 3 SC Ag@SiO_2 plasmonic nanostructures when lighting on or off the Xe lamp under illumination of 100 mW cm^2 (1 sun). (c) Schematic picture for photothermal water evaporation. (d) Real-time temperature monitoring during water evaporation. The number in the upper left white rectangle shows the average temperature in the center square. (e) Mass change during water evaporation for 3 SC

$Ag@SiO_2$ plasmonic nanostructure under dark, 100 mW cm^{-2} and 300 mW/cm^2.

Due to the excellent extinction properties, our structures are quite interesting for efficient photothermal conversion towards applications in photothermal imaging, water purification and seawater desalination. As presented in Figure 5-36a, photothermal properties of the black $Ag@SiO_2$ plasmonic nanostructures with 1 SC, 2 SC and 3 SC indicate that increasing surface temperature as the illumination time rises and surface temperature differences (ΔT) of 36.8, 38.6 and 39.3 °C, respectively. Figure 5-36b shows that surface temperatures of 1 SC, 2SC and 3 SC samples change during light on for illumination and light off under dark conditions. All three temperature curves show similar temperature rise and fall at the same moment, indicating the three samples have similar photothermal conversion capabilities and cooling properties. Figure 5-36c shows the schematic picture of bottom-heat-based water evaporation experimental setup, where a balance is used to record the bulk water decrease, a thermal insulation polymer foam is acted as a water container, 2 × 2 cm^2 $Ag@SiO_2$ plasmonic nanostructure sample plays the role of the light absorber, 2 grams water is used for evaporation experiments and solar light is vertically shined on the sample. Figure 5-36d records the 3 SC $Ag@SiO_2$ plasmonic nanostructures sample's real-time surface temperature change under the illumination of 100 mW cm^{-2} at the time of 0, 20, 40 and 60 min. As depicted in Figure 5-36e, it only shows an evaporation rate of 0.125 $kg \cdot m^{-2} \cdot h^{-1}$ in the dark conditions while the evaporate rate is remarkably enhanced to 7.12 times and reaches 0.89 $kg \cdot m^{-2} \cdot h^{-1}$ under 100 mW cm^{-2} illumination. After evaporation, the XRD pattern (Figure 5-37a) and reflection property (Figure 5-37b) show almost the same as the pristine sample, which indicates its stability of structural and optical properties. When we further increase the illumination intensity to 200 mW/cm^2, the water evaporation rate further increases 11.9 times and obtains an evaporation rate of 1.49 $kg \cdot m^{-2} \cdot h^{-1}$. These results indicate 3D $Ag@SiO_2$ plasmonic nanostructures unambitiously reveal their great potentials in photothermal response applications, such as solar vapor generation.

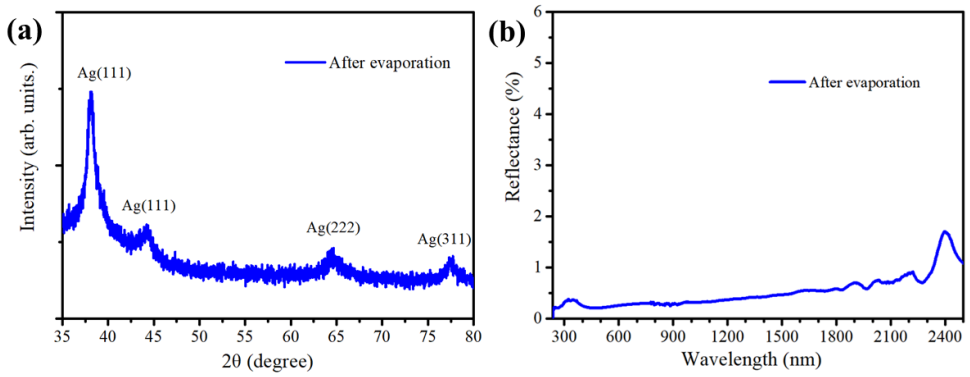

Figure 5-37 Structure stability test. (a) XRD patterns of 3SC Ag@SiO_2 sample after water evaporation. (b) Reflectance spectra of 3SC Ag@SiO_2 sample after water evaporation.

5.4.3 Conclusions

In summary, inspired by the surface structure on the coral tentacles, we have developed a MS-ALD self-assembly strategy for fabricating large area (153 cm^2) 3D Ag@SiO_2 hybrid plasmonic nanostructures. Experimental results indicate that 3D Ag@SiO_2 hybrid plasmonic nanostructures include random size distributions of Ag nanoparticles below 100 nm grown on hierarchically ordered branches on a trunk SiO_2. Adjustable reflection edges, transmission edges, and absorption edges are revealed in the prepared samples. 3 SC sample shows an ultralow reflection of 0.5% and high absorption of 96.4% across the range from 200 to 2500 nm. The multiple forward scattering and extinction effect produced by high Ag@SiO_2 nanostructures and Ag nanoparticles with random size distribution could be responsible for the tunable optical properties of reflection, transmission, and absorption. Furthermore, we use the 3 SC Ag@SiO_2 plasmonic nanostructure sample as the bottom-heated-based water evaporation light absorber and demonstrate it can significantly improve the evaporation rate to 7.12 times under 1 sun. We believe that large-area MS-ALD self-assembly of Ag@SiO_2 plasmonic nanostructures with controllable morphology and optical properties show great application prospects in energy harvesting, SPR sensing and detection, photothermal imaging, photothermal therapy, and photothermal disinfection.

6. Results of surface modification on black silicon for photoelectrochemical water reduction

6.1 Introduction of photoelectrochemical water reduction

With the advent of the carbon neutral era, searching new energy technologies for supplementing or replacing fossil energy is highly urgent and a must for modern society.[224–227] Hydrogen (H_2) as a green, regenerable and high energy-density gas can be used without producing any poisonous and harmful wastes.[228–230] So, developing H_2 energy technologies can efficiently reduce carbon dioxide (CO_2) emission and environmental problems, such as extreme climate and acid rain.[231–233] Nowadays, H_2 production mainly depends on water electrolysis and artificial photosynthesis.[234–236] However, most of the power source of electrolyzed water relies on fossil fuels, which directly speeds up CO_2 emission. Photocatalytic H_2 production with pure photocatalyst and without any bias is an ideal solution for carbon neutrality, because it only converts solar energy into chemical energy by photocatalyst, electrolyte and solar light.[236,237] But the rate of H_2 production is very low. Photoelectrochemical (PEC) H_2 production can make up the challenges faced by electrocatalytic and photocatalytic H_2 productions.[234,238–241] On one hand, it can take advantage of electric power to raise the rate of H_2 production and the H_2 yield. On the other hand, it can utilize solar energy for H_2 production and thus reduce the usage of electric power. Therefore, developing PEC H_2 production technology with high-efficiency, environmental friendliness and sustainability can make a considerable influence on “carbon neutral” society.

Silicon, a kind of narrow bandgap (1.1 eV) semiconductor, has been widely studied as the photoelectrodes of PEC water splitting.[89,131,240,242] However, the low absorption of solar light, poor electrocatalytic activity and being not resistant to photochemical corrosion make pure silicon not suitable for PEC water splitting.[243] So it is necessary to modify the silicon surface for improving these properties. Three possible strategies are put forward to increase the light absorption, improve photochemical corrosion resistance and enhance electrocatalytic activity. Firstly, the polished Si surface is etched

to form a micro-nanostructure surface, so that more light can be trapped in the structure. On one hand, the light absorption is highly enhanced;[244] on the other hand, due to the formation of the Si micro-nanostructure, it will lead to more contact area with electrolyte and thus its corrosion resistance ability obviously decreases. Therefore, a protective layer on the Si structure is absolutely necessary and the protective layer should not apparently influence the light absorption at the same time. Finally, an additional photocatalyst should be deposited to enhance the photocatalytic activity and improve charge transfer during the PEC water splitting. [87,243,245,246]

To address the above challenges, corresponding solutions are proposed. In order to form Si micro-nanostructure, self-masking reactive ion etching (RIE) can be used with good controllability and scalability.[33,247] TiO_2 can be introduced as the protective layer and ReS_2 is used as photocatalyst. Unlike typical trigonal prismatic (2H) multi-layers, such as MoS_2 and WS_2 with indirect bandgaps, ReS_2 is a direct bandgap semiconductor in the multi layers, which reveals a stable and conductive (octahedral) 1T phase at room temperature with better electron transportation behavior.[76,248] Moreover, the distorted T phase in ReS_2 can show excellent optical, mechanical, anisotropic electronic and catalytic properties.[77,248–253] In this chapter, it is presented that the performance of Si photocathode for PEC water splitting is largely enhanced through dual interface engineering and integrating with ReS_2 photocatalyst. By the first interface engineering step, the mirror-like Si changed to black silicon through surface nanostructuring, which largely promotes the light absorption. The second interface engineering step was the deposition of TiO_2 by ALD, and TiO_2 was changed from amorphous phase to anatase phase during the subsequent CVD growth of vertically-aligned ReS_2 nanosheets. After the CVD process, the vertical orientation of ReS_2 nanosheets is perpendicular to the Si substrate. It also verifies that the growth of ReS_2 monocrystalline nanosheets does not need a smooth substrate, which is necessary for the growth of single crystals. The as-prepared ReS_2/TiO_2/b-Si photocathode shows better PEC H_2 production performance in 0.5 M H_2SO_4 solutions than b-Si, TiO_2/b-Si and ReS_2/b-Si photocathodes. Compared

to b-Si under dark condition at a potential of 1.0 V vs RHE, the PEC performance of b-Si, ReS_2/b-Si, TiO_2/b-Si and ReS_2/TiO_2/b-Si improves to 6.1, 8.3, 30 and 89.6 times under solar light irradiation, respectively. The Electrochemical Impedance Spectroscopy (EIS) analysis and Mott-Schottky plot analysis indicate that the crystalline TiO_2 layer plays an important role here, not only by improving the electrode stability, but also by adjusting the band structure and increasing the system charge transfer kinetics.

6.2 Results and discussion

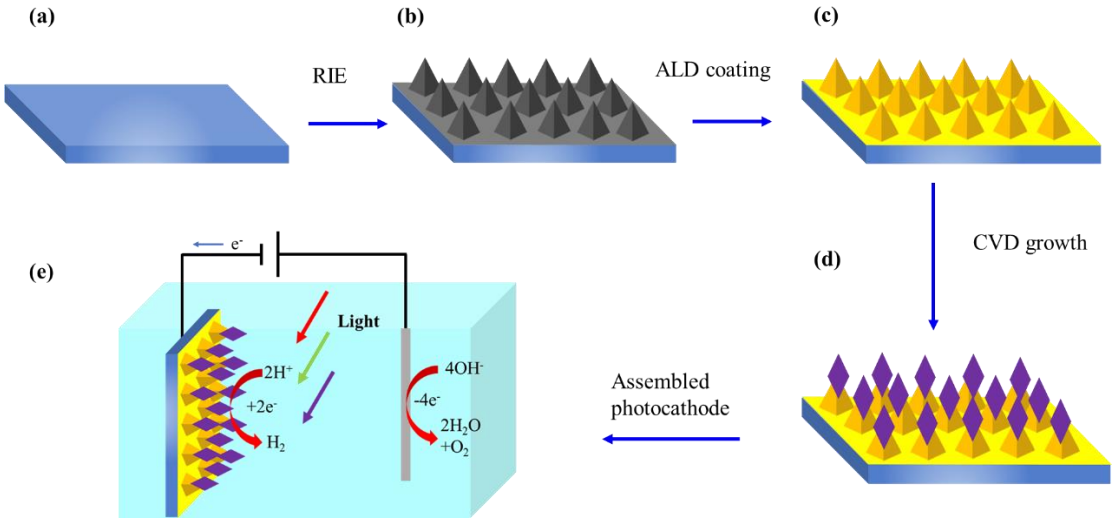

Figure 6-1 Flow chart of assembled Si-based photocathode. (a) Pristine silicon substrate. (b) b-Si formed by the RIE etching. (c) Coated TiO_2 on the b-Si by ALD. (d) Growth of ReS_2 on TiO_2/b-Si sample by CVD. (e) Schematic diagram of PEC water splitting using ReS_2/TiO_2/b-Si photocathode.

The assembly of the ReS_2/TiO_2/b-Si photocathode mainly consists of four steps (Figure 6-1a ~1d): At first, black silicon with surface nanostructures is fabricated using self-masking RIE. After that, it is cleaned by piranha solution and HF dipping (Figure 6-1b). Secondly, 10 nm TiO_2 is coated on the b-Si as the protective layer (Figure 6-1c). Immediately prior to the ALD coating, the black silicon is treated with HF acid again to remove the native SiO_2 layer. Then, ReS_2 is grown on the TiO_2/b-Si substrate as the photocatalyst by using CVD (Figure 6-1d). Finally, the as-prepared ReS_2/TiO_2/b-Si as photocathode, Ag/AgCl as the reference electrode and Pt wire as the counter electrode are immersed into H_2SO_4 electrolyte for PEC water splitting with solar light irradiation (Figure 6-1e).

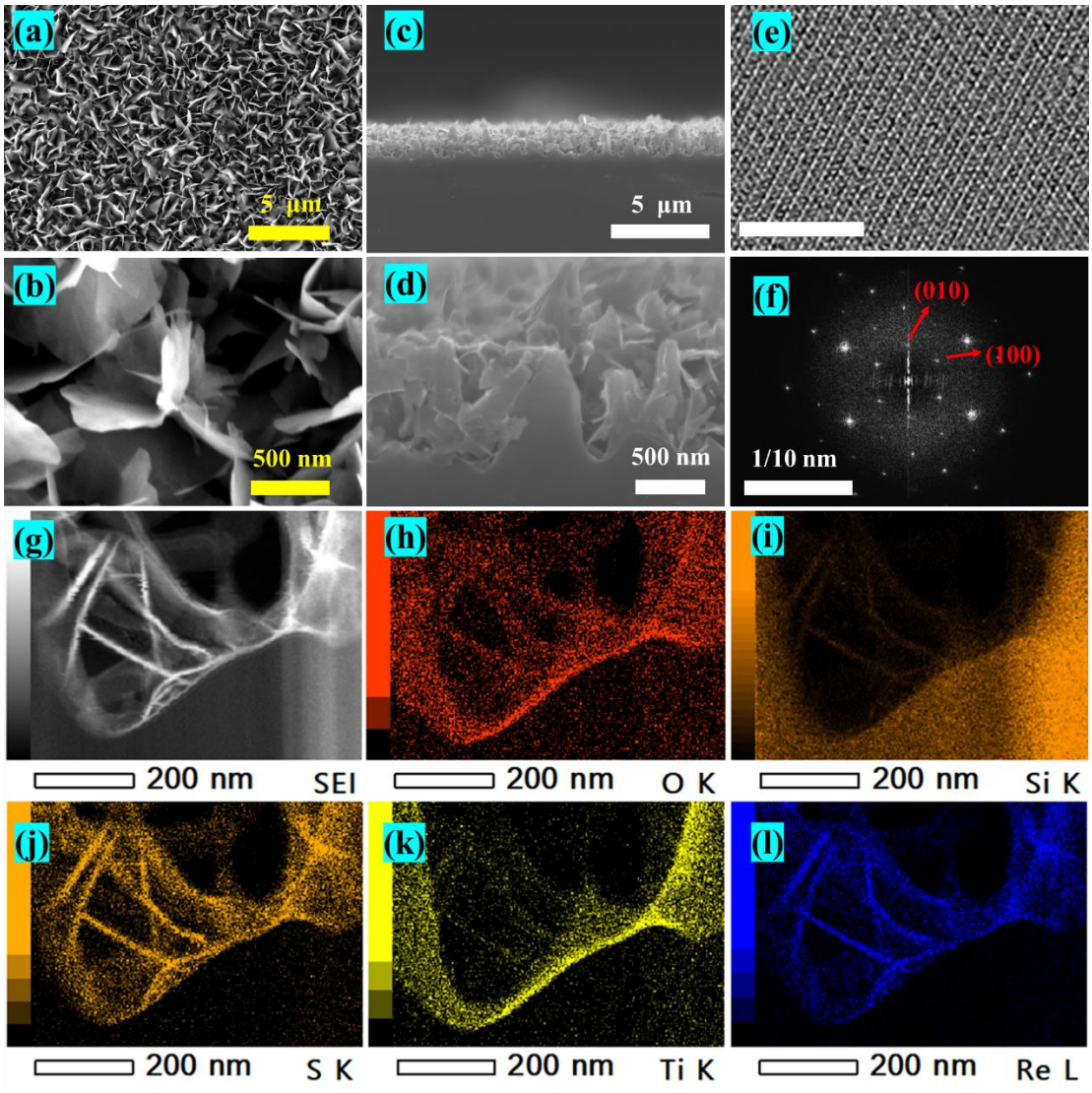

Figure 6-2 (a) and (b) Top-view SEM images of ReS_2/TiO_2/b-Si with low and high magnifications. (c) and (d) Cross-section view of SEM images of ReS_2/TiO_2/b-Si with low and high magnifications. (e) High-resolution (HR) TEM image of ReS_2 nanosheet. Scale bar is 5 nm. (f) Its corresponding FFT patterns in (e). (g) Cross-sectional scanning TEM (STEM) image of ReS_2/TiO_2/b-Si heterostructure, and its corresponding elemental mapping images of (h) oxygen, (i) silicon, (j) sulfur, (k) titanium and (l) rhenium.

As-prepared samples were firstly characterized by SEM characterizations. Figure 6-2a shows the uniform distribution ReS_2 nanosheets with a large portion of vertically-aligned orientation. The thickness of ReS_2 nanosheets is about several nanometers (Figure 6-2b). The cross-section of ReS_2/TiO_2/b-Si heterostructure was also analyzed by SEM (Figure 6-2c and 6-2d), which indicated that the ReS_2 nanosheets were tightly grown on the surface of the nanopyramids. It was also demonstrated that the growth of

ReS_2 single crystal nanosheet did not need a polished substrate or a small lattice mismatch. Such an advantage is promising to promote the related application development, such as energy storage,[248] photodetector,[254] water treatment[255] and so on.[251] The crystallinity of ReS_2 nanosheets was further investigated by TEM characterizations. In Figure 6-2e, an HR-TEM image of ReS_2 nanosheets is shown. The regular atom arrangement suggests that the ReS_2 nanosheet is of high quality and reveals good crystalline structure without defects. This is beneficial for the electron transfer during PEC water splitting. Hexagonal FFT pattern (Figure 6-2f) with good symmetry also verifies its single crystal quality. Figure 6-2g shows a representative cross-sectional STEM image of ReS_2/TiO_2/b-Si heterostructure with interfaces. Figure 6-2h ~ 2l are the corresponding elemental mapping images. Obviously, oxygen mainly comes from the TiO_2 layer and silicon native oxide, Si is from the substrate, S and Re belong to ReS_2, and Ti element is also originating from TiO_2. It is noted that about a 10 nm thick TiO_2 layer is presented between the ReS_2 and b-Si, which can be easily seen in Figure 6-2h and 6-2k, where the existence of two interfaces of ReS_2/TiO_2 and TiO_2/b-Si in the ReS_2/TiO_2/b-Si heterostructure is confirmed.

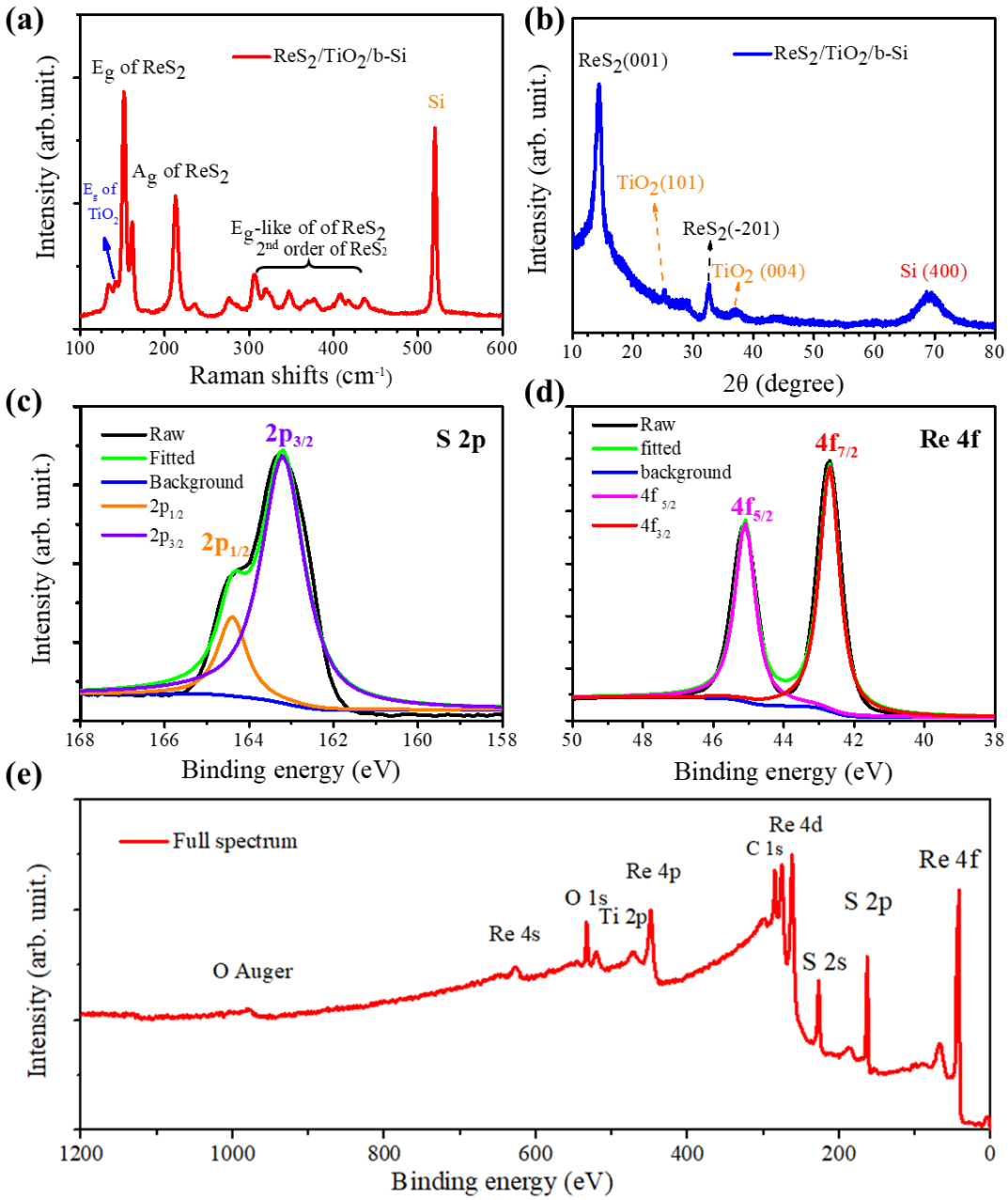

Figure 6-3 (a) Raman spectra of ReS_2/TiO_2/b-Si. (b)XRD pattern of ReS_2/TiO_2/b-Si. (c) and (d) XPS spectra of S 2p orbit and Re 4f orbit binding energies. (e) A full XPS spectrum of the ReS_2/TiO_2/b-Si.

Raman measurements have been carried out to explored the characteristic features of ReS_2/TiO_2/b-Si. As presented in Figure 6-3a, the peak located at 520 cm^{-1} belongs to Si standard peak.[38] The peak located at 143 cm^{-1} is assigned to E_g vibration mode of the anatase TiO_2.[256] The three main peaks lying at 160 cm^{-1}, 212 cm^{-1}, 306 cm^{-1} are classified to in-plane (E_g) vibration, like in-plain (E_g-like) vibration and out-of-plane (A_g) vibration of ReS_2, respectively.[248,249] The peaks located at Raman shifts above 400

cm^{-1} and below 500 cm^{-1} are 2nd order Raman peaks of ReS_2 nanosheets.[248] Thus, the compositions of ReS_2/TiO_2/b-Si are confirmed by Raman measurement. XRD patterns are measure to identify the crystal structure of ReS_2/TiO_2/b-Si. As shown in Figure 6-3b, the b-Si peak located at 69.3° is the (400) facet of crystalline silicon.[38] The peaks at $2\theta = 25°$ and 37.5° are (101) and (004) plane of the anatase phase TiO_2.[257] The remaining peaks in the diffractograms belong to the ReS_2 nanosheets. Here, the XRD measurements well agree with the Raman characterizations.

In order to further identify the chemical compositions of ReS_2, high-resolution XPS spectra are showed in Figure 6-3c and 6-3d. The XPS spectra of ReS_2 is shown in Figure 6-3c and 6-3d. Obviously, S $2p_{1/2}$ and S $2p_{3/2}$ are located at the binding energy of 163.2 eV and 144.4 eV, respectively. Owing to the spin-orbit splitting of the Re 4f, the Re $4f_{3/2}$ shows a binding energy of 42.7 eV, while Re $4f_{5/2}$ indicates a binding energy of 45.1 eV, representing the Re^{+4} state. Full XPS spectra (Figure 6-3e) ranging from 1200 eV to 0 eV is measured to analyze the compositions of ReS_2/TiO_2/b-Si. The results indicate that there is almost no impurity in the sample. Combined with all the characterizations, the fabrication of ReS_2/TiO_2/b-Si is confirmed.

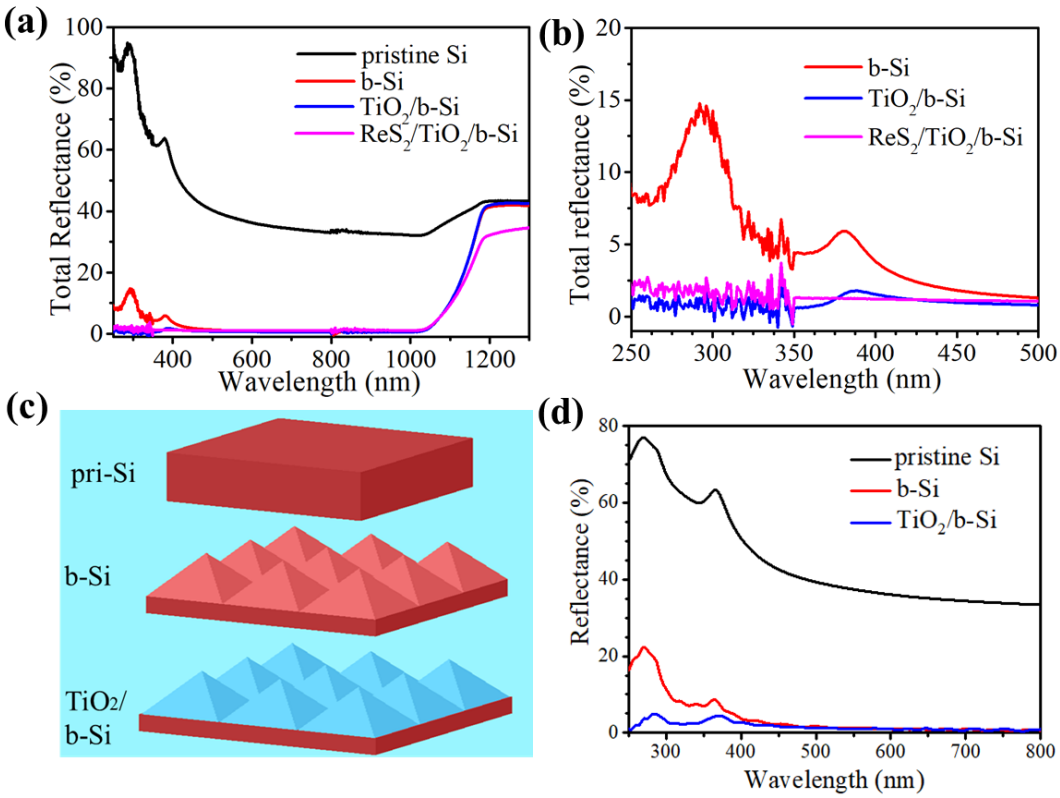

Figure 6-4 (a) Total reflectance of different Si-based samples. (b) Enlarged region from 250 nm to 500 nm in a. (c) The different models for FDTD simulation. (d) Simulated reflectance for pristine Si, b-Si, and b-Si with 10 nm TiO_2.

As the planar silicon is polished, it can reflect a large portion of light (Figure 6-4a), leading to a low absorption efficiency. In order to reduce the reflection and increase the absorption, the polished silicon is processed by RIE etching to produce micro-nanostructures for light trapping. Obviously, b-Si with abundant surface nanostructures shows a very low reflection below the cutoff wavelength (1110 nm) of silicon. However, the intrinsic reflections at around 300 nm and 375 nm are over 5% (Figure 6-4b). After a thickness of 10 nm TiO_2 is coated on the b-Si, the reflection is largely decreased possibly due to a top layer with lower refractive index than the Si substrate. Thus, 10 nm crystalline TiO_2 not only can protect the b-Si from being oxidized, but also can improve light trapping. Finally, with the growth of ReS_2, the ReS_2/TiO_2/b-Si doesn't show apparent change regarding the total reflection.

To further explore the influences of different interfaces on the light trapping properties,

three models (pristine Si, b-Si and b-Si with 10 nm TiO_2) are constructed, as presented in Figure 6-4c. The simulated reflection can be found in Figure 6-4d. The results are in good accordance with the measured reflection results shown in Figure 6-4a. Thus, it is reasonable to apply these models for investigating the light-silicon interaction.

We choose three typical wavelengths of 400 nm, 600 nm and 800 nm (below the cutoff wavelength of silicon) to investigate the light interaction with different silicon-based samples. For the case of pristine Si in Figure 6-5a~5c, the local field enhancement is clearly stronger in both nanostructured Si with (Figure 6-5d~5f) and without TiO_2 layer (Figure 6-5g~5i) than that of the flat Si. At an incident wavelength of 400 nm, the field enhancement is mainly observed at the Si-vacuum interface, while it becomes stronger inside of the Si structure as the incident wavelength changes to 600 nm and 800 nm. All these confirm the improved light trapping in the nanostructures.[33]

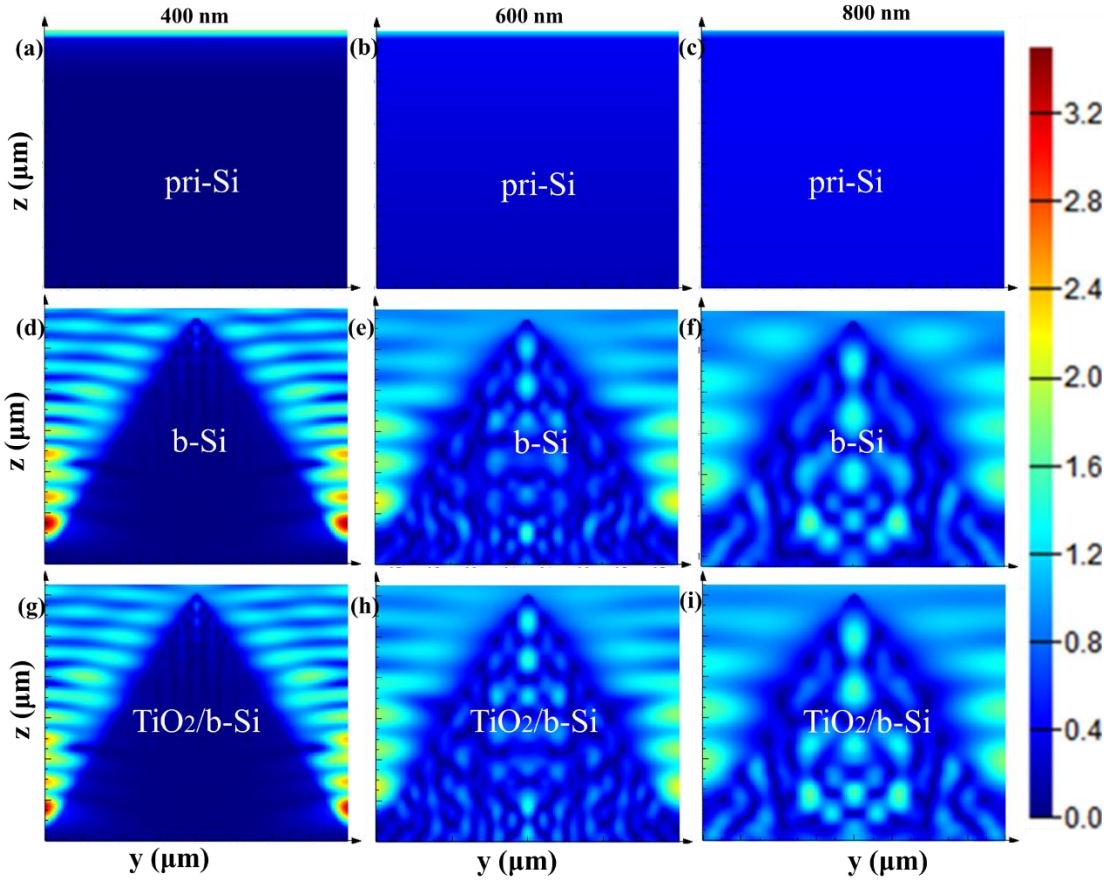

Figure 6-5 (a)~(c), (d)~(f) and (g)~(i) Electric field enhancement induced by 400 nm, 600 nm, 800 nm incident light interaction with the pristine Si, b-Si and TiO_2/b-Si, respectively. Simulation area: 1.6 μm (y axis) × 2.5 μm (z axis). The color scale is

$|E|/|E_0|$.

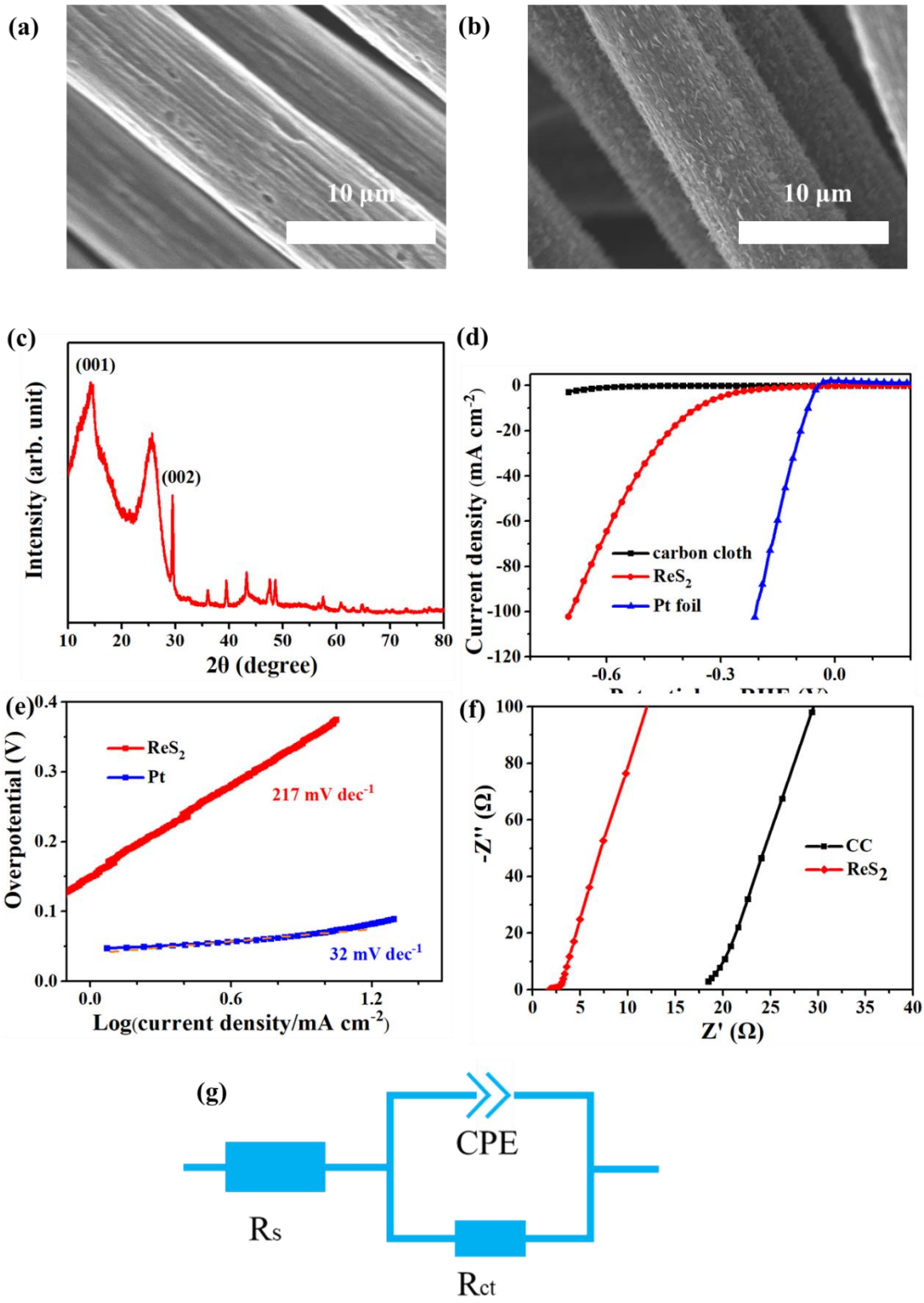

Figure 6-6 (a) SEM image for carbon cloth substrate. (a) SEM image for ReS_2 on carbon cloth substrate. (c) Figure S8 XRD pattern for ReS_2 on carbon cloth substrate. The marked (001) and (002) reflections belong to ReS_2, while the other peaks are classified to belong to the carbon cloth substrate.[258] (d) LSV curves of carbon cloth,

ReS_2/CC and Pt foil. (e) Tafel slope of ReS_2/CC and Pt foil. (f) EIS of carbon cloth and ReS_2/CC. (g) The corresponding equivalent circuits for CC and CC/ReS_2 electrodes. R_s is series resistance, CPE is capacitance phase element and R_{ct} is charge transfer resistance.

Prior to PEC test, the electrocatalytic hydrogen evolution (HER) activity of ReS_2 on carbon cloth (ReS_2/CC) is explored. As the evidence of ReS_2/CC, SEM images and XRD pattern can be seen in Figure 6-6a~6b and Figure 6-6c. The electrocatalytic performances of commercial Pt foil and commercial CC are also compared in Figure 6-6d. The Pt foil shows the best HER activity, while the bare CC presents almost no HER activity. After the growth of ReS_2 on the CC, the ReS_2/CC shows obviously HER activity improvement compared to bare CC. It shows a 0.367 V overpotential at the current density of 10 mA cm^{-2}, indicating that ReS_2 is benefit for HER and can be used as HER catalyst for water splitting. As depicted in Figure 6-6e, ReS_2/CC demonstrates a Tafel slope of 217 mV dec^{-1} compared with that of Pt foil (32 mV dec^{-1}). Figure 6-6f presents the EIS data of CC and ReS_2/CC and their corresponding equivalent circuits (Figure 6-6g). It reveals that ReS_2/CC has a lower R_{ct} value of 7.3 Ω and higher capacitance value of 0.28 mF than those of 19.5 Ω and 2.6 $\times 10^{-3}$ mF in CC (as seen in Table 6-1), respectively, which directly demonstrates the improved charge transfer at the ReS_2/CC-electrolyte interface than the CC-electrolyte interface. All these confirm that ReS_2 can be used as a promising HER catalyst.

Table 6-1 Fitting parameters obtained by fitting the Nyquist plots shown in Figure 6-6f with the equivalent circuit models presented in Figure 6-6g.

cathode	R_S (Ω)	CPE (μF)	R_{ct} (Ω)
CC	19.5	2.6	125.6
ReS_2/CC	2.2	290	7.3

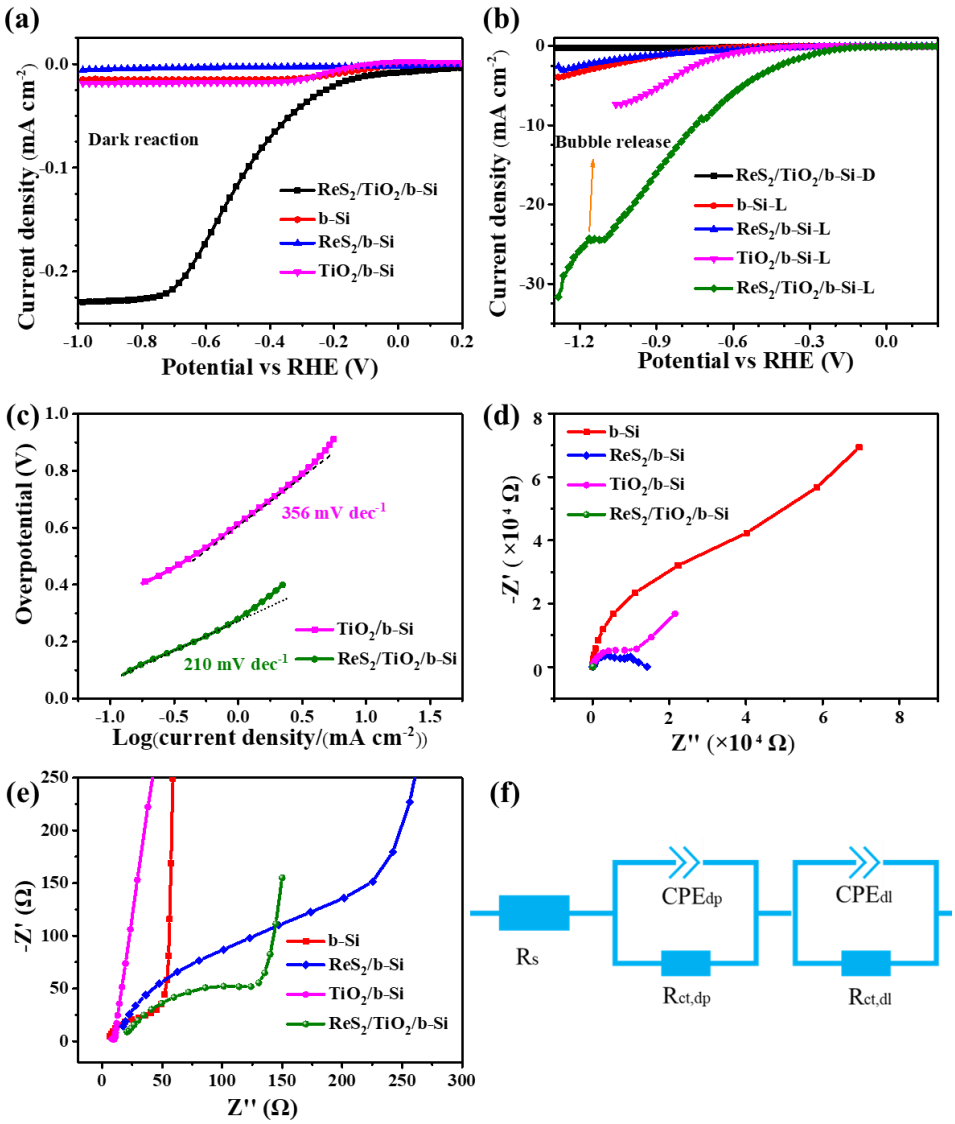

Figure 6-7 PEC properties of Si-based photocathodes. (a) Dark reactions of b-Si, ReS_2/b-Si, TiO_2/b-Si and ReS_2/TiO_2/b-Si. (b) Illuminated reactions of b-Si, ReS_2/b-Si, TiO_2/b-Si and ReS_2/TiO_2/b-Si. (c) Tafel slopes of TiO_2/b-Si and ReS_2/TiO_2/b-Si photocathodes. (d) EIS curves of b-Si, ReS_2/b-Si, TiO_2/b-Si and ReS_2/TiO_2/b-Si, and (e) the enlarged view under 1 sun illumination at -0.67 V vs RHE. (f) The corresponding equivalent circuits for TiO_2/b-Si, ReS_2/b-Si and b- ReS_2/TiO_2/b-Si photocathodes. R_s is series resistance, CPE_{dp} is the capacitance phase element for the depletion layer of the TiO_2/b-Si, ReS_2/b-Si and ReS_2/TiO_2/b-Si. $R_{ct,dp}$ is the charge transfer resistance for the depletion layer of TiO_2/b-Si, ReS_2/b-Si and ReS_2/TiO_2/b-Si. CPE_{dl} is the capacitance phase element for the double layer at the interface between photocathode and electrolyte. $R_{ct,dl}$ is the charge transfer resistance for the double layer at the interface between photocathode and electrolyte.[259]

In order to better understand the influence of different cathode materials, we conduct HER under dark condition (Figure 6-7a). Obviously, b-Si, ReS_2/b-Si, TiO_2/b-Si and

ReS_2/TiO_2/b-Si cathodes show very weak electrocatalytic activation. However, when we operate these electrodes under illumination, their HER performances are remarkably enhanced during the PEC water splitting process. As presented in Figure 6-7b, the ReS_2/TiO_2/b-Si shows the best PEC water splitting performance, while the b-Si obtains the worst one. The PEC performance of b-Si, ReS_2/b-Si, TiO_2/b-Si and ReS_2/TiO_2/b-Si improves to 6.1, 8.3, 30, 89.6 times, respectively, compared to b-Si under dark condition at the potential of -1.0 V vs RHE. As shown in Figure 6-7c, the Tafel slopes for ReS_2/TiO_2/b-Si and TiO_2/b-Si are 210 mV dec^{-1} and 356 mV dec^{-1}, respectively. The Tafel slopes for b-Si and ReS_2/b-Si are not calculated due to their poor PEC water splitting performance.

Comparing the data between the ReS_2/b-Si and b-Si electrodes in Figure 6-7a and 6-7b, it is noticeable that the performance slightly degraded under both dark and illuminated conditions when the catalyst ReS_2 is deposited on b-Si. As the catalyst ReS_2 is added, the active catalytic surface area should be clearly enlarged. Why the performance actually degraded is not clear yet. Besides, the same ReS_2 with the same deposition process parameters and similar structural parameters are used in both cases, and the active catalytic surface area should be similar for both ReS_2/b-Si and ReS_2/TiO_2/b-Si electrodes. Why is the performance of the ReS_2/TiO_2/b-Si electrode much better and what a role does the TiO_2 layer play? In order to answer these questions, both EIS measurements and Mott-Schottky measurements are performed.

EIS measurements are carried out to analyze the electrode-electrolyte interface behavior. The benefit of the ReS_2/TiO_2/b-Si photocathode can be seen in Figure 6-7d and 7e when EIS was applied to explore the electrode kinetics under 1 sun at -0.67 V vs RHE. The EIS Nyquist curves of b-Si, ReS_2/b-Si, TiO_2/b-Si and ReS_2/TiO_2/b-Si are plotted in Figure 6-7d and 5-7e and the corresponding equivalent circuit is presented (Figure 6-7f). The charge transfer resistance $R_{ct,dl}$ is determined for the catalytic activity.[95,259] The ReS_2/TiO_2/b-Si photocathode has a minimum value of $R_{ct,dl}$ = 115 Ω (Table 6-2), being

much smaller than those of bare b-Si, ReS_2/b-Si and TiO_2/b-Si and confirming the best performance. Compared with the b-Si electrode, the small performance degradation of ReS_2/b-Si electrode even with better catalyst should be due to the suppressed or hindered charge transfer.

Table 6-2 Fitting parameters obtained by fitting the Nyquist plots shown in Figure 6-7d and 7e with the equivalent circuit models presented in Figure 6-7f.

Photocathode	R_S (Ω)	CPE_{dp} (μF)	$R_{ct,dp}$ (kΩ)	CPE_{dl} (μF)	$R_{ct,dl}$ (kΩ)
b-Si	6.5	\	\	7.7	107
ReS_2/b-Si	18.8	0.26	0.187	4.7	9.0
TiO_2/b-Si	9.6	17.7	4.4	43.1	18.3
ReS_2/TiO_2/b-Si	25.8	15.8	3.0	0.57	0.115

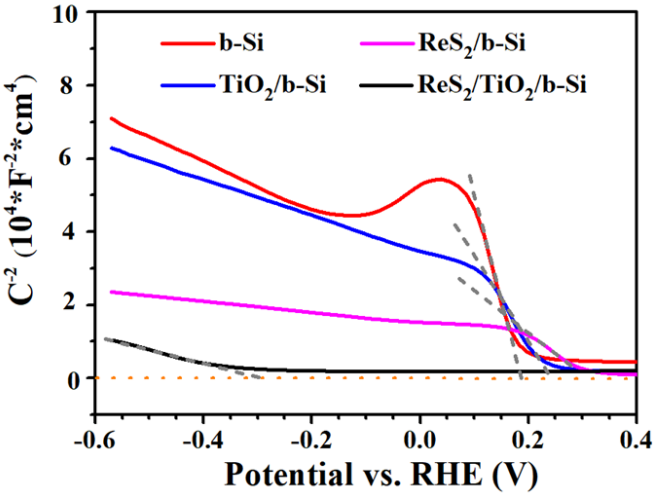

Figure 6-8 Mott-Schottky curves of b-Si, ReS_2/b-Si, TiO_2/b-Si and ReS_2/TiO_2/b-Si.

Mott-Schottky measurements (Figure 6-8) are conducted in dark condition to investigate the band bending at the interface between the electrode and the electrolyte. The b-Si, ReS_2/b-Si, TiO_2/b-Si and ReS_2/TiO_2/b-Si photocathodes show the flat-band

potentials (U_{fb}) of 0.19 V, 0.32 V, 0.23 V and -0.29 V, respectively. Basically, for the PEC water splitting, the U_{fb} should be close to the onset potential (V_{onset}) such that the overpotential (i.e., $V_{onset} - U_{fb}$) can be possibly small.[95,260] According to Figure 6-7b, ReS_2/TiO_2/b-Si has the V_{onset} of ~ -0.28 V, which is the closest to its corresponding U_{fb}, delivering the best PEC water splitting performance. All the three electrodes b-Si, ReS_2/b-Si and TiO_2/b-Si have large flat-band potentials, and the flat-band potential of ReS_2/b-Si electrode is the largest one with value of 0.32 V and far from the V_{onset} of ~ -0.28 V, which can suppress the charge transfer kinetics. This is probably the reason that the ReS_2/b-Si sample demonstrated a little degradation of performance under both dark and illuminated conditions (Figure 6-7a and 7b) compared to the other samples. Its performance is even worse than TiO_2/b-Si although ReS_2 has better catalytic property than TiO_2. Altogether, this suggests that the degradation of the charge transfer kinetics through the ReS_2/b-Si interface is the main problem, but it is still not clear what exactly happens at the interface. By adding a TiO_2 layer between b-Si and ReS_2, the flat band potential between electrode and electrolyte and the overpotential for HER are clearly reduced and charge transfer kinetics of the system is dramatically improved. In order to understand the important role of the TiO_2 layer, the energy band information before equilibrium is provided in Figure 6-9a,[261,262] and band alignment and energy bending are shown in Figure 6-9b and 9c. It is clear that the heterojunction between Si and TiO_2 is favored for the charge separation (Figure 6-9b) and an enhanced photoelectrical effect helps much here.

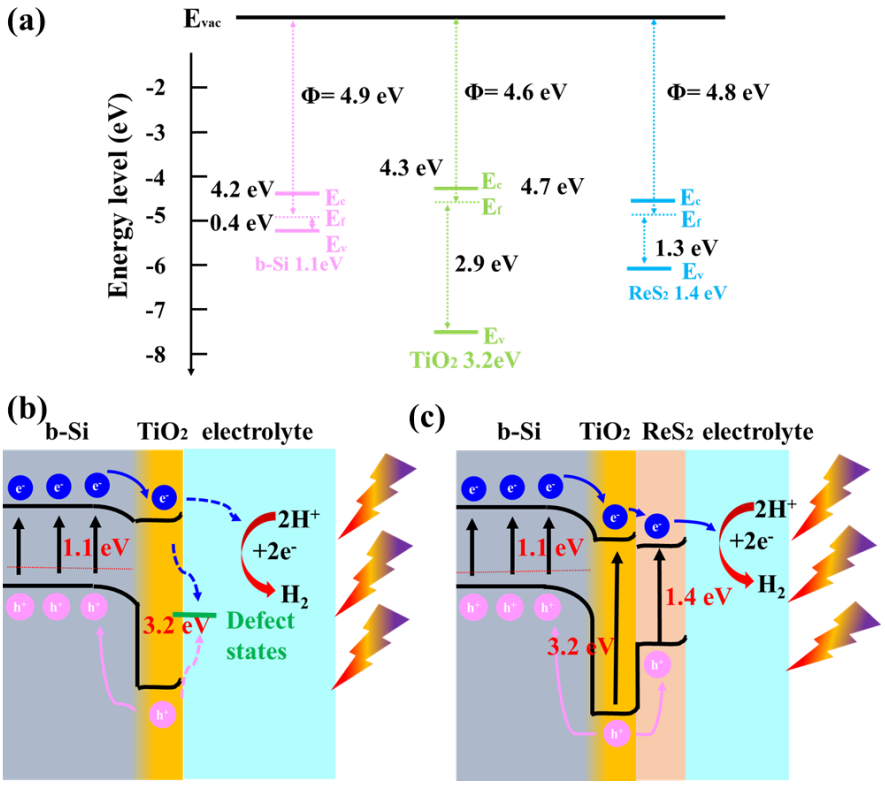

Figure 6-9 PEC water splitting mechanism. (a) Energy band structures of p-type Si, TiO_2 and ReS_2. Φ, E_{vac}, E_c, E_v, E_f means work function, vacuum energy level, the minimum of conduction band, the maximum of valence band and fermi energy level, respectively. (b) Schematic picture of TiO_2/b-Si photocathode for PEC water reduction. The pink dash lines are the fermi energy levels within the semiconductors. (c) Schematic picture of ReS_2/TiO_2/b-Si photocathode for PEC water reduction.

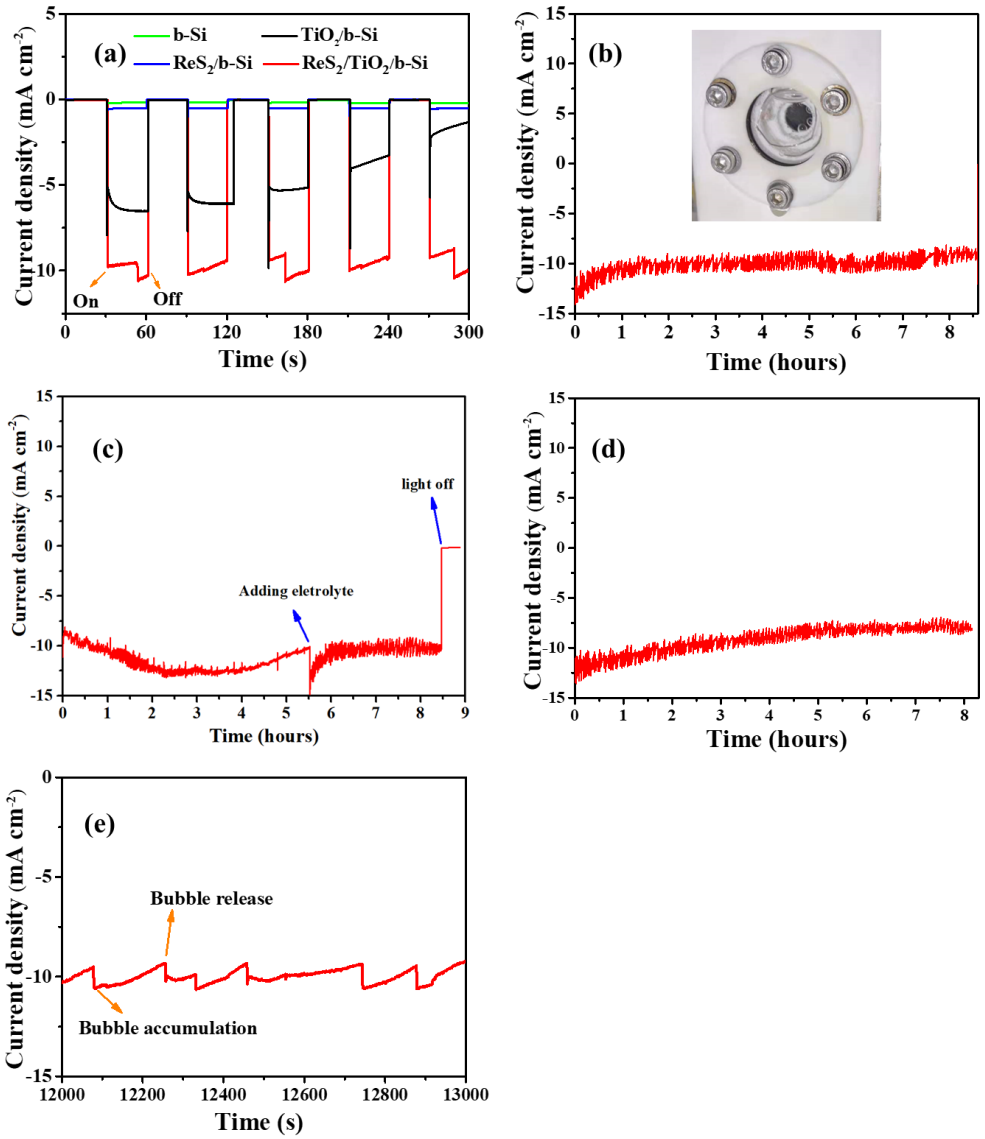

Figure 6-10 (a) Transient photocurrent responsive curves under repeatedly light-on and light-off. (b)~(d) Stability test for ReS_2/TiO_2/b-Si photocathode, inset is the photograph of the PEC cell with bubbles generation during the stability test. (e) The enlargement curve in b to clarify the influence of bubbles.

The photo-responsive properties of different photocathodes are investigated to explore the photocatalytic activities at the potential 0.67 V vs RHE. As depicted in Figure 6-10a, the different photocathodes show different current density responses when the lamp is repeatedly switched off and on. In the dark condition, all the electrodes present almost no current density response. However, upon illumination, the current densities increase rapidly and the ReS_2/TiO_2/b-Si shows the highest and most stable current density, while the TiO_2/b-Si declines obviously, indicating the poor catalytic property

of TiO_2. In addition, we measured 3 times the stability of ReS_2/TiO_2/b-Si photocathode for over 8 hours (See Figure 6-10b~d), the PEC water splitting performance doesn't show apparent decline. The electrode stability is well maintained by the 10 nm thick crystalline TiO_2 layer during the PEC water splitting process. In addition, the generated H_2 bubbles are visible in the inset of Figure 6-10b. Enlarged view shown in Figure 6-10e clarifies that the current density fluctuation is owing to the successively bubble accumulation and bubble release on the photoelectrode surface.

After the PEC tests, the morphology of b-Si/TiO_2/ReS_2 is compared with the initial as prepared sample. The SEM results (Figure 6-11a and 11b) indicate that the surface nanostructure does not change too much. The crystalline structure of b-Si/TiO_2/ReS_2 remains similar after the PEC test as comparing the XRD results between Figure 6-11c and Figure 6-3b. But its reflectance (Figure 6-11d) below the cutoff wavelength shows a little increase. It is thought that the sample surface was slightly damaged when it was mounted on the PEC cell. Generally, the b-Si/TiO_2/ReS_2 photocathode can retain a good stability during the PEC water splitting process.

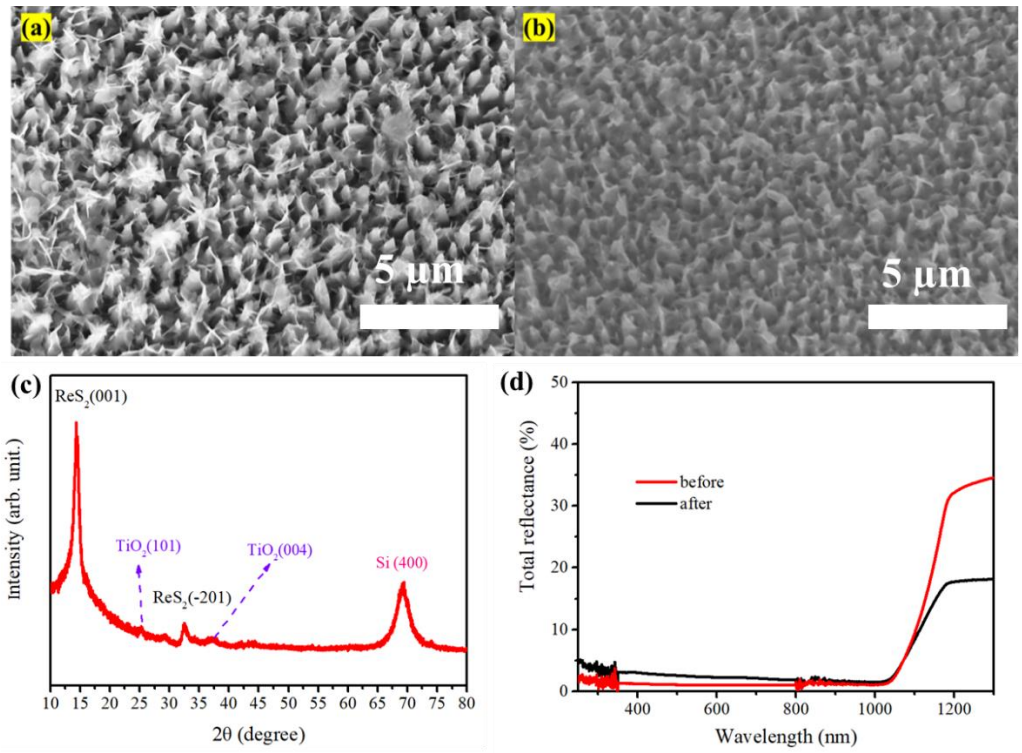

Figure 6-11 SEM pictures for ReS_2/TiO_2/b-Si photocathodes before (a) and after (b) stability tests. (c) XRD pattern after PEC stability test of the ReS_2/TiO_2/b-Si. (d) Optical

properties for ReS_2/TiO_2/b-Si photocathode before (a) and after (b) stability test.

6.3 Conclusion

An effective strategy including dual interface engineering and photocatalyst deposition is put forward to improve the PEC performance of Si-based photocathode: the Si surface is nanostructured to enhance the light absorption, a TiO_2 layer is deposited as protective layer, and then ReS_2 nanosheets are grown as photocatalyst. In this strategy, the crystalline TiO_2 layer plays a key role for the largely enhanced PEC performance for water reduction. On one hand, TiO_2 and ReS_2 protect the photocathode from being corroded and improve its durability. On the other hand, b-Si/ReS_2 show a degraded performance due to the suppressed charge transfer kinetics by the flat band potential between electrode and electrolyte. However, by placing the 10 nm crystalline TiO_2 layer between b-Si and ReS_2, the band structure of the whole electrode becomes more favorable towards a reduced overpotential for the PEC and an improved charge transfer kinetics. These universal strategies based on Si micro-nanostructuring, protective layers and photocatalyst deposition can be extended to other Si-based photoelectrode engineering for enhancing the PEC performance.

7. Summary and outlook

In summary, we fabricated several kinds of broadband light absorbers by advanced micro/nanofabrication technologies for solar energy harvesting and conversion applications, and the related photothermal water evaporation, photo-thermoelectric conversion and PEC water reduction performance were investigated in detail. We applied RIE technology to etch Si micro/nanostructures for light trapping, which significantly enhanced photo-thermoelectric conversion and photothermal water evaporation performance. Moreover, we also used MS-ALD combined with PVD method to fabricate 3D Ag@SiO_2 nanostructure for ultra-broadband solar light capture, and it also show better photo-thermoelectric conversion and photothermal water evaporation performance than b-Si absorber due to the improvement of solar convertors. Furthermore, we explored the possibility for PEC water reduction by depositing TiO_2 thin layer (ALD) as protective layer and ReS_2 as photocatalyst (CVD) on b-Si, which shows a remarkably improvement on PEC performance due to band alignment of different layers.

Firstly, surface nanostructured b-Si with excellent light trapping performance has been prepared by self-masking RIE method. The excellent light trapping performance (~ 98.9% absorption) of the b-Si is due to multiple scattering of light and enhanced free carrier absorption in the nanostructures. By integrating the b-Si with a thermoelectrical generator, we successfully demonstrated a significantly higher conversion from solar energy to electric power. Especially solar energy exceeding 1110 nm wavelength, i.e. above the band gap, can also be utilized efficiently.

Secondly, we demonstrate that the b-Si can also be applied as an excellent light absorber for a photothermal water evaporation system. Using the b-Si sample by connected with the superhydrophilic porous sponge, we can achieve an average PTCE of 73% under 1 sun (AM 1.5G). The b-Si@SPS photothermal converter has an advanced PTCE compared with the latest reported photothermal conversion materials. It also presents

good stability during 10 cycle tests, which indicates a great potentially practical application. Furthermore, FDTD simulations are conducted to get a better understanding of the reflection results and the mechanism of how the electric field enhancement affects the light absorption.

Thirdly, we presented a b-Ag plasmonic absorber, which can harvest the incident light for wavelengths from 200 nm to 2500 nm and have an average absorptance of 99.4% in the whole solar spectrum. The b-Ag plasmonic absorber can be prepared by a scalable MS-ALD technique in a self-assemble manner. As-prepared b-Ag plasmonic absorber has plenty of uniformly distributed and hierarchical SiO_2 micro/nanostructures as support, where large amounts of random silver nanoparticles are attached. Their sizes range from several nanometers to dozens of nanometers. It is demonstrated that the strong LSPR hybridization of the adjacent silver nanoparticles and multiple scatterings lead to full solar spectrum absorption. The mask-free self-assembled fabrication method can also be applied to different solid substrates, enabling wide applications of solar energy harvesting. Moreover, the superior b-Ag with extremely high light absorption can be used for photo-thermoelectric power generation under the solar light irradiation. The voltage density (power rate) of assembled photo-thermoelectric convertor can achieve ~82.5 V m^{-2} (2.53 mW) under 1 sun intensity (100 mW cm^{-2}). Furthermore, we also test the tandem devices with 20 convertors at outdoor, the results also show good photo-thermoelectric conversion ability.

Fourth, we investigated large area (153 cm^2) 3D Ag@SiO_2 hybrid plasmonic nanostructures for photo-thermoelectric conversion. Experimental results indicate that 3D Ag@SiO_2 hybrid plasmonic nanostructures include random size distributions of Ag nanoparticles below 100 nm grown on hierarchically ordered branches on a trunk SiO_2. Adjustable reflection edges, transmission edges, and absorption edges are revealed in the prepared samples. The optimized sample shows an ultralow reflection of 0.5% and high absorption of 96.4% across the range from 200 to 2500 nm. The multiple forward

scattering and extinction effect produced by high (10.6 μm) Ag@SiO_2 nanostructures and Ag nanoparticles with random size distribution could be responsible for the tunable optical properties of reflection, transmission, and absorption. Furthermore, we use the 3 SC Ag@SiO_2 plasmonic nanostructure sample as the bottom-heated-based water evaporation light absorber and demonstrate it can significantly improve the evaporation rate to 7.12 times under 1 sun.

Fifth, an efficient strategy including dual interface engineering and photocatalyst deposition is put forward to improve the PEC performance of Si-based photocathode: the Si surface is nanostructured to enhance the light absorption, a TiO_2 layer is deposited as protective layer, and then ReS_2 nanosheets are grown as photocatalyst. In this strategy, the crystalline TiO_2 layer plays a key role for the largely enhanced PEC performance for water reduction. On one hand, TiO_2 and ReS_2 protect the photocathode from being corroded and improve its durability. On the other hand, b-Si/ReS_2 show a inferior performance due to the suppressed charge transfer kinetics by the flat band potential between electrode and electrolyte. However, by placing the 10 nm crystalline TiO_2 layer between b-Si and ReS_2, the band structure of the whole electrode becomes more favorable towards a reduced overpotential for the PEC and an improved charge transfer kinetics.

Based on these results, in the future works, the thermal conduction between the absorber and substrate should be carefully investigated, since it directly influences the solar conversion performance. We should develop high thermal conductivity absorbers for photo-thermoelectric conversion, while the support materials with poor thermal conductivity below absorbers should be applied, because heat localization retaining on the surface of absorbers can boost solar conversion efficiency. In addition, for PEC water reduction, the band alignment is critically significant and the related research methods, such as XPS valence spectra, UV-Vis spectra, should be carefully applied to study the band positions. After band alignment, the photocurrent density of

photocathode at 0 V vs. RHE should be as much as close to the saturated photocurrent density (~ 40 mA cm^{-2}).

Furthermore, fabrication methods with large-scale, controllable parameters and low cost are also highly needed to be applied for promoting the realistic applications of solar energy conversion, such as solar water evaporation, water purification, seawater desalination as well as photo-thermoelectric conversion. The developing novel absorbers with high broadband absorption, suitable heat conduction and low emission as the light absorbers are very significant for high photothermal conversion efficiency. In addition, efficiency and stability are the two most tough challenges for PEC water reduction. More efforts should be taken on the both to speed up its development. It can be expected that the further development and commercialization of the diverse photothermal technologies and high-efficiency PEC conversion technologies for solar energy conversion will play an important role and have big significance on global sustainability.

References

(1) Rabaia, M. K. H.; Abdelkareem, M. A.; Sayed, E. T.; Elsaid, K.; Chae, K.-J.; Wilberforce, T.; Olabi, A. G. Environmental Impacts of Solar Energy Systems: A Review. *Science of The Total Environment* **2021**, *754*, 141989. https://doi.org/10.1016/j.scitotenv.2020.141989.

(2) Kruitwagen, L.; Story, K. T.; Friedrich, J.; Byers, L.; Skillman, S.; Hepburn, C. A Global Inventory of Photovoltaic Solar Energy Generating Units. *Nature* **2021**, *598* (7882), 604–610. https://doi.org/10.1038/s41586-021-03957-7.

(3) Jin, L.; Zhao, H.; Wang, Z. M.; Rosei, F. Quantum Dots-Based Photoelectrochemical Hydrogen Evolution from Water Splitting. *Advanced Energy Materials* **2021**, *11* (12), 2003233. https://doi.org/10.1002/aenm.202003233.

(4) Grainger, A.; Smith, G. The Role of Low Carbon and High Carbon Materials in Carbon Neutrality Science and Carbon Economics. *Current Opinion in Environmental Sustainability* **2021**, *49*, 164–189. https://doi.org/10.1016/j.cosust.2021.06.006.

(5) Gorjian, S.; Sharon, H.; Ebadi, H.; Kant, K.; Scavo, F. B.; Tina, G. M. Recent Technical Advancements, Economics and Environmental Impacts of Floating Photovoltaic Solar Energy Conversion Systems. *Journal of Cleaner Production* **2021**, *278*, 124285. https://doi.org/10.1016/j.jclepro.2020.124285.

(6) Liu, C.; Kong, D.; Hsu, P.-C.; Yuan, H.; Lee, H.-W.; Liu, Y.; Wang, H.; Wang, S.; Yan, K.; Lin, D.; Maraccini, P. A.; Parker, K. M.; Boehm, A. B.; Cui, Y. Rapid Water Disinfection Using Vertically Aligned MoS2 Nanofilms and Visible Light. *Nature Nanotech* **2016**, *11* (12), 1098–1104. https://doi.org/10.1038/nnano.2016.138.

(7) Gong, J.; Li, C.; Wasielewski, M. R. Advances in Solar Energy Conversion. *Chem. Soc. Rev.* **2019**, *48* (7), 1862–1864. https://doi.org/10.1039/C9CS90020A.

(8) Yeom, H.; Sridharan, K. Cold Spray Technology in Nuclear Energy Applications: A Review of Recent Advances. *Annals of Nuclear Energy* **2021**, *150*, 107835. https://doi.org/10.1016/j.anucene.2020.107835.

(9) Johansen, K. Blowing in the Wind: A Brief History of Wind Energy and Wind Power Technologies in Denmark. *Energy Policy* **2021**, *152*, 112139. https://doi.org/10.1016/j.enpol.2021.112139.

(10) Zhang, C.; Zhou, L.; Cheng, P.; Liu, D.; Zhang, C.; Li, X.; Li, S.; Wang, J.; Wang, Z. L. Bifilar-Pendulum-Assisted Multilayer-Structured Triboelectric Nanogenerators for Wave Energy Harvesting. *Advanced Energy Materials* **2021**, *11* (12), 2003616. https://doi.org/10.1002/aenm.202003616.

(11) Peibst, R.; Rienäcker, M.; Larionova, Y.; Folchert, N.; Haase, F.; Hollemann, C.; Wolter, S.; Krügener, J.; Bayerl, P.; Bayer, J.; Dzinnik, M.; Haug, R. J.; Brendel, R. Towards 28 %-Efficient Si Single-Junction Solar Cells with Better Passivating POLO Junctions and Photonic Crystals. *Solar Energy Materials and Solar Cells* **2022**, *238*, 111560. https://doi.org/10.1016/j.solmat.2021.111560.

(12) Lin, L.; Jones, T. W.; Yang, T. C.-J.; Duffy, N. W.; Li, J.; Zhao, L.; Chi, B.; Wang, X.; Wilson, G. J. Inorganic Electron Transport Materials in Perovskite Solar Cells. *Advanced Functional Materials* **2021**, *31* (5), 2008300. https://doi.org/10.1002/adfm.202008300.

(13) Al-Ashouri, A.; Köhnen, E.; Li, B.; Magomedov, A.; Hempel, H.; Caprioglio, P.; Márquez, J. A.; Vilches, A. B. M.; Kasparavicius, E.; Smith, J. A.; Phung, N.; Menzel, D.; Grischek,

M.; Kegelmann, L.; Skroblin, D.; Gollwitzer, C.; Malinauskas, T.; Jošt, M.; Matič, G.; Rech, B.; Schlatmann, R.; Topič, M.; Korte, L.; Abate, A.; Stannowski, B.; Neher, D.; Stolterfoht, M.; Unold, T.; Getautis, V.; Albrecht, S. Monolithic Perovskite/Silicon Tandem Solar Cell with >29% Efficiency by Enhanced Hole Extraction. *Science* **2020**. https://doi.org/10.1126/science.abd4016.

(14) Gao, P.; Wang, P.; Liu, X.; Cui, Z.; Wu, Y.; Zhang, X.; Zhang, Q.; Wang, Z.; Zheng, Z.; Cheng, H.; Liu, Y.; Dai, Y.; Huang, B. Photothermal Synergy for Efficient Dry Reforming of CH4 by Ag/AgBr/CsPbBr3 Composite. *Catalysis Science & Technology* **2022**. https://doi.org/10.1039/D1CY02281D.

(15) Wang, S.; Yu, W.; Xu, S.; Han, K.; Wang, F. Ammonia from Photothermal N2 Hydrogenation over Ni/TiO2 Catalysts under Mild Conditions. *ACS Sustainable Chem. Eng.* **2022**, *10* (1), 115–123. https://doi.org/10.1021/acssuschemeng.1c04931.

(16) Mateo, D.; Luis Cerrillo, J.; Durini, S.; Gascon, J. Fundamentals and Applications of Photo-Thermal Catalysis. *Chemical Society Reviews* **2021**, *50* (3), 2173–2210. https://doi.org/10.1039/D0CS00357C.

(17) Ghoussoub, M.; Xia, M.; N. Duchesne, P.; Segal, D.; Ozin, G. Principles of Photothermal Gas-Phase Heterogeneous CO 2 Catalysis. *Energy & Environmental Science* **2019**, *12* (4), 1122–1142. https://doi.org/10.1039/C8EE02790K.

(18) Fan, W. K.; Tahir, M. Recent Developments in Photothermal Reactors with Understanding on the Role of Light/Heat for CO2 Hydrogenation to Fuels: A Review. *Chemical Engineering Journal* **2022**, *427*, 131617. https://doi.org/10.1016/j.cej.2021.131617.

(19) Zhu, L.; Gao, M.; Peh, C. K. N.; Ho, G. W. Recent Progress in Solar-Driven Interfacial Water Evaporation: Advanced Designs and Applications. *Nano Energy* **2019**, *57*, 507–518. https://doi.org/10.1016/j.nanoen.2018.12.046.

(20) Ren, H.; Tang, M.; Guan, B.; Wang, K.; Yang, J.; Wang, F.; Wang, M.; Shan, J.; Chen, Z.; Wei, D.; Peng, H.; Liu, Z. Hierarchical Graphene Foam for Efficient Omnidirectional Solar–Thermal Energy Conversion. *Advanced Materials* **2017**, *29* (38), 1702590. https://doi.org/10.1002/adma.201702590.

(21) Chen, Q.; Pei, Z.; Xu, Y.; Li, Z.; Yang, Y.; Wei, Y.; Ji, Y. A Durable Monolithic Polymer Foam for Efficient Solar Steam Generation. *Chem. Sci.* **2018**, *9* (3), 623–628. https://doi.org/10.1039/C7SC02967E.

(22) Shi, Y.; Li, R.; Jin, Y.; Zhuo, S.; Shi, L.; Chang, J.; Hong, S.; Ng, K.-C.; Wang, P. A 3D Photothermal Structure toward Improved Energy Efficiency in Solar Steam Generation. *Joule* **2018**, *2* (6), 1171–1186. https://doi.org/10.1016/j.joule.2018.03.013.

(23) Gao, M.; Zhu, L.; Kangnuo Peh, C.; Wei Ho, G. Solar Absorber Material and System Designs for Photothermal Water Vaporization towards Clean Water and Energy Production. *Energy & Environmental Science* **2019**, *12* (3), 841–864. https://doi.org/10.1039/C8EE01146J.

(24) Zhang, C.; Liang, H.-Q.; Xu, Z.-K.; Wang, Z. Harnessing Solar-Driven Photothermal Effect toward the Water–Energy Nexus. *Advanced Science* **2019**, *6* (18), 1900883. https://doi.org/10.1002/advs.201900883.

(25) Zhao, F.; Guo, Y.; Zhou, X.; Shi, W.; Yu, G. Materials for Solar-Powered Water Evaporation. *Nat Rev Mater* **2020**, *5* (5), 388–401. https://doi.org/10.1038/s41578-020-0182-4.

(26) Tao, P.; Ni, G.; Song, C.; Shang, W.; Wu, J.; Zhu, J.; Chen, G.; Deng, T. Solar-Driven

Interfacial Evaporation. *Nat Energy* **2018**, *3* (12), 1031–1041. https://doi.org/10.1038/s41560-018-0260-7.

(27) Zou, Y.; Zhang, Y.; Yu, Q.; Chen, H. Photothermal Bactericidal Surfaces: Killing Bacteria Using Light Instead of Biocides. *Biomaterials Science* **2021**, *9* (1), 10–22. https://doi.org/10.1039/D0BM00617C.

(28) Xiong, M.; Shan, X.; Liu, C.; Yang, L.; Meng, M.; Di, Y.; Gan, Z. Broadband Photodetectors Based on Enhanced Photothermal Effect of Polymer Encapsulated Graphene Film. *Applied Surface Science Advances* **2021**, *3*, 100050. https://doi.org/10.1016/j.apsadv.2020.100050.

(29) Xiang, H.; Niu, T.; Schoenauer Sebag, M.; Hu, Z.; Xu, X.; Billot, L.; Aigouy, L.; Chen, Z. Short-Wave Infrared Sensor by the Photothermal Effect of Colloidal Gold Nanorods. *Small* **2018**, *14* (16), 1704013. https://doi.org/10.1002/smll.201704013.

(30) Han, B.; Zhang, Y.-L.; Chen, Q.-D.; Sun, H.-B. Carbon-Based Photothermal Actuators. *Advanced Functional Materials* **2018**, *28* (40), 1802235. https://doi.org/10.1002/adfm.201802235.

(31) Zhou, L.; Tan, Y.; Wang, J.; Xu, W.; Yuan, Y.; Cai, W.; Zhu, S.; Zhu, J. 3D Self-Assembly of Aluminium Nanoparticles for Plasmon-Enhanced Solar Desalination. *Nature Photon* **2016**, *10* (6), 393–398. https://doi.org/10.1038/nphoton.2016.75.

(32) Chen, C.; Kuang, Y.; Hu, L. Challenges and Opportunities for Solar Evaporation. *Joule* **2019**, *3* (3), 683–718. https://doi.org/10.1016/j.joule.2018.12.023.

(33) Cheng, P.; Wang, H.; Müller, B.; Müller, J.; Wang, D.; Schaaf, P. Photo-Thermoelectric Conversion Using Black Silicon with Enhanced Light Trapping Performance Far beyond the Band Edge Absorption. *ACS Appl. Mater. Interfaces* **2021**, *13* (1), 1818–1826. https://doi.org/10.1021/acsami.0c17279.

(34) Wu, Z.; Li, C.; Li, Z.; Feng, K.; Cai, M.; Zhang, D.; Wang, S.; Chu, M.; Zhang, C.; Shen, J.; Huang, Z.; Xiao, Y.; Ozin, G. A.; Zhang, X.; He, L. Niobium and Titanium Carbides (MXenes) as Superior Photothermal Supports for CO2 Photocatalysis. *ACS Nano* **2021**, *15* (3), 5696–5705. https://doi.org/10.1021/acsnano.1c00990.

(35) Fan, W. K.; Tahir, M. Recent Developments in Photothermal Reactors with Understanding on the Role of Light/Heat for CO2 Hydrogenation to Fuels: A Review. *Chemical Engineering Journal* **2022**, *427*, 131617. https://doi.org/10.1016/j.cej.2021.131617.

(36) Luo, S.; Ren, X.; Lin, H.; Song, H.; Ye, J. Plasmonic Photothermal Catalysis for Solar-to-Fuel Conversion: Current Status and Prospects. *Chemical Science* **2021**, *12* (16), 5701–5719. https://doi.org/10.1039/D1SC00064K.

(37) Cheng, P.; Liu, Y.; Ziegler, M.; Klingenhof, M.; Wang, D.; Zhang, Z.; Strasser, P.; Schaaf, P. Improving Silicon Photocathode Performance for Water Reduction through Dual Interface Engineering and Integrating ReS2 Photocatalyst. *ACS Appl. Energy Mater.* **2022**. https://doi.org/10.1021/acsaem.2c00761.

(38) Cheng, P.; Wang, H.; Wang, H.; van Aken, P. A.; Wang, D.; Schaaf, P. High-Efficiency Photothermal Water Evaporation Using Broadband Solar Energy Harvesting by Ultrablack Silicon Structures. *Advanced Energy and Sustainability Research* **2021**, *2* (4), 2000083. https://doi.org/10.1002/aesr.202000083.

(39) Steglich, M.; Lehr, D.; Ratzsch, S.; Käsebier, T.; Schrempel, F.; Kley, E.-B.; Tünnermann, A. An Ultra-Black Silicon Absorber. *Laser & Photonics Reviews* **2014**, *8* (2), L13–L17. https://doi.org/10.1002/lpor.201300142.

(40) Zhou, L.; Tan, Y.; Ji, D.; Zhu, B.; Zhang, P.; Xu, J.; Gan, Q.; Yu, Z.; Zhu, J. Self-Assembly of Highly Efficient, Broadband Plasmonic Absorbers for Solar Steam Generation. *Science Advances* **2016**, *2* (4), e1501227. https://doi.org/10.1126/sciadv.1501227.

(41) Cheng, P.; Ziegler, M.; Ripka, V.; Wang, H.; Pollok, K.; Langenhorst, F.; Wang, D.; Schaaf, P. Black Silver: Three-Dimensional Ag Hybrid Plasmonic Nanostructures with Strong Photon Coupling for Scalable Photothermoelectric Power Generation. *ACS Appl. Mater. Interfaces* **2022**, *14* (14), 16894–16900. https://doi.org/10.1021/acsami.2c01181.

(42) Cheng, P.; Ziegler, M.; Ripka, V.; Wang, D.; Wang, H.; van Aken, P. A.; Schaaf, P. Bio-Inspired Self-Assembly of Large Area 3D Ag@SiO2 Plasmonic Nanostructures with Tunable Broadband Light Harvesting. *Applied Materials Today* **2021**, *25*, 101238. https://doi.org/10.1016/j.apmt.2021.101238.

(43) Li, M.; Han, N.; Zhang, X.; Wang, S.; Jiang, M.; Bokhari, A.; Zhang, W.; Race, M.; Shen, Z.; Chen, R.; Mubashir, M.; Khoo, K. S.; Teo, S. S.; Show, P. L. Perovskite Oxide for Emerging Photo(Electro)Catalysis in Energy and Environment. *Environmental Research* **2022**, *205*, 112544. https://doi.org/10.1016/j.envres.2021.112544.

(44) Che, X.; Zhu, B.; Wang, P. Assessing Global Energy Poverty: An Integrated Approach. *Energy Policy* **2021**, *149*, 112099. https://doi.org/10.1016/j.enpol.2020.112099.

(45) Min, H.; Lee, D. Y.; Kim, J.; Kim, G.; Lee, K. S.; Kim, J.; Paik, M. J.; Kim, Y. K.; Kim, K. S.; Kim, M. G.; Shin, T. J.; Il Seok, S. Perovskite Solar Cells with Atomically Coherent Interlayers on SnO2 Electrodes. *Nature* **2021**, *598* (7881), 444–450. https://doi.org/10.1038/s41586-021-03964-8.

(46) Chen, S.; Dai, X.; Xu, S.; Jiao, H.; Zhao, L.; Huang, J. Stabilizing Perovskite-Substrate Interfaces for High-Performance Perovskite Modules. *Science* **2021**. https://doi.org/10.1126/science.abi6323.

(47) Yoo, J. J.; Seo, G.; Chua, M. R.; Park, T. G.; Lu, Y.; Rotermund, F.; Kim, Y.-K.; Moon, C. S.; Jeon, N. J.; Correa-Baena, J.-P.; Bulović, V.; Shin, S. S.; Bawendi, M. G.; Seo, J. Efficient Perovskite Solar Cells via Improved Carrier Management. *Nature* **2021**, *590* (7847), 587–593. https://doi.org/10.1038/s41586-021-03285-w.

(48) Campbell, M. W.; Polites, V. C.; Patel, S.; Lipson, J. E.; Majhi, J.; Molander, G. A. Photochemical C–F Activation Enables Defluorinative Alkylation of Trifluoroacetates and -Acetamides. *J. Am. Chem. Soc.* **2021**, *143* (47), 19648–19654. https://doi.org/10.1021/jacs.1c11059.

(49) Genzink, M. J.; Kidd, J. B.; Swords, W. B.; Yoon, T. P. Chiral Photocatalyst Structures in Asymmetric Photochemical Synthesis. *Chem. Rev.* **2022**, *122* (2), 1654–1716. https://doi.org/10.1021/acs.chemrev.1c00467.

(50) Kusaka, R.; Nihonyanagi, S.; Tahara, T. The Photochemical Reaction of Phenol Becomes Ultrafast at the Air–Water Interface. *Nat. Chem.* **2021**, *13* (4), 306–311. https://doi.org/10.1038/s41557-020-00619-5.

(51) Mei, Z.; Chen, Y.; Tong, S.; Li, Y.; Liu, J.; Sun, L.; Zhong, W.; Dong, X.; Ji, Y.; Lin, Y.; Chen, H.; Pan, F. High-Performance Si Photocathode Enabled by Spatial Decoupling Multifunctional Layers for Water Splitting. *Advanced Functional Materials n/a* (n/a), 2107164. https://doi.org/10.1002/adfm.202107164.

(52) Tang, R.; Zhou, S.; Zhang, Z.; Zheng, R.; Huang, J. Engineering Nanostructure–Interface of Photoanode Materials Toward Photoelectrochemical Water Oxidation. *Advanced Materials*

2021, *33* (17), 2005389. https://doi.org/10.1002/adma.202005389.

(53) Zhang, X.; Zhai, P.; Zhang, Y.; Wu, Y.; Wang, C.; Ran, L.; Gao, J.; Li, Z.; Zhang, B.; Fan, Z.; Sun, L.; Hou, J. Engineering Single-Atomic Ni-N4-O Sites on Semiconductor Photoanodes for High-Performance Photoelectrochemical Water Splitting. *J. Am. Chem. Soc.* **2021**. https://doi.org/10.1021/jacs.1c07391.

(54) Xu, D.; Li, Z.; Li, L.; Wang, J. Insights into the Photothermal Conversion of 2D MXene Nanomaterials: Synthesis, Mechanism, and Applications. *Advanced Functional Materials* **2020**, *30* (47), 2000712. https://doi.org/10.1002/adfm.202000712.

(55) Zhu, L.; Gao, M.; Nuo Peh, C. K.; Wei Ho, G. Solar-Driven Photothermal Nanostructured Materials Designs and Prerequisites for Evaporation and Catalysis Applications. *Materials Horizons* **2018**, *5* (3), 323–343. https://doi.org/10.1039/C7MH01064H.

(56) Linic, S.; Aslam, U.; Boerigter, C.; Morabito, M. Photochemical Transformations on Plasmonic Metal Nanoparticles. *Nature Mater* **2015**, *14* (6), 567–576. https://doi.org/10.1038/nmat4281.

(57) Li, X.-M.; Bi, M.-H.; Cui, L.; Zhou, Y.-Z.; Du, X.-W.; Qiao, S.-Z.; Yang, J. 3D Aluminum Hybrid Plasmonic Nanostructures with Large Areas of Dense Hot Spots and Long-Term Stability. *Advanced Functional Materials* **2017**, *27* (10), 1605703. https://doi.org/10.1002/adfm.201605703.

(58) Wang, L.; Hasanzadeh Kafshgari, M.; Meunier, M. Optical Properties and Applications of Plasmonic-Metal Nanoparticles. *Advanced Functional Materials* **2020**, *30* (51), 2005400. https://doi.org/10.1002/adfm.202005400.

(59) Kelly, K. L.; Coronado, E.; Zhao, L. L.; Schatz, G. C. The Optical Properties of Metal Nanoparticles: The Influence of Size, Shape, and Dielectric Environment. *J. Phys. Chem. B* **2003**, *107* (3), 668–677. https://doi.org/10.1021/jp026731y.

(60) Jain, P. K.; Huang, X.; El-Sayed, I. H.; El-Sayed, M. A. Noble Metals on the Nanoscale: Optical and Photothermal Properties and Some Applications in Imaging, Sensing, Biology, and Medicine. *Acc. Chem. Res.* **2008**, *41* (12), 1578–1586. https://doi.org/10.1021/ar7002804.

(61) Huang, X.; Liu, J.; Zhou, P.; Su, G.; Zhou, T.; Zhang, X.; Zhang, C. Ultrarobust Photothermal Materials via Dynamic Crosslinking for Solar Harvesting. *Small n/a* (n/a), 2104048. https://doi.org/10.1002/smll.202104048.

(62) Zhang, Y.; Gurzadyan, G. G.; Umair, M. M.; Wang, W.; Lu, R.; Zhang, S.; Tang, B. Ultrafast and Efficient Photothermal Conversion for Sunlight-Driven Thermal-Electric System. *Chemical Engineering Journal* **2018**, *344*, 402–409. https://doi.org/10.1016/j.cej.2018.03.098.

(63) Zhu, L.; Ding, T.; Gao, M.; Peh, C. K. N.; Ho, G. W. Shape Conformal and Thermal Insulative Organic Solar Absorber Sponge for Photothermal Water Evaporation and Thermoelectric Power Generation. *Advanced Energy Materials* **2019**, *9* (22), 1900250. https://doi.org/10.1002/aenm.201900250.

(64) Chen, G.; Sun, J.; Peng, Q.; Sun, Q.; Wang, G.; Cai, Y.; Gu, X.; Shuai, Z.; Tang, B. Z. Biradical-Featured Stable Organic-Small-Molecule Photothermal Materials for Highly Efficient Solar-Driven Water Evaporation. *Advanced Materials* **2020**, *32* (29), 1908537. https://doi.org/10.1002/adma.201908537.

(65) Chen, G.; Jiang, Z.; Li, A.; Chen, X.; Ma, Z.; Song, H. Cu-Based MOF-Derived Porous

Carbon with Highly Efficient Photothermal Conversion Performance for Solar Steam Evaporation. *Journal of Materials Chemistry A* **2021**, *9* (31), 16805–16813. https://doi.org/10.1039/D1TA03695E.

(66) Cao, P.; Zhao, L.; Zhang, J.; Zhang, L.; Yuan, P.; Zhang, Y.; Li, Q. Gradient Heating Effect Modulated by Hydrophobic/Hydrophilic Carbon Nanotube Network Structures for Ultrafast Solar Steam Generation. *ACS Appl. Mater. Interfaces* **2021**, *13* (16), 19109–19116. https://doi.org/10.1021/acsami.0c21831.

(67) Duan, Y.; Weng, M.; Zhang, W.; Qian, Y.; Luo, Z.; Chen, L. Multi-Functional Carbon Nanotube Paper for Solar Water Evaporation Combined with Electricity Generation and Storage. *Energy Conversion and Management* **2021**, *241*, 114306. https://doi.org/10.1016/j.enconman.2021.114306.

(68) He, W.; Zhou, L.; Wang, M.; Cao, Y.; Chen, X.; Hou, X. Structure Development of Carbon-Based Solar-Driven Water Evaporation Systems. *Science Bulletin* **2021**, *66* (14), 1472–1483. https://doi.org/10.1016/j.scib.2021.02.014.

(69) Lova, P.; Robbiano, V.; Cacialli, F.; Comoretto, D.; Soci, C. Black GaAs by Metal-Assisted Chemical Etching. *ACS Appl. Mater. Interfaces* **2018**, *10* (39), 33434–33440. https://doi.org/10.1021/acsami.8b10370.

(70) Huang, X.; Liu, J.; Zhou, P.; Su, G.; Zhou, T.; Zhang, X.; Zhang, C. Ultrarobust Photothermal Materials via Dynamic Crosslinking for Solar Harvesting. *Small* **2022**, *18* (7), 2104048. https://doi.org/10.1002/smll.202104048.

(71) Zhang, Z.; Wang, Y.; Stensby Hansen, P. A.; Du, K.; Gustavsen, K. R.; Liu, G.; Karlsen, F.; Nilsen, O.; Xue, C.; Wang, K. Black Silicon with Order-Disordered Structures for Enhanced Light Trapping and Photothermic Conversion. *Nano Energy* **2019**, *65*, 103992. https://doi.org/10.1016/j.nanoen.2019.103992.

(72) Li, R.; Zhang, L.; Shi, L.; Wang, P. MXene Ti3C2: An Effective 2D Light-to-Heat Conversion Material. *ACS Nano* **2017**, *11* (4), 3752–3759. https://doi.org/10.1021/acsnano.6b08415.

(73) Fujishima, A.; Honda, K. Electrochemical Photolysis of Water at a Semiconductor Electrode. *Nature* **1972**, *238* (5358), 37–38. https://doi.org/10.1038/238037a0.

(74) Joy, J.; Mathew, J.; George, S. C. Nanomaterials for Photoelectrochemical Water Splitting – Review. *International Journal of Hydrogen Energy* **2018**, *43* (10), 4804–4817. https://doi.org/10.1016/j.ijhydene.2018.01.099.

(75) Kong, D. Y.; Cho, C. S.; Jo, J. H.; Kim, B. H.; Lee, J. H. Surface Texturing for Crystalline Silicon Solar Cell Using RIE Equipped with Metal-Mesh. *AMR* **2011**, *328–330*, 747–750. https://doi.org/10.4028/www.scientific.net/AMR.328-330.747.

(76) Liu, Y.; Li, J.; Huang, W.; Zhang, Y.; Wang, M.; Gao, X.; Wang, X.; Jin, M.; Hou, Z.; Zhou, G.; Zhang, Z.; Liu, J. Surface-Induced 2D/1D Heterostructured Growth of ReS2/CoS2 for High-Performance Electrocatalysts. *ACS Appl. Mater. Interfaces* **2020**, *12* (30), 33586–33594. https://doi.org/10.1021/acsami.0c02951.

(77) Huang, W.; Zhou, Q.; Su, S.; Li, J.; Lu, X.; Gao, X.; Wang, X.; Jin, M.; Zhou, G.; Zhang, Z.; Liu, J. Ion Beam Defect Engineering on ReS2/Si Photocathode with Significantly Enhanced Hydrogen Evolution Reaction. *Advanced Materials Interfaces* **2019**, *6* (3), 1801663. https://doi.org/10.1002/admi.201801663.

(78) Ziegler, M.; Dathe, A.; Pollok, K.; Langenhorst, F.; Hübner, U.; Wang, D.; Schaaf, P.

Metastable Atomic Layer Deposition: 3D Self-Assembly toward Ultradark Materials. *ACS Nano* **2020**, *14* (11), 15023–15031. https://doi.org/10.1021/acsnano.0c04974.

(79) Ziegler, M.; Yüksel, S.; Goerke, S.; Weber, K.; Cialla-May, D.; Popp, J.; Pollok, K.; Wang, D.; Langenhorst, F.; Hübner, U.; Schaaf, P.; Meyer, H.-G. Growth of Hierarchically 3D Silver–Silica Hybrid Nanostructures by Metastable State Assisted Atomic Layer Deposition (MS-ALD). *Advanced Materials Technologies* **2017**, *2* (7), 1700015. https://doi.org/10.1002/admt.201700015.

(80) Spieß, L.; Teichert, G.; Schwarzer, R.; Behnken, H.; Genzel, C. *Moderne Röntgenbeugung: Röntgendiffraktometrie für Materialwissenschaftler, Physiker und Chemiker*; Springer Fachmedien Wiesbaden: Wiesbaden, 2009. https://doi.org/10.1007/978-3-8348-8232-5.

(81) Wang, L.; Liu, W.; Tang, J.-W.; Wang, J.-J.; Liu, Q.-H.; Wen, P.-B.; Wang, M.-M.; Pan, Y.-C.; Gu, B.; Zhang, X. Applications of Raman Spectroscopy in Bacterial Infections: Principles, Advantages, and Shortcomings. *Front Microbiol* **2021**, *12*, 683580. https://doi.org/10.3389/fmicb.2021.683580.

(82) John, F. M.; William, F. S.; Peter, E. S.; Kenneth, D. B. *Handbook of X-Ray Photoelectron Spectroscopy*; Perkin-Elmer Corporation: Physical Electronics Division, 1992; Vol. 40.

(83) Zhong, M.; Jang, M. Light Absorption Coefficient Measurement of SOA Using a UV–Visible Spectrometer Connected with an Integrating Sphere. *Atmospheric Environment* **2011**, *45* (25), 4263–4271. https://doi.org/10.1016/j.atmosenv.2011.04.082.

(84) Kim, S.-K.; Day, R. W.; Cahoon, J. F.; Kempa, T. J.; Song, K.-D.; Park, H.-G.; Lieber, C. M. Tuning Light Absorption in Core/Shell Silicon Nanowire Photovoltaic Devices through Morphological Design. *Nano Lett.* **2012**, *12* (9), 4971–4976. https://doi.org/10.1021/nl302578z.

(85) Palik, E. D. *Handbook of Optical Constants of Solids*; Academic Press, 1998.

(86) Gao, X.-Y.; Feng, H.-L.; Ma, J.-M.; Zhang, Z.-Y.; Lu, J.-X.; Chen, Y.-S.; Yang, S.-E.; Gu, J.-H. Analysis of the Dielectric Constants of the Ag2O Film by Spectroscopic Ellipsometry and Single-Oscillator Model. *Physica B: Condensed Matter* **2010**, *405* (7), 1922–1926. https://doi.org/10.1016/j.physb.2010.01.076.

(87) Zheng, J.; Lyu, Y.; Wang, R.; Xie, C.; Zhou, H.; Jiang, S. P.; Wang, S. Crystalline TiO 2 Protective Layer with Graded Oxygen Defects for Efficient and Stable Silicon-Based Photocathode. *Nature Communications* **2018**, *9* (1), 3572. https://doi.org/10.1038/s41467-018-05580-z.

(88) Fan, R.; Mao, J.; Yin, Z.; Jie, J.; Dong, W.; Fang, L.; Zheng, F.; Shen, M. Efficient and Stable Silicon Photocathodes Coated with Vertically Standing Nano-MoS2 Films for Solar Hydrogen Production. *ACS Appl. Mater. Interfaces* **2017**, *9* (7), 6123–6129. https://doi.org/10.1021/acsami.6b15854.

(89) Vijselaar, W.; Westerik, P.; Veerbeek, J.; Tiggelaar, R. M.; Berenschot, E.; Tas, N. R.; Gardeniers, H.; Huskens, J. Spatial Decoupling of Light Absorption and Catalytic Activity of Ni–Mo-Loaded High-Aspect-Ratio Silicon Microwire Photocathodes. *Nat Energy* **2018**, *3* (3), 185–192. https://doi.org/10.1038/s41560-017-0068-x.

(90) Ghoussoub, M.; Xia, M.; N. Duchesne, P.; Segal, D.; Ozin, G. Principles of Photothermal Gas-Phase Heterogeneous CO 2 Catalysis. *Energy & Environmental Science* **2019**, *12* (4), 1122–1142. https://doi.org/10.1039/C8EE02790K.

(91) Sun, L.; Chen, Y.; Gong, F.; Dang, Q.; Xiang, G.; Cheng, L.; Liao, F.; Shao, M. Silicon

Nanowires Decorated with Gold Nanoparticles via in Situ Reduction for Photoacoustic Imaging-Guided Photothermal Cancer Therapy. *Journal of Materials Chemistry B* **2019**, *7* (28), 4393–4401. https://doi.org/10.1039/C9TB00147F.

(92) Steglich, M.; Käsebier, T.; Zilk, M.; Pertsch, T.; Kley, E.-B.; Tünnermann, A. The Structural and Optical Properties of Black Silicon by Inductively Coupled Plasma Reactive Ion Etching. *Journal of Applied Physics* **2014**, *116* (17), 173503. https://doi.org/10.1063/1.4900996.

(93) Noor, N. A. Md.; Mohamad, S. K.; Hamil, S. S.; Devarajan, M.; Pakhuruddin, M. Z. Effects of Etching Time towards Broadband Absorption Enhancement in Black Silicon Fabricated by Silver-Assisted Chemical Etching. *Optik* **2019**, *176*, 586–592. https://doi.org/10.1016/j.ijleo.2018.09.096.

(94) Plakhotnyuk, M. M.; Gaudig, M.; Davidsen, R. S.; Lindhard, J. M.; Hirsch, J.; Lausch, D.; Schmidt, M. S.; Stamate, E.; Hansen, O. Low Surface Damage Dry Etched Black Silicon. *Journal of Applied Physics* **2017**, *122* (14), 143101. https://doi.org/10.1063/1.4993425.

(95) Hu, D.; Xiang, J.; Zhou, Q.; Su, S.; Zhang, Z.; Wang, X.; Jin, M.; Nian, L.; Nözel, R.; Zhou, G.; Zhang, Z.; Liu, J. One-Step Chemical Vapor Deposition of MoS 2 Nanosheets on SiNWs as Photocathodes for Efficient and Stable Solar-Driven Hydrogen Production. *Nanoscale* **2018**, *10* (7), 3518–3525. https://doi.org/10.1039/C7NR09235K.

(96) Azeredo, B. P.; Lin, Y.-W.; Avagyan, A.; Sivaguru, M.; Hsu, K.; Ferreira, P. Direct Imprinting of Porous Silicon via Metal-Assisted Chemical Etching. *Advanced Functional Materials* **2016**, *26* (17), 2929–2939. https://doi.org/10.1002/adfm.201505153.

(97) Lai, R. A.; Hymel, T. M.; Narasimhan, V. K.; Cui, Y. Schottky Barrier Catalysis Mechanism in Metal-Assisted Chemical Etching of Silicon. *ACS Appl. Mater. Interfaces* **2016**, *8* (14), 8875–8879. https://doi.org/10.1021/acsami.6b01020.

(98) Kong, L.; Chiam, S. Y.; Chim, W. K. Metal-Assisted Silicon Chemical Etching Using Self-Assembled Sacrificial Nickel Nanoparticles Template for Antireflection Layers in Photovoltaic and Light-Trapping Devices. *ACS Appl. Nano Mater.* **2019**, *2* (11), 7025–7031. https://doi.org/10.1021/acsanm.9b01528.

(99) Wang, D.; Ji, R.; Du, S.; Albrecht, A.; Schaaf, P. Ordered Arrays of Nanoporous Silicon Nanopillars and Silicon Nanopillars with Nanoporous Shells. *Nanoscale Res Lett* **2013**, *8* (1), 42. https://doi.org/10.1186/1556-276X-8-42.

(100) Wang, D.; Schönherr, S.; Du, S.; Ronning, C.; Schaaf, P. Luminescent Ordered Arrays of Nanoporous Silicon Nanopillars and Silicon Nanopillars with Nanoporous Shells. *Materials Letters* **2013**, *98*, 186–189. https://doi.org/10.1016/j.matlet.2013.02.044.

(101) Liu, X.; R. Coxon, P.; Peters, M.; Hoex, B.; M. Cole, J.; J. Fray, D. Black Silicon: Fabrication Methods, Properties and Solar Energy Applications. *Energy & Environmental Science* **2014**, *7* (10), 3223–3263. https://doi.org/10.1039/C4EE01152J.

(102) Xu, G. J.; Cheng, S. Q.; Cai, B. *Black silicon as absorber for photo-thermal-electric devices*. https://doi.org/info:doi/10.1166/mex.2018.1426.

(103) Yu, X.; Yang, K.; Chen, X.; Li, W. Black Hollow Silicon Oxide Nanoparticles as Highly Efficient Photothermal Agents in the Second Near-Infrared Window for in Vivo Cancer Therapy. *Biomaterials* **2017**, *143*, 120–129. https://doi.org/10.1016/j.biomaterials.2017.07.037.

(104) Xu, W.; Tamarov, K.; Fan, L.; Granroth, S.; Rantanen, J.; Nissinen, T.; Peräniemi, S.; Uski, O.; Hirvonen, M.-R.; Lehto, V.-P. Scalable Synthesis of Biodegradable Black Mesoporous

Silicon Nanoparticles for Highly Efficient Photothermal Therapy. *ACS Appl. Mater. Interfaces* **2018**, *10* (28), 23529–23538. https://doi.org/10.1021/acsami.8b04557.

(105) Branz, H. M.; Yost, V. E.; Ward, S.; Jones, K. M.; To, B.; Stradins, P. Nanostructured Black Silicon and the Optical Reflectance of Graded-Density Surfaces. *Appl. Phys. Lett.* **2009**, *94* (23), 231121. https://doi.org/10.1063/1.3152244.

(106) Mellhaoui, X.; Dussart, R.; Tillocher, T.; Lefaucheux, P.; Ranson, P.; Boufnichel, M.; Overzet, L. J. SiOxFy Passivation Layer in Silicon Cryoetching. *Journal of Applied Physics* **2005**, *98* (10), 104901. https://doi.org/10.1063/1.2133896.

(107) Jansen, H.; Boer, M. de; Legtenberg, R.; Elwenspoek, M. The Black Silicon Method: A Universal Method for Determining the Parameter Setting of a Fluorine-Based Reactive Ion Etcher in Deep Silicon Trench Etching with Profile Control. *J. Micromech. Microeng.* **1995**, *5* (2), 115–120. https://doi.org/10.1088/0960-1317/5/2/015.

(108) Nguyen, K. N.; Basset, P.; Marty, F.; Leprince-Wang, Y.; Bourouina, T. On the Optical and Morphological Properties of Microstructured Black Silicon Obtained by Cryogenic-Enhanced Plasma Reactive Ion Etching. *Journal of Applied Physics* **2013**, *113* (19), 194903. https://doi.org/10.1063/1.4805024.

(109) Yamada, N.; Kim, O. N.; Tokimitsu, T.; Nakai, Y.; Masuda, H. Optimization of Anti-Reflection Moth-Eye Structures for Use in Crystalline Silicon Solar Cells. *Progress in Photovoltaics: Research and Applications* **2011**, *19* (2), 134–140. https://doi.org/10.1002/pip.994.

(110) Boden, S. A.; Bagnall, D. M. Optimization of Moth-Eye Antireflection Schemes for Silicon Solar Cells. *Progress in Photovoltaics: Research and Applications* **2010**, *18* (3), 195–203. https://doi.org/10.1002/pip.951.

(111) Murias, D.; Reyes-Betanzo, C.; Moreno, M.; Torres, A.; Itzmoyotl, A.; Ambrosio, R.; Soriano, M.; Lucas, J.; Cabarrocas, P. R. i. Black Silicon Formation Using Dry Etching for Solar Cells Applications. *Materials Science and Engineering: B* **2012**, *177* (16), 1509–1513. https://doi.org/10.1016/j.mseb.2012.03.038.

(112) Zhao, S.; Yuan, G.; Wang, Q.; Liu, W.; Wang, R.; Yang, S. Quasi-Hydrophilic Black Silicon Photocathodes with Inverted Pyramid Arrays for Enhanced Hydrogen Generation. *Nanoscale* **2020**, *12* (1), 316–325. https://doi.org/10.1039/C9NR06635G.

(113) Huang, Y.-F.; Chattopadhyay, S.; Jen, Y.-J.; Peng, C.-Y.; Liu, T.-A.; Hsu, Y.-K.; Pan, C.-L.; Lo, H.-C.; Hsu, C.-H.; Chang, Y.-H.; Lee, C.-S.; Chen, K.-H.; Chen, L.-C. Improved Broadband and Quasi-Omnidirectional Anti-Reflection Properties with Biomimetic Silicon Nanostructures. *Nature Nanotechnology* **2007**, *2* (12), 770–774. https://doi.org/10.1038/nnano.2007.389.

(114) Baker-Finch, S. C.; McIntosh, K. R.; Yan, D.; Fong, K. C.; Kho, T. C. Near-Infrared Free Carrier Absorption in Heavily Doped Silicon. *Journal of Applied Physics* **2014**, *116* (6), 063106. https://doi.org/10.1063/1.4893176.

(115) Wang, J.; Li, Y.; Deng, L.; Wei, N.; Weng, Y.; Dong, S.; Qi, D.; Qiu, J.; Chen, X.; Wu, T. High-Performance Photothermal Conversion of Narrow-Bandgap Ti2O3 Nanoparticles. *Advanced Materials* **2017**, *29* (3), 1603730. https://doi.org/10.1002/adma.201603730.

(116) Davis, A. L.; Nijhout, H. F.; Johnsen, S. Diverse Nanostructures Underlie Thin Ultra-Black Scales in Butterflies. *Nature Communications* **2020**, *11* (1), 1294. https://doi.org/10.1038/s41467-020-15033-1.

(117) Guo, J.; Li, D.; Qian, Z.; Luo, H.; Yang, M.; Wang, Q.; Xu, J.; Zhao, N. Carbon Vesicles: A Symmetry-Breaking Strategy for Wide-Band and Solvent-Processable Ultrablack Coating Materials. *Advanced Functional Materials* **2020**, *30* (17), 1909877. https://doi.org/10.1002/adfm.201909877.

(118) Wang, H.; Du, A.; Ji, X.; Zhang, C.; Zhou, B.; Zhang, Z.; Shen, J. Enhanced Photothermal Conversion by Hot-Electron Effect in Ultrablack Carbon Aerogel for Solar Steam Generation. *ACS Appl. Mater. Interfaces* **2019**, *11* (45), 42057–42065. https://doi.org/10.1021/acsami.9b12918.

(119) Zhu, L.; Ding, T.; Gao, M.; Peh, C. K. N.; Ho, G. W. Shape Conformal and Thermal Insulative Organic Solar Absorber Sponge for Photothermal Water Evaporation and Thermoelectric Power Generation. *Advanced Energy Materials* **2019**, *9* (22), 1900250. https://doi.org/10.1002/aenm.201900250.

(120) Won Heo, S.; Le, T. H. H.; Tanaka, T.; Osaka, I.; Takimiya, K.; Tajima, K. Cumulative Gain in Organic Solar Cells by Using Multiple Optical Nanopatterns. *Journal of Materials Chemistry A* **2017**, *5* (21), 10347–10354. https://doi.org/10.1039/C7TA01897E.

(121) Wiscombe, W. J. Improved Mie Scattering Algorithms. *Appl. Opt., AO* **1980**, *19* (9), 1505–1509. https://doi.org/10.1364/AO.19.001505.

(122) Cho, S.; Shim, T. S.; Kim, J. H.; Kim, D.-H.; Kim, S.-H. Selective Coloration of Melanin Nanospheres through Resonant Mie Scattering. *Advanced Materials* **2017**, *29* (22), 1700256. https://doi.org/10.1002/adma.201700256.

(123) Terekhov, P. D.; Baryshnikova, K. V.; Shalin, A. S.; Karabchevsky, A.; Evlyukhin, A. B. Resonant Forward Scattering of Light by High-Refractive-Index Dielectric Nanoparticles with Toroidal Dipole Contribution. *Opt. Lett., OL* **2017**, *42* (4), 835–838. https://doi.org/10.1364/OL.42.000835.

(124) Wang, Y.; Schouten, H. F.; Visser, T. D. Strong Suppression of Forward or Backward Mie Scattering by Using Spatial Coherence. *J. Opt. Soc. Am. A, JOSAA* **2016**, *33* (4), 513–518. https://doi.org/10.1364/JOSAA.33.000513.

(125) Lv, J.; Zhang, T.; Zhang, P.; Zhao, Y.; Li, S. Review Application of Nanostructured Black Silicon. *Nanoscale Research Letters* **2018**, *13* (1), 110. https://doi.org/10.1186/s11671-018-2523-4.

(126) Li, C.; Zhao, J.; Yu, X.; Chen, Q.; Feng, J.; Sun, H. Fabrication of Black Silicon With Thermostable Infrared Absorption by Femtosecond Laser. *IEEE Photonics Journal* **2016**, *8* (6), 1–9. https://doi.org/10.1109/JPHOT.2016.2617403.

(127) Tembhurne, S.; Nandjou, F.; Haussener, S. A Thermally Synergistic Photo-Electrochemical Hydrogen Generator Operating under Concentrated Solar Irradiation. *Nat Energy* **2019**, *4* (5), 399–407. https://doi.org/10.1038/s41560-019-0373-7.

(128) Goto, Y.; Hisatomi, T.; Wang, Q.; Higashi, T.; Ishikiriyama, K.; Maeda, T.; Sakata, Y.; Okunaka, S.; Tokudome, H.; Katayama, M.; Akiyama, S.; Nishiyama, H.; Inoue, Y.; Takewaki, T.; Setoyama, T.; Minegishi, T.; Takata, T.; Yamada, T.; Domen, K. A Particulate Photocatalyst Water-Splitting Panel for Large-Scale Solar Hydrogen Generation. *Joule* **2018**, *2* (3), 509–520. https://doi.org/10.1016/j.joule.2017.12.009.

(129) Wang, Y.; Dar, M. I.; Ono, L. K.; Zhang, T.; Kan, M.; Li, Y.; Zhang, L.; Wang, X.; Yang, Y.; Gao, X.; Qi, Y.; Grätzel, M.; Zhao, Y. Thermodynamically Stabilized β-CsPbI3–Based Perovskite Solar Cells with Efficiencies >18%. *Science* **2019**, *365* (6453), 591–595.

https://doi.org/10.1126/science.aav8680.

(130) Tavakoli, M. M.; Saliba, M.; Yadav, P.; Holzhey, P.; Hagfeldt, A.; Zakeeruddin, S. M.; Grätzel, M. Synergistic Crystal and Interface Engineering for Efficient and Stable Perovskite Photovoltaics. *Advanced Energy Materials* **2019**, *9* (1), 1802646. https://doi.org/10.1002/aenm.201802646.

(131) Cushing, S. K.; Porter, I. J.; Roulet, B. R. de; Lee, A.; Marsh, B. M.; Szoke, S.; Vaida, M. E.; Leone, S. R. Layer-Resolved Ultrafast Extreme Ultraviolet Measurement of Hole Transport in a Ni-TiO2-Si Photoanode. *Science Advances* **2020**, *6* (14), eaay6650. https://doi.org/10.1126/sciadv.aay6650.

(132) Wang, W.; Guo, B.; Dai, H.; Zhao, C.; Xie, G.; Ma, R.; Akram, M. Z.; Shan, H.; Cai, C.; Fang, Z.; Gong, J. R. Improving the Water Oxidation Efficiency with a Light-Induced Electric Field in Nanograting Photoanodes. *Nano Lett.* **2019**, *19* (9), 6133–6139. https://doi.org/10.1021/acs.nanolett.9b02122.

(133) Wang, Q.; Nakabayashi, M.; Hisatomi, T.; Sun, S.; Akiyama, S.; Wang, Z.; Pan, Z.; Xiao, X.; Watanabe, T.; Yamada, T.; Shibata, N.; Takata, T.; Domen, K. Oxysulfide Photocatalyst for Visible-Light-Driven Overall Water Splitting. *Nat. Mater.* **2019**, *18* (8), 827–832. https://doi.org/10.1038/s41563-019-0399-z.

(134) Gao, M.; Peh, C. K.; Zhu, L.; Yilmaz, G.; Ho, G. W. Photothermal Catalytic Gel Featuring Spectral and Thermal Management for Parallel Freshwater and Hydrogen Production. *Advanced Energy Materials* **2020**, *10* (23), 2000925. https://doi.org/10.1002/aenm.202000925.

(135) Meng, F. L.; Gao, M.; Ding, T.; Yilmaz, G.; Ong, W. L.; Ho, G. W. Modular Deformable Steam Electricity Cogeneration System with Photothermal, Water, and Electrochemical Tunable Multilayers. *Advanced Functional Materials* **2020**, *30* (32), 2002867. https://doi.org/10.1002/adfm.202002867.

(136) Wang, X.; Peng, K.-Q.; Pan, X.-J.; Chen, X.; Yang, Y.; Li, L.; Meng, X.-M.; Zhang, W.-J.; Lee, S.-T. High-Performance Silicon Nanowire Array Photoelectrochemical Solar Cells through Surface Passivation and Modification. *Angewandte Chemie* **2011**, *123* (42), 10035–10039. https://doi.org/10.1002/ange.201104102.

(137) Turren-Cruz, S.-H.; Saliba, M.; T. Mayer, M.; Juárez-Santiesteban, H.; Mathew, X.; Nienhaus, L.; Tress, W.; P. Erodici, M.; Sher, M.-J.; G. Bawendi, M.; Grätzel, M.; Abate, A.; Hagfeldt, A.; Correa-Baena, J.-P. Enhanced Charge Carrier Mobility and Lifetime Suppress Hysteresis and Improve Efficiency in Planar Perovskite Solar Cells. *Energy & Environmental Science* **2018**, *11* (1), 78–86. https://doi.org/10.1039/C7EE02901B.

(138) Shao, S.; Liu, J.; Portale, G.; Fang, H.-H.; Blake, G. R.; Brink, G. H. ten; Koster, L. J. A.; Loi, M. A. Highly Reproducible Sn-Based Hybrid Perovskite Solar Cells with 9% Efficiency. *Advanced Energy Materials* **2018**, *8* (4), 1702019. https://doi.org/10.1002/aenm.201702019.

(139) Arora, N.; Dar, M. I.; Hinderhofer, A.; Pellet, N.; Schreiber, F.; Zakeeruddin, S. M.; Grätzel, M. Perovskite Solar Cells with CuSCN Hole Extraction Layers Yield Stabilized Efficiencies Greater than 20%. *Science* **2017**, *358* (6364), 768–771. https://doi.org/10.1126/science.aam5655.

(140) Vijselaar, W.; Kunturu, P. P.; Moehl, T.; Tilley, S. D.; Huskens, J. Tandem Cuprous Oxide/Silicon Microwire Hydrogen-Evolving Photocathode with Photovoltage Exceeding 1.3 V. *ACS Energy Lett.* **2019**, *4* (9), 2287–2294.

https://doi.org/10.1021/acsenergylett.9b01402.

(141) Wu, X.; Robson, M. E.; Phelps, J. L.; Tan, J. S.; Shao, B.; Owens, G.; Xu, H. A Flexible Photothermal Cotton-CuS Nanocage-Agarose Aerogel towards Portable Solar Steam Generation. *Nano Energy* **2019**, *56*, 708–715. https://doi.org/10.1016/j.nanoen.2018.12.008.

(142) Wang, Y.; Zhu, W.; Du, W.; Liu, X.; Zhang, X.; Dong, H.; Hu, W. Cocrystals Strategy towards Materials for Near-Infrared Photothermal Conversion and Imaging. *Angewandte Chemie International Edition* **2018**, *57* (15), 3963–3967. https://doi.org/10.1002/anie.201712949.

(143) Zou, Y.; Wu, T.; Li, N.; Guo, X.; Li, Y. Photothermal-Enhanced Synthetic Melanin Inks for near-Infrared Imaging. *Polymer* **2020**, *186*, 122042. https://doi.org/10.1016/j.polymer.2019.122042.

(144) Li, Y.; Gao, T.; Yang, Z.; Chen, C.; Kuang, Y.; Song, J.; Jia, C.; Hitz, E. M.; Yang, B.; Hu, L. Graphene Oxide-Based Evaporator with One-Dimensional Water Transport Enabling High-Efficiency Solar Desalination. *Nano Energy* **2017**, *41*, 201–209. https://doi.org/10.1016/j.nanoen.2017.09.034.

(145) Zhou, Y.; Ding, T.; Gao, M.; Chan, K. H.; Cheng, Y.; He, J.; Ho, G. W. Controlled Heterogeneous Water Distribution and Evaporation towards Enhanced Photothermal Water-Electricity-Hydrogen Production. *Nano Energy* **2020**, *77*, 105102. https://doi.org/10.1016/j.nanoen.2020.105102.

(146) Tao, P.; Ni, G.; Song, C.; Shang, W.; Wu, J.; Zhu, J.; Chen, G.; Deng, T. Solar-Driven Interfacial Evaporation. *Nat Energy* **2018**, *3* (12), 1031–1041. https://doi.org/10.1038/s41560-018-0260-7.

(147) Gao, M.; Zhu, L.; Kangnuo Peh, C.; Wei Ho, G. Solar Absorber Material and System Designs for Photothermal Water Vaporization towards Clean Water and Energy Production. *Energy & Environmental Science* **2019**, *12* (3), 841–864. https://doi.org/10.1039/C8EE01146J.

(148) Hu, X.; Xu, W.; Zhou, L.; Tan, Y.; Wang, Y.; Zhu, S.; Zhu, J. Tailoring Graphene Oxide-Based Aerogels for Efficient Solar Steam Generation under One Sun. *Advanced Materials* **2017**, *29* (5), 1604031. https://doi.org/10.1002/adma.201604031.

(149) Ma, C.; Yan, J.; Huang, Y.; Wang, C.; Yang, G. The Optical Duality of Tellurium Nanoparticles for Broadband Solar Energy Harvesting and Efficient Photothermal Conversion. *Science Advances* **2018**, *4* (8), eaas9894. https://doi.org/10.1126/sciadv.aas9894.

(150) Yang, Y.; Zhao, R.; Zhang, T.; Zhao, K.; Xiao, P.; Ma, Y.; Ajayan, P. M.; Shi, G.; Chen, Y. Graphene-Based Standalone Solar Energy Converter for Water Desalination and Purification. *ACS Nano* **2018**, *12* (1), 829–835. https://doi.org/10.1021/acsnano.7b08196.

(151) Cheng, P.; Wang, H.; Müller, B.; Müller, J.; Wang, D.; Schaaf, P. Photo-Thermoelectric Conversion Using Black Silicon with Enhanced Light Trapping Performance Far beyond the Band Edge Absorption. *ACS Appl. Mater. Interfaces* **2021**. https://doi.org/10.1021/acsami.0c17279.

(152) Moatti, A.; Bayati, R.; Narayan, J. Epitaxial Growth of Rutile TiO2 Thin Films by Oxidation of TiN/Si{100} Heterostructure. *Acta Materialia* **2016**, *103*, 502–511. https://doi.org/10.1016/j.actamat.2015.10.022.

(153) Wang, M.; Wang, D.; Schaaf, P. Layer Thickness Effect on Fracture Behavior of Al/Si3N4

Multilayer on Si Substrate under Three-Point Bending. *Applied Surface Science* **2018**, *445*, 563–567. https://doi.org/10.1016/j.apsusc.2018.02.223.

(154) Adu, K. W.; Gutiérrez, H. R.; Kim, U. J.; Sumanasekera, G. U.; Eklund, P. C. Confined Phonons in Si Nanowires. *Nano Lett.* **2005**, *5* (3), 409–414. https://doi.org/10.1021/nl0486259.

(155) Xu, R.; Zhao, H.; Jin, H.; Wang, Z.; Zhang, Z.; Xu, S.; Zeng, Z.; Wang, S.; Lei, Y. Scalable Fabrication of Geometry-Tunable Self-Aligned Superlattice Photonic Crystals for Spectrum-Programmable Light Trapping. *Nano Energy* **2019**, *58*, 543–551. https://doi.org/10.1016/j.nanoen.2019.01.074.

(156) Li, W.; Guler, U.; Kinsey, N.; Naik, G. V.; Boltasseva, A.; Guan, J.; Shalaev, V. M.; Kildishev, A. V. Refractory Plasmonics with Titanium Nitride: Broadband Metamaterial Absorber. *Advanced Materials* **2014**, *26* (47), 7959–7965. https://doi.org/10.1002/adma.201401874.

(157) Li, W.; Valentine, J. Metamaterial Perfect Absorber Based Hot Electron Photodetection. *Nano Lett.* **2014**, *14* (6), 3510–3514. https://doi.org/10.1021/nl501090w.

(158) Kraemer, D.; Poudel, B.; Feng, H.-P.; Caylor, J. C.; Yu, B.; Yan, X.; Ma, Y.; Wang, X.; Wang, D.; Muto, A.; McEnaney, K.; Chiesa, M.; Ren, Z.; Chen, G. High-Performance Flat-Panel Solar Thermoelectric Generators with High Thermal Concentration. *Nature Mater* **2011**, *10* (7), 532–538. https://doi.org/10.1038/nmat3013.

(159) Nowotny, J.; Dodson, J.; Fiechter, S.; Gür, T. M.; Kennedy, B.; Macyk, W.; Bak, T.; Sigmund, W.; Yamawaki, M.; Rahman, K. A. Towards Global Sustainability: Education on Environmentally Clean Energy Technologies. *Renewable and Sustainable Energy Reviews* **2018**, *81*, 2541–2551. https://doi.org/10.1016/j.rser.2017.06.060.

(160) Zhang, Y.; Gurzadyan, G. G.; Umair, M. M.; Wang, W.; Lu, R.; Zhang, S.; Tang, B. Ultrafast and Efficient Photothermal Conversion for Sunlight-Driven Thermal-Electric System. *Chemical Engineering Journal* **2018**, *344*, 402–409. https://doi.org/10.1016/j.cej.2018.03.098.

(161) Gong, J.; Li, C.; R. Wasielewski, M. Advances in Solar Energy Conversion. *Chemical Society Reviews* **2019**, *48* (7), 1862–1864. https://doi.org/10.1039/C9CS90020A.

(162) Boudet, H. S. Public Perceptions of and Responses to New Energy Technologies. *Nat Energy* **2019**, *4* (6), 446–455. https://doi.org/10.1038/s41560-019-0399-x.

(163) Ng, C.; Yap, L. W.; Roberts, A.; Cheng, W.; Gómez, D. E. Black Gold: Broadband, High Absorption of Visible Light for Photochemical Systems. *Advanced Functional Materials* **2017**, *27* (2), 1604080. https://doi.org/10.1002/adfm.201604080.

(164) Qiu, X.; Cao, B.; Yuan, S.; Chen, X.; Qiu, Z.; Jiang, Y.; Ye, Q.; Wang, H.; Zeng, H.; Liu, J.; Kanatzidis, M. G. From Unstable CsSnI3 to Air-Stable Cs2SnI6: A Lead-Free Perovskite Solar Cell Light Absorber with Bandgap of 1.48eV and High Absorption Coefficient. *Solar Energy Materials and Solar Cells* **2017**, *159*, 227–234. https://doi.org/10.1016/j.solmat.2016.09.022.

(165) Ding, Q.; Kang, Y.; Li, W.; Sun, G.; Liu, H.; Li, M.; Ye, Z.; Zhou, M.; Zhou, J.; Yang, S. Bioinspired Brochosomes as Broadband and Omnidirectional Surface-Enhanced Raman Scattering Substrates. *J. Phys. Chem. Lett.* **2019**, *10* (21), 6484–6491. https://doi.org/10.1021/acs.jpclett.9b02380.

(166) Liu, G.; Xu, J.; Wang, K. Solar Water Evaporation by Black Photothermal Sheets. *Nano Energy* **2017**, *41*, 269–284. https://doi.org/10.1016/j.nanoen.2017.09.005.

(167) Cheng, P.; Wang, H.; Wang, H.; Aken, P. A. van; Wang, D.; Schaaf, P. High-Efficiency Photothermal Water Evaporation Using Broadband Solar Energy Harvesting by Ultrablack Silicon Structures. *Advanced Energy and Sustainability Research n/a* (n/a), 2000083. https://doi.org/10.1002/aesr.202000083.

(168) Guo, Z.; Liu, X.; Li, C.; Li, J.; Cai, H.; Fu, M.; He, D.; Wang, Y. Near-Perfect Broadband Metamaterial Absorbers of Truncated Nanocones Using Colloidal Lithography. *Optical Materials* **2021**, *119*, 111352. https://doi.org/10.1016/j.optmat.2021.111352.

(169) Zhang, Z.; Martinsen, T.; Liu, G.; Tayyib, M.; Cui, D.; Boer, M. J. de; Karlsen, F.; Jakobsen, H.; Xue, C.; Wang, K. Ultralow Broadband Reflectivity in Black Silicon via Synergy between Hierarchical Texture and Specific-Size Au Nanoparticles. *Advanced Optical Materials* **2020**, *8* (19), 2000668. https://doi.org/10.1002/adom.202000668.

(170) ElKabbash, M.; Sousa-Castillo, A.; Nguyen, Q.; Mariño-Fernández, R.; Hoffman, N.; Correa-Duarte, M. A.; Strangi, G. Tunable Black Gold: Controlling the Near-Field Coupling of Immobilized Au Nanoparticles Embedded in Mesoporous Silica Capsules. *Advanced Optical Materials* **2017**, *5* (21), 1700617. https://doi.org/10.1002/adom.201700617.

(171) Essig, S.; Allebé, C.; Remo, T.; Geisz, J. F.; Steiner, M. A.; Horowitz, K.; Barraud, L.; Ward, J. S.; Schnabel, M.; Descoeudres, A.; Young, D. L.; Woodhouse, M.; Despeisse, M.; Ballif, C.; Tamboli, A. Raising the One-Sun Conversion Efficiency of III–V/Si Solar Cells to 32.8% for Two Junctions and 35.9% for Three Junctions. *Nat Energy* **2017**, *2* (9), 1–9. https://doi.org/10.1038/nenergy.2017.144.

(172) Li, X.-B.; Xin, Z.-K.; Xia, S.-G.; Gao, X.-Y.; Tung, C.-H.; Wu, L.-Z. Semiconductor Nanocrystals for Small Molecule Activation via Artificial Photosynthesis. *Chemical Society Reviews* **2020**, *49* (24), 9028–9056. https://doi.org/10.1039/D0CS00930J.

(173) Huang, X.; El-Sayed, M. A. Plasmonic Photo-Thermal Therapy (PPTT). *Alexandria Journal of Medicine* **2011**, *47* (1), 1–9. https://doi.org/10.1016/j.ajme.2011.01.001.

(174) Lv, Z.; He, S.; Wang, Y.; Zhu, X. Noble Metal Nanomaterials for NIR-Triggered Photothermal Therapy in Cancer. *Advanced Healthcare Materials* **2021**, *10* (6), 2001806. https://doi.org/10.1002/adhm.202001806.

(175) Zhang, X.; Shiu, B.; Li, T.-T.; Liu, X.; Ren, H.-T.; Wang, Y.; Lou, C.-W.; Lin, J.-H. Synergistic Work of Photo-Thermoelectric and Hydroelectric Effects of Hierarchical Structure Photo-Thermoelectric Textile for Solar Energy Harvesting and Solar Steam Generation Simultaneously. *Chemical Engineering Journal* **2021**, *426*, 131923. https://doi.org/10.1016/j.cej.2021.131923.

(176) Wen, D.-L.; Liu, X.; Bao, J.-F.; Li, G.-K.; Feng, T.; Zhang, F.; Liu, D.; Zhang, X.-S. Flexible Hybrid Photo-Thermoelectric Generator Based on Single Thermoelectric Effect for Simultaneously Harvesting Thermal and Radiation Energies. *ACS Appl. Mater. Interfaces* **2021**, *13* (18), 21401–21410. https://doi.org/10.1021/acsami.1c03622.

(177) Liang, X.; Jiang, T.; Feng, Y.; Lu, P.; An, J.; Wang, Z. L. Triboelectric Nanogenerator Network Integrated with Charge Excitation Circuit for Effective Water Wave Energy Harvesting. *Advanced Energy Materials* **2020**, *10* (40), 2002123. https://doi.org/10.1002/aenm.202002123.

(178) Wang, Z. L.; Wu, W. Nanotechnology-Enabled Energy Harvesting for Self-Powered Micro-/Nanosystems. *Angewandte Chemie International Edition* **2012**, *51* (47), 11700–11721. https://doi.org/10.1002/anie.201201656.

(179) Komatsu, R.; Balčytis, A.; Seniutinas, G.; Yamamura, T.; Nishijima, Y.; Juodkazis, S. Plasmonic Photo-Thermoelectric Energy Converter with Black-Si Absorber. *Solar Energy Materials and Solar Cells* **2015**, *143*, 72–77. https://doi.org/10.1016/j.solmat.2015.06.035.

(180) Linic, S.; Christopher, P.; Ingram, D. B. Plasmonic-Metal Nanostructures for Efficient Conversion of Solar to Chemical Energy. *Nature Materials* **2011**, *10* (12), 911–921. https://doi.org/10.1038/nmat3151.

(181) Aslam, U.; Chavez, S.; Linic, S. Controlling Energy Flow in Multimetallic Nanostructures for Plasmonic Catalysis. *Nature Nanotechnology* **2017**, *12* (10), 1000–1005. https://doi.org/10.1038/nnano.2017.131.

(182) Li, X.-M.; Bi, M.-H.; Cui, L.; Zhou, Y.-Z.; Du, X.-W.; Qiao, S.-Z.; Yang, J. 3D Aluminum Hybrid Plasmonic Nanostructures with Large Areas of Dense Hot Spots and Long-Term Stability. *Advanced Functional Materials* **2017**, *27* (10), 1605703. https://doi.org/10.1002/adfm.201605703.

(183) Mejía-Salazar, J. R.; Oliveira, O. N. Plasmonic Biosensing. *Chem. Rev.* **2018**, *118* (20), 10617–10625. https://doi.org/10.1021/acs.chemrev.8b00359.

(184) Dai, Y.; Xu, H.; Wang, H.; Lu, Y.; Wang, P. Experimental Demonstration of High Sensitivity for Silver Rectangular Grating-Coupled Surface Plasmon Resonance (SPR) Sensing. *Optics Communications* **2018**, *416*, 66–70. https://doi.org/10.1016/j.optcom.2018.02.010.

(185) Zhou, L.; Martirez, J. M. P.; Finzel, J.; Zhang, C.; Swearer, D. F.; Tian, S.; Robatjazi, H.; Lou, M.; Dong, L.; Henderson, L.; Christopher, P.; Carter, E. A.; Nordlander, P.; Halas, N. J. Light-Driven Methane Dry Reforming with Single Atomic Site Antenna-Reactor Plasmonic Photocatalysts. *Nature Energy* **2020**, *5* (1), 61–70. https://doi.org/10.1038/s41560-019-0517-9.

(186) Yuan, L.; Lou, M.; Clark, B. D.; Lou, M.; Zhou, L.; Tian, S.; Jacobson, C. R.; Nordlander, P.; Halas, N. J. Morphology-Dependent Reactivity of a Plasmonic Photocatalyst. *ACS Nano* **2020**, *14* (9), 12054–12063. https://doi.org/10.1021/acsnano.0c05383.

(187) Zhou, L.; Swearer, D. F.; Zhang, C.; Robatjazi, H.; Zhao, H.; Henderson, L.; Dong, L.; Christopher, P.; Carter, E. A.; Nordlander, P.; Halas, N. J. Quantifying Hot Carrier and Thermal Contributions in Plasmonic Photocatalysis. *Science* **2018**, *362* (6410), 69–72. https://doi.org/10.1126/science.aat6967.

(188) Aslam, U.; Rao, V. G.; Chavez, S.; Linic, S. Catalytic Conversion of Solar to Chemical Energy on Plasmonic Metal Nanostructures. *Nature Catalysis* **2018**, *1* (9), 656–665. https://doi.org/10.1038/s41929-018-0138-x.

(189) Ng, C.; Yap, L. W.; Roberts, A.; Cheng, W.; Gómez, D. E. Black Gold: Broadband, High Absorption of Visible Light for Photochemical Systems. *Advanced Functional Materials* **2017**, *27* (2), 1604080. https://doi.org/10.1002/adfm.201604080.

(190) Linic, S.; Aslam, U.; Boerigter, C.; Morabito, M. Photochemical Transformations on Plasmonic Metal Nanoparticles. *Nature Materials* **2015**, *14* (6), 567–576. https://doi.org/10.1038/nmat4281.

(191) Christopher, P.; Xin, H.; Linic, S. Visible-Light-Enhanced Catalytic Oxidation Reactions on Plasmonic Silver Nanostructures. *Nature Chemistry* **2011**, *3* (6), 467–472. https://doi.org/10.1038/nchem.1032.

(192) Huang, X.; Tang, S.; Mu, X.; Dai, Y.; Chen, G.; Zhou, Z.; Ruan, F.; Yang, Z.; Zheng, N. Freestanding Palladium Nanosheets with Plasmonic and Catalytic Properties. *Nature*

Nanotechnology **2011**, *6* (1), 28–32. https://doi.org/10.1038/nnano.2010.235.

(193) Rycenga, M.; Cobley, C. M.; Zeng, J.; Li, W.; Moran, C. H.; Zhang, Q.; Qin, D.; Xia, Y. Controlling the Synthesis and Assembly of Silver Nanostructures for Plasmonic Applications. *Chem. Rev.* **2011**, *111* (6), 3669–3712. https://doi.org/10.1021/cr100275d.

(194) Renard, D.; Tian, S.; Lou, M.; Neumann, O.; Yang, J.; Bayles, A.; Solti, D.; Nordlander, P.; Halas, N. J. UV-Resonant Al Nanocrystals: Synthesis, Silica Coating, and Broadband Photothermal Response. *Nano Lett.* **2021**, *21* (1), 536–542. https://doi.org/10.1021/acs.nanolett.0c04020.

(195) Li, Y.; Lin, C.; Wu, Z.; Chen, Z.; Chi, C.; Cao, F.; Mei, D.; Yan, H.; Tso, C. Y.; Chao, C. Y. H.; Huang, B. Solution-Processed All-Ceramic Plasmonic Metamaterials for Efficient Solar–Thermal Conversion over 100–727 °C. *Advanced Materials* **2021**, *33* (1), 2005074. https://doi.org/10.1002/adma.202005074.

(196) Li, N.; Yang, D.-J.; Shao, Y.; Liu, Y.; Tang, J.; Yang, L.; Sun, T.; Zhou, W.; Liu, H.; Xue, G. Nanostructured Black Aluminum Prepared by Laser Direct Writing as a High-Performance Plasmonic Absorber for Photothermal/Electric Conversion. *ACS Appl. Mater. Interfaces* **2021**, *13* (3), 4305–4315. https://doi.org/10.1021/acsami.0c17584.

(197) Kim, J. U.; Kang, S. J.; Lee, S.; Ok, J.; Kim, Y.; Roh, S. H.; Hong, H.; Kim, J. K.; Chae, H.; Kwon, S. J.; Kim, T. Omnidirectional, Broadband Light Absorption in a Hierarchical Nanoturf Membrane for an Advanced Solar-Vapor Generator. *Advanced Functional Materials* **2020**, *30* (50), 2003862. https://doi.org/10.1002/adfm.202003862.

(198) Xu, R.; Zhao, H.; Jin, H.; Wang, Z.; Zhang, Z.; Xu, S.; Zeng, Z.; Wang, S.; Lei, Y. Scalable Fabrication of Geometry-Tunable Self-Aligned Superlattice Photonic Crystals for Spectrum-Programmable Light Trapping. *Nano Energy* **2019**, *58*, 543–551. https://doi.org/10.1016/j.nanoen.2019.01.074.

(199) Zhou, L.; Zhuang, S.; He, C.; Tan, Y.; Wang, Z.; Zhu, J. Self-Assembled Spectrum Selective Plasmonic Absorbers with Tunable Bandwidth for Solar Energy Conversion. *Nano Energy* **2017**, *32*, 195–200. https://doi.org/10.1016/j.nanoen.2016.12.031.

(200) Mandal, J.; Wang, D.; Overvig, A. C.; Shi, N. N.; Paley, D.; Zangiabadi, A.; Cheng, Q.; Barmak, K.; Yu, N.; Yang, Y. Scalable, "Dip-and-Dry" Fabrication of a Wide-Angle Plasmonic Selective Absorber for High-Efficiency Solar–Thermal Energy Conversion. *Advanced Materials* **2017**, *29* (41), 1702156. https://doi.org/10.1002/adma.201702156.

(201) Luo, H.; Zhu, Y.; Xu, Z.; Hong, Y.; Ghosh, P.; Kaur, S.; Wu, M.; Yang, C.; Qiu, M.; Li, Q. Outdoor Personal Thermal Management with Simultaneous Electricity Generation. *Nano Lett.* **2021**, *21* (9), 3879–3886. https://doi.org/10.1021/acs.nanolett.1c00400.

(202) Luo, H.; Li, Q.; Du, K.; Xu, Z.; Zhu, H.; Liu, D.; Cai, L.; Ghosh, P.; Qiu, M. An Ultra-Thin Colored Textile with Simultaneous Solar and Passive Heating Abilities. *Nano Energy* **2019**, *65*, 103998. https://doi.org/10.1016/j.nanoen.2019.103998.

(203) Chatterjee, H.; Rahman, D. S.; Sengupta, M.; Ghosh, S. K. Gold Nanostars in Plasmonic Photothermal Therapy: The Role of Tip Heads in the Thermoplasmonic Landscape. *J. Phys. Chem. C* **2018**, *122* (24), 13082–13094. https://doi.org/10.1021/acs.jpcc.8b00388.

(204) Reineck, P.; Lee, G. P.; Brick, D.; Karg, M.; Mulvaney, P.; Bach, U. A Solid-State Plasmonic Solar Cell via Metal Nanoparticle Self-Assembly. *Advanced Materials* **2012**, *24* (35), 4750–4755. https://doi.org/10.1002/adma.201200994.

(205) Wang, L.; Kafshgari, M. H.; Meunier, M. Optical Properties and Applications of Plasmonic-

Metal Nanoparticles. *Advanced Functional Materials* **2020**, *30* (51), 2005400. https://doi.org/10.1002/adfm.202005400.

(206) Hou, G.; Wang, Z.; Lu, Z.; Song, H.; Xu, J.; Chen, K. Enhanced Broadband Plasmonic Absorbers with Tunable Light Management on Flexible Tapered Metasurface. *ACS Appl. Mater. Interfaces* **2020**, *12* (50), 56178–56185. https://doi.org/10.1021/acsami.0c16189.

(207) Maniyara, R. A.; Rodrigo, D.; Yu, R.; Canet-Ferrer, J.; Ghosh, D. S.; Yongsunthon, R.; Baker, D. E.; Rezikyan, A.; García de Abajo, F. J.; Pruneri, V. Tunable Plasmons in Ultrathin Metal Films. *Nature Photonics* **2019**, *13* (5), 328–333. https://doi.org/10.1038/s41566-019-0366-x.

(208) Kats, M. A.; Blanchard, R.; Genevet, P.; Capasso, F. Nanometre Optical Coatings Based on Strong Interference Effects in Highly Absorbing Media. *Nature Materials* **2013**, *12* (1), 20–24. https://doi.org/10.1038/nmat3443.

(209) Zhan, C.; Liu, B.-W.; Huang, Y.-F.; Hu, S.; Ren, B.; Moskovits, M.; Tian, Z.-Q. Disentangling Charge Carrier from Photothermal Effects in Plasmonic Metal Nanostructures. *Nature Communications* **2019**, *10* (1), 2671. https://doi.org/10.1038/s41467-019-10771-3.

(210) Langhammer, C.; Yuan, Z.; Zorić, I.; Kasemo, B. Plasmonic Properties of Supported Pt and Pd Nanostructures. *Nano Lett.* **2006**, *6* (4), 833–838. https://doi.org/10.1021/nl060219x.

(211) Gao, L.; Zhang, Y.; Zhang, H.; Doshay, S.; Xie, X.; Luo, H.; Shah, D.; Shi, Y.; Xu, S.; Fang, H.; Fan, J. A.; Nordlander, P.; Huang, Y.; Rogers, J. A. Optics and Nonlinear Buckling Mechanics in Large-Area, Highly Stretchable Arrays of Plasmonic Nanostructures. *ACS Nano* **2015**, *9* (6), 5968–5975. https://doi.org/10.1021/acsnano.5b00716.

(212) Zhao, J.; Zhang, C.; Braun, P. V.; Giessen, H. Large-Area Low-Cost Plasmonic Nanostructures in the NIR for Fano Resonant Sensing. *Advanced Materials* **2012**, *24* (35), OP247–OP252. https://doi.org/10.1002/adma.201202109.

(213) Ziegler, M.; Thamm, S.; Stolle, H. L. K. S.; Dellith, J.; Hübner, U.; Wang, D.; Schaaf, P. 3D Structure Evolution Using Metastable Atomic Layer Deposition Based on Planar Silver Templates. *Applied Surface Science* **2020**, *514*, 145770. https://doi.org/10.1016/j.apsusc.2020.145770.

(214) Fei Guo, C.; Sun, T.; Cao, F.; Liu, Q.; Ren, Z. Metallic Nanostructures for Light Trapping in Energy-Harvesting Devices. *Light: Science & Applications* **2014**, *3* (4), e161–e161. https://doi.org/10.1038/lsa.2014.42.

(215) Zhou, L.; Zhuang, S.; He, C.; Tan, Y.; Wang, Z.; Zhu, J. Self-Assembled Spectrum Selective Plasmonic Absorbers with Tunable Bandwidth for Solar Energy Conversion. *Nano Energy* **2017**, *32*, 195–200. https://doi.org/10.1016/j.nanoen.2016.12.031.

(216) Sahm, H.; Charton, C.; Thielsch, R. Oxidation Behaviour of Thin Silver Films Deposited on Plastic Web Characterized by Spectroscopic Ellipsometry (SE). *Thin Solid Films* **2004**, *455–456*, 819–823. https://doi.org/10.1016/j.tsf.2003.11.266.

(217) Dudem, B.; Bharat, L. K.; Leem, J. W.; Kim, D. H.; Yu, J. S. Hierarchical Ag/TiO2/Si Forest-Like Nano/Micro-Architectures as Antireflective, Plasmonic Photocatalytic, and Self-Cleaning Coatings. *ACS Sustainable Chem. Eng.* **2018**, *6* (2), 1580–1591. https://doi.org/10.1021/acssuschemeng.7b02220.

(218) Shi, G.; Zhang, X.; Li, J.; Zhu, H.; Li, Y.; Zhang, L.; Ni, C.; Chi, L. Fabrication of 3D Biomimetic Composite Coating with Broadband Antireflection, Superhydrophilicity, and Double p-n Heterojunctions. *Nano Res.* **2017**, *10* (7), 2377–2385.

https://doi.org/10.1007/s12274-017-1434-5.

(219) Yang, J.; Luo, F.; Kao, T. S.; Li, X.; Ho, G. W.; Teng, J.; Luo, X.; Hong, M. Design and Fabrication of Broadband Ultralow Reflectivity Black Si Surfaces by Laser Micro/Nanoprocessing. *Light: Science & Applications* **2014**, *3* (7), e185–e185. https://doi.org/10.1038/lsa.2014.66.

(220) Yang, S.; Sun, N.; Stogin, B. B.; Wang, J.; Huang, Y.; Wong, T.-S. Ultra-Antireflective Synthetic Brochosomes. *Nature Communications* **2017**, *8* (1), 1285. https://doi.org/10.1038/s41467-017-01404-8.

(221) Zhao, W.; Shen, D.; Zou, G.; Zhao, G.; Bai, H.; Liu, L.; Zhou, Y. Super Black Iron Nanostructures with Broadband Ultralow Reflectance for Efficient Photothermal Conversion. *Applied Surface Science* **2020**, *521*, 146388. https://doi.org/10.1016/j.apsusc.2020.146388.

(222) Naldoni, A.; Kudyshev, Z. A.; Mascaretti, L.; Sarmah, S. P.; Rej, S.; Froning, J. P.; Tomanec, O.; Yoo, J. E.; Wang, D.; Kment, Š.; Montini, T.; Fornasiero, P.; Shalaev, V. M.; Schmuki, P.; Boltasseva, A.; Zbořil, R. Solar Thermoplasmonic Nanofurnace for High-Temperature Heterogeneous Catalysis. *Nano Lett.* **2020**, *20* (5), 3663–3672. https://doi.org/10.1021/acs.nanolett.0c00594.

(223) Lei, L.; Li, S.; Huang, H.; Tao, K.; Xu, P. Ultra-Broadband Absorber from Visible to near-Infrared Using Plasmonic Metamaterial. *Opt. Express, OE* **2018**, *26* (5), 5686–5693. https://doi.org/10.1364/OE.26.005686.

(224) Ren, J.; Yu, A.; Peng, P.; Lefler, M.; Li, F.-F.; Licht, S. Recent Advances in Solar Thermal Electrochemical Process (STEP) for Carbon Neutral Products and High Value Nanocarbons. *Acc. Chem. Res.* **2019**, *52* (11), 3177–3187. https://doi.org/10.1021/acs.accounts.9b00405.

(225) Kar, S.; Sen, R.; Goeppert, A.; Prakash, G. K. S. Integrative CO2 Capture and Hydrogenation to Methanol with Reusable Catalyst and Amine: Toward a Carbon Neutral Methanol Economy. *J. Am. Chem. Soc.* **2018**, *140* (5), 1580–1583. https://doi.org/10.1021/jacs.7b12183.

(226) Carlino, A.; Vita, A. D.; Giuliani, M.; Zamberletti, P.; Capros, P.; Recanati, F.; Kannavou, M.; Castelletti, A. Hydroclimatic Change Challenges the EU Planned Transition to a Carbon Neutral Electricity System. *Environ. Res. Lett.* **2021**, *16* (10), 104011. https://doi.org/10.1088/1748-9326/ac243f.

(227) Zhao, N.; You, F. Can Renewable Generation, Energy Storage and Energy Efficient Technologies Enable Carbon Neutral Energy Transition? *Applied Energy* **2020**, *279*, 115889. https://doi.org/10.1016/j.apenergy.2020.115889.

(228) Men, Y.; Li, P.; Zhou, J.; Cheng, G.; Chen, S.; Luo, W. Tailoring the Electronic Structure of Co2P by N Doping for Boosting Hydrogen Evolution Reaction at All PH Values. *ACS Catal.* **2019**, *9* (4), 3744–3752. https://doi.org/10.1021/acscatal.9b00407.

(229) Zhu, J.; Hu, L.; Zhao, P.; Lee, L. Y. S.; Wong, K.-Y. Recent Advances in Electrocatalytic Hydrogen Evolution Using Nanoparticles. *Chem. Rev.* **2020**, *120* (2), 851–918. https://doi.org/10.1021/acs.chemrev.9b00248.

(230) Dawood, F.; Anda, M.; Shafiullah, G. M. Hydrogen Production for Energy: An Overview. *International Journal of Hydrogen Energy* **2020**, *45* (7), 3847–3869. https://doi.org/10.1016/j.ijhydene.2019.12.059.

(231) Yu, J.; Li, G.; Liu, H.; Zeng, L.; Zhao, L.; Jia, J.; Zhang, M.; Zhou, W.; Liu, H.; Hu, Y.

Electrochemical Flocculation Integrated Hydrogen Evolution Reaction of Fe@N-Doped Carbon Nanotubes on Iron Foam for Ultralow Voltage Electrolysis in Neutral Media. *Advanced Science* **2019**, *6* (18), 1901458. https://doi.org/10.1002/advs.201901458.

(232) Huang, H.; Yan, M.; Yang, C.; He, H.; Jiang, Q.; Yang, L.; Lu, Z.; Sun, Z.; Xu, X.; Bando, Y.; Yamauchi, Y. Graphene Nanoarchitectonics: Recent Advances in Graphene-Based Electrocatalysts for Hydrogen Evolution Reaction. *Advanced Materials* **2019**, *31* (48), 1903415. https://doi.org/10.1002/adma.201903415.

(233) Bae, S.-Y.; Mahmood, J.; Jeon, I.-Y.; Baek, J.-B. Recent Advances in Ruthenium-Based Electrocatalysts for the Hydrogen Evolution Reaction. *Nanoscale Horizons* **2020**, *5* (1), 43–56. https://doi.org/10.1039/C9NH00485H.

(234) Yang, W.; Ramanujam Prabhakar, R.; Tan, J.; David Tilley, S.; Moon, J. Strategies for Enhancing the Photocurrent, Photovoltage, and Stability of Photoelectrodes for Photoelectrochemical Water Splitting. *Chemical Society Reviews* **2019**, *48* (19), 4979–5015. https://doi.org/10.1039/C8CS00997J.

(235) Li, Y.; Sun, Y.; Qin, Y.; Zhang, W.; Wang, L.; Luo, M.; Yang, H.; Guo, S. Recent Advances on Water-Splitting Electrocatalysis Mediated by Noble-Metal-Based Nanostructured Materials. *Advanced Energy Materials* **2020**, *10* (11), 1903120. https://doi.org/10.1002/aenm.201903120.

(236) Wang, Q.; Domen, K. Particulate Photocatalysts for Light-Driven Water Splitting: Mechanisms, Challenges, and Design Strategies. *Chem. Rev.* **2020**, *120* (2), 919–985. https://doi.org/10.1021/acs.chemrev.9b00201.

(237) Takata, T.; Jiang, J.; Sakata, Y.; Nakabayashi, M.; Shibata, N.; Nandal, V.; Seki, K.; Hisatomi, T.; Domen, K. Photocatalytic Water Splitting with a Quantum Efficiency of Almost Unity. *Nature* **2020**, *581* (7809), 411–414. https://doi.org/10.1038/s41586-020-2278-9.

(238) Mei, Z.; Chen, Y.; Tong, S.; Li, Y.; Liu, J.; Sun, L.; Zhong, W.; Dong, X.; Ji, Y.; Lin, Y.; Chen, H.; Pan, F. High-Performance Si Photocathode Enabled by Spatial Decoupling Multifunctional Layers for Water Splitting. *Advanced Functional Materials n/a* (n/a), 2107164. https://doi.org/10.1002/adfm.202107164.

(239) Vanka, S.; Zhou, B.; Awni, R. A.; Song, Z.; Chowdhury, F. A.; Liu, X.; Hajibabaei, H.; Shi, W.; Xiao, Y.; Navid, I. A.; Pandey, A.; Chen, R.; Botton, G. A.; Hamann, T. W.; Wang, D.; Yan, Y.; Mi, Z. InGaN/Si Double-Junction Photocathode for Unassisted Solar Water Splitting. *ACS Energy Lett.* **2020**, *5* (12), 3741–3751. https://doi.org/10.1021/acsenergylett.0c01583.

(240) Choi, S.; Hwang, J.; Lee, T. H.; Kim, H.-H.; Hong, S.-P.; Kim, C.; Choi, M.-J.; Park, H. K.; Bhat, S. S. M.; Suh, J. M.; Lee, J.; Choi, K. S.; Hong, S.-H.; Shin, J. C.; Jang, H. W. Photoelectrochemical Hydrogen Production at Neutral PH Phosphate Buffer Solution Using TiO2 Passivated InAs Nanowire/p-Si Heterostructure Photocathode. *Chemical Engineering Journal* **2020**, *392*, 123688. https://doi.org/10.1016/j.cej.2019.123688.

(241) Oh, J.; G. Deutsch, T.; Yuan, H.-C.; M. Branz, H. Nanoporous Black Silicon Photocathode for H 2 Production by Photoelectrochemical Water Splitting. *Energy & Environmental Science* **2011**, *4* (5), 1690–1694. https://doi.org/10.1039/C1EE01124C.

(242) Huang, G.; Fan, R.; Zhou, X.; Xu, Z.; Zhou, W.; Dong, W.; Shen, M. A Porous Ni-O/Ni/Si Photoanode for Stable and Efficient Photoelectrochemical Water Splitting. *Chemical Communications* **2019**, *55* (3), 377–380. https://doi.org/10.1039/C8CC08146H.

(243) Choi, S.; Hwang, J.; Lee, T. H.; Kim, H.-H.; Hong, S.-P.; Kim, C.; Choi, M.-J.; Park, H. K.; Bhat, S. S. M.; Suh, J. M.; Lee, J.; Choi, K. S.; Hong, S.-H.; Shin, J. C.; Jang, H. W. Photoelectrochemical Hydrogen Production at Neutral PH Phosphate Buffer Solution Using TiO2 Passivated InAs Nanowire/p-Si Heterostructure Photocathode. *Chemical Engineering Journal* **2020**, *392*, 123688. https://doi.org/10.1016/j.cej.2019.123688.

(244) Branz, H. M.; Yost, V. E.; Ward, S.; Jones, K. M.; To, B.; Stradins, P. Nanostructured Black Silicon and the Optical Reflectance of Graded-Density Surfaces. *Appl. Phys. Lett.* **2009**, *94* (23), 231121. https://doi.org/10.1063/1.3152244.

(245) Thalluri, S. M.; Wei, B.; Welter, K.; Thomas, R.; Smirnov, V.; Qiao, L.; Wang, Z.; Finger, F.; Liu, L. Inverted Pyramid Textured P-Silicon Covered with Co2P as an Efficient and Stable Solar Hydrogen Evolution Photocathode. *ACS Energy Lett.* **2019**, *4* (7), 1755–1762. https://doi.org/10.1021/acsenergylett.9b00964.

(246) Ros, C.; Andreu, T.; Hernández-Alonso, M. D.; Penelas-Pérez, G.; Arbiol, J.; Morante, J. R. Charge Transfer Characterization of ALD-Grown TiO2 Protective Layers in Silicon Photocathodes. *ACS Appl. Mater. Interfaces* **2017**, *9* (21), 17932–17941. https://doi.org/10.1021/acsami.7b02996.

(247) Morozov, I.; Gudovskikh, A.; Uvarov, A.; Baranov, A.; Sivakov, V.; Kudryashov, D. The Study of Latex Sphere Lithography for High Aspect Ratio Dry Silicon Etching. *physica status solidi (a)* **2020**, *217* (4), 1900535. https://doi.org/10.1002/pssa.201900535.

(248) Gao, J.; Li, L.; Tan, J.; Sun, H.; Li, B.; Idrobo, J. C.; Singh, C. V.; Lu, T.-M.; Koratkar, N. Vertically Oriented Arrays of ReS2 Nanosheets for Electrochemical Energy Storage and Electrocatalysis. *Nano Lett.* **2016**, *16* (6), 3780–3787. https://doi.org/10.1021/acs.nanolett.6b01180.

(249) Chenet, D. A.; Aslan, O. B.; Huang, P. Y.; Fan, C.; van der Zande, A. M.; Heinz, T. F.; Hone, J. C. In-Plane Anisotropy in Mono- and Few-Layer ReS2 Probed by Raman Spectroscopy and Scanning Transmission Electron Microscopy. *Nano Lett.* **2015**, *15* (9), 5667–5672. https://doi.org/10.1021/acs.nanolett.5b00910.

(250) He, X.; Liu, F.; Hu, P.; Fu, W.; Wang, X.; Zeng, Q.; Zhao, W.; Liu, Z. Chemical Vapor Deposition of High-Quality and Atomically Layered ReS2. *Small* **2015**, *11* (40), 5423–5429. https://doi.org/10.1002/smll.201501488.

(251) Pang, Q.-Q.; Niu, Z.-L.; Yi, S.-S.; Zhang, S.; Liu, Z.-Y.; Yue, X.-Z. Hydrogen-Etched Bifunctional Sulfur-Defect-Rich ReS2/CC Electrocatalyst for Highly Efficient HER and OER. *Small* **2020**, *16* (34), 2003007. https://doi.org/10.1002/smll.202003007.

(252) Rahman, M.; Davey, K.; Qiao, S.-Z. Advent of 2D Rhenium Disulfide (ReS2): Fundamentals to Applications. *Advanced Functional Materials* **2017**, *27* (10), 1606129. https://doi.org/10.1002/adfm.201606129.

(253) Zhao, H.; Dai, Z.; Xu, X.; Pan, J.; Hu, J. Integrating Semiconducting Catalyst of ReS2 Nanosheets into P-Silicon Photocathode for Enhanced Solar Water Reduction. *ACS Appl. Mater. Interfaces* **2018**, *10* (27), 23074–23080. https://doi.org/10.1021/acsami.8b04740.

(254) Hafeez, M.; Gan, L.; Li, H.; Ma, Y.; Zhai, T. Large-Area Bilayer ReS2 Film/Multilayer ReS2 Flakes Synthesized by Chemical Vapor Deposition for High Performance Photodetectors. *Advanced Functional Materials* **2016**, *26* (25), 4551–4560. https://doi.org/10.1002/adfm.201601019.

(255) Zhang, Y.; Liu, Y.; Cheng, P.; Song, W.; Zhang, X.; Rong, S.; Gao, X.; Zhou, G.; Zhang, Z.;

Liu, J. Universal Substrate Growth of Ag-Modified ReS2 as Visible-Light-Driven Photocatalyst for Highly Efficient Water Disinfection. *Chemical Engineering Journal* **2022**, *430*, 132918. https://doi.org/10.1016/j.cej.2021.132918.

(256) Mathpal, M. C.; Tripathi, A. K.; Singh, M. K.; Gairola, S. P.; Pandey, S. N.; Agarwal, A. Effect of Annealing Temperature on Raman Spectra of TiO2 Nanoparticles. *Chemical Physics Letters* **2013**, *555*, 182–186. https://doi.org/10.1016/j.cplett.2012.10.082.

(257) Wang, H.; Xiong, J.; Cheng, X.; Chen, G.; Kups, T.; Wang, D.; Schaaf, P. Hydrogen–Nitrogen Plasma Assisted Synthesis of Titanium Dioxide with Enhanced Performance as Anode for Sodium Ion Batteries. *Sci Rep* **2020**, *10* (1), 11817. https://doi.org/10.1038/s41598-020-68838-x.

(258) Li, J.; Zhou, Q.; Yuan, C.; Cheng, P.; Hu, X.; Huang, W.; Gao, X.; Wang, X.; Jin, M.; Nötzel, R.; Zhou, G.; Zhang, Z.; Liu, J. Direct Growth of Vertically Aligned ReSe2 Nanosheets on Conductive Electrode for Electro-Catalytic Hydrogen Production. *Journal of Colloid and Interface Science* **2019**, *553*, 699–704. https://doi.org/10.1016/j.jcis.2019.06.073.

(259) Huang, Z.; Zhong, P.; Wang, C.; Zhang, X.; Zhang, C. Silicon Nanowires/Reduced Graphene Oxide Composites for Enhanced Photoelectrochemical Properties. *ACS Appl. Mater. Interfaces* **2013**, *5* (6), 1961–1966. https://doi.org/10.1021/am3027458.

(260) Lv, C.; Chen, Z.; Chen, Z.; Zhang, B.; Qin, Y.; Huang, Z.; Zhang, C. Silicon Nanowires Loaded with Iron Phosphide for Effective Solar-Driven Hydrogen Production. *Journal of Materials Chemistry A* **2015**, *3* (34), 17669–17675. https://doi.org/10.1039/C5TA03438H.

(261) Jun, S. E.; Hong, S.-P.; Choi, S.; Kim, C.; Ji, S. G.; Park, I. J.; Lee, S. A.; Yang, J. W.; Lee, T. H.; Sohn, W.; Kim, J. Y.; Jang, H. W. Boosting Unassisted Alkaline Solar Water Splitting Using Silicon Photocathode with TiO2 Nanorods Decorated by Edge-Rich MoS2 Nanoplates. *Small* **2021**, *17* (39), 2103457. https://doi.org/10.1002/smll.202103457.

(262) Park, J. Y.; Joe, H.-E.; Yoon, H. S.; Yoo, S.; Kim, T.; Kang, K.; Min, B.-K.; Jun, S. C. Contact Effect of ReS2/Metal Interface. *ACS Appl. Mater. Interfaces* **2017**, *9* (31), 26325–26332. https://doi.org/10.1021/acsami.7b06432.

Scientific Publications of Pengfei Cheng

(1) Pengfei Cheng, Honglei Wang, Björn Müller, Jens Müller, Dong Wang, Peter Schaaf. Photo-Thermoelectric Conversion Using Black Silicon with Enhanced Light Trapping Performance far beyond the Band Edge Absorption. ACS Appl. Mater. Interfaces **2021**, 13, 1, 1818–1826.

(2) Pengfei Cheng, Honglei Wang, Hongguang Wang, Peter A. van Aken, Dong Wang, Peter Schaaf. High-Efficiency Photothermal Water Evaporation using Broadband Solar Energy Harvesting by Ultrablack Silicon Stucture. Adv. Energy Sustainability Res. **2021**, 2, 2000083.

(3) Pengfei Cheng, Mario Ziegler, Valentin Ripka, Dong Wang, Hongguang Wang, Peter Schaaf. Bio-inspired self-assembly of large-scale 3D Ag@SiO2 plasmonic nanostructures with tunable broadband light harvesting. Applied Materials Today. **2021**, 25 101238

(4) Pengfei Cheng, Ronald Kampmann, Dong Wang, Stefan Sinzinger, Peter Schaaf. Tailoring patterned visible-light scattering by silicon photonic crystals. ACS Appl. Mater. Interfaces **2021**, 13, 60319−60326.

(5) Pengfei Cheng, Mario Ziegler, Valentin Ripka, Honglei Wang, Kilian Pollok, Falko Langenhorst, Dong Wang, Peter Schaaf. Black silver: 3D Ag hybrid plasmonic nanostructures with strongly photon coupling for scalable photo-thermoelectric power generation. ACS Appl. Mater. Interfaces **2022**, 14, 14, 16894-16900.

(6) Pengfei Cheng, Yuanwu Liu, Mario Ziegler, Malte Klingenhof, Dong Wang, Zhang Zhang, Peter Strasser, Peter Schaaf. Improving Silicon Photocathode Performance for Water Reduction through Dual Interface Engineering and Integrating ReS_2 Photocatalyst. ACS Appl. Energy Mater **2022**, 5, 7, 8222–8231.

(7) Pengfei Cheng, Dong Wang, Peter Schaaf. A Review on Photothermal Conversion of Solar Energy with Nanomaterials and Nanostructures: From fundamentals to applications. Advanced Sustainable Systems **2022**, Adv. Sustainable Syst. 2022, 2200115**. (Invited)**

(8) Xuyan Zhang, **Pengfei Cheng**, Weiming Song, Shiya Rong, Jieming Huang, Dong Wang, Peter Schaaf, Guofu Zhou, Zhang Zhang, Junming Liu. Photo-Thermoelectric Conversion and Photothermal Imaging using 2D/3D ReS_2@Carbon Framework with Enhanced Photon Harvesting. Chemical Engineering Journal **2022**, 430, 132918. (**Co-first author**)

(9) Honglei Wang, **Pengfei Cheng**, Jun Shi,b Dong Wang, Hongguang Wang, Jörg Pezoldt, Michael Stich, Runfeng Chen, Peter A. van Aken, Wei Huang, and Peter Schaaf. Efficient Fabrication of MoS2 Nanocomposites by Water-assisted Exfoliation for Nonvolatile Memories. *Green Chemistry* **2021**, 23, 3642-3648.

Manuscripts in submission.

(10) Pengfei Cheng, Joachim Döll, et al, Reactive Magnetron Sputtering of Large-scale 3D Aluminum-based Plasmonic Nanostructure for both Light-induced Thermal Imaging and Photo-thermoelectric Conversion. In submission.

(11) Shiya Rong**, Pengfei Cheng, et al.** Multicore-shell Au@ZnO Nanostructures for Plasmonic Photocatalysis. In submission. (**Co-first author**)

(12) **Pengfei Cheng**, Dong Wang. Repairable Carbon Absorber for Simultaneous Photo-thermoelectric Conversion and Photothermal Water Evaporation. Solar RRL. In submission.

Conferences:

6th Bioinspired Materials 2022, Bavaria, Germany (Online talk)

Supervision of project works:

a) 2021 Project work, Jipanyu Lu

Topic: Fabricating high performance half-transparent Fe_2O_3 photoanode for tandem photoelectrochemical water splitting

b) 2021 Project work, Tzu-Chin Huang

Topic: Oxygen vacancies inhibiting the activation of Au/TiO_2 photocatalyst

Declaration

I hereby declare that this Ph.D. dissertation entitled "Broadband solar energy harvesting enabled by micro-nanostructured materials" was carried out by me for the degree of Doctor under the supervision of Univ. Dr. rer. nat. habil. Dr. hc Peter Schaaf. All data or information in this dissertation that have been directly or indirectly consulted or used from other sources are clearly stated. This dissertation has not been submitted, in part or in whole, for any other degree or examination in any other University. I have acknowledged all main sources of help, and I have made clear exactly what was done by others and what I have contributed when the work was done jointly with others. Some of the results may have been published in scientific journals or elsewhere. I am aware that the falsity of this declaration will be regarded as an attempt of deception and will cause the derogation of the doctoral procedure.

Ilmenau, 20 Sept, 2022

(*Place, date*)

Pengfei Cheng

(*Signature*)